Light-Matter Interaction with Focused Optical Fields: Directional Scattering and Dynamics of Active Colloids

A thesis

submitted in partial fulfilment of the requirements
for the degree of Doctor of Philosophy

by

Diptabrata Paul

(Reg ID: 20162035)

IISER PUNE

INDIAN INSTITUTE OF SCIENCE EDUCATION AND RESEARCH, PUNE

Certificate

Certified that the work incorporated in the thesis entitled "Light-Matter Interaction with Focused Optical Fields: Directional Scattering and Dynamics of Active Colloids" submitted by **Diptabrata Paul** was carried out by the candidate, under my supervision. The work presented here or any part of it has not been included in any other thesis submitted previously for the award of any degree or diploma from any other university or institution.

Date: January 18, 2023

(Dr. G V Pavan Kumar)

Supervisor

<u>Declaration</u>

I declare that this written submission represents my research work in my own words and where others' ideas or works have been included, I have adequately cited and referenced the original sources. I also declare that I have adhered to all principles of academic honesty and integrity and have not misrepresented or fabricated or falsified any idea/data/fact/source in my submission. I understand that the violation of the above will be a cause for disciplinary action by the Institute and can also evoke penal action from the sources which have thus not been properly cited or from whom proper permission has not been taken when needed.

Date: January 18, 2023

(Diptabrata Paul)

Reg. No: 20162035

Abstract

Along with energy and linear momentum, angular momentum represents the most fundamental properties of light. These effect of these properties in various light-matter interactions become much more prominent upon focusing of the optical field to a small region. As a result, at the microscopic scale, the interaction of focused optical fields and the corresponding angular momentum of light with matter, broadly known as spin-orbit interactions (SOIs), can lead to various effects such as directional scattering, inter conversion of angular momentum as well as micro manipulation. On the other hand, illuminated optical fields intensity lead to optothermal heating of metallic objects, which can be utilized to trap as well as manipulate colloidal particles through thermophoresis, thermos-osmosis effects.

In this thesis, broadly divided into two parts, we will discuss how these interactions can be modulated by the characteristics of the focal optical field properties. The first part discusses the numerical and experimental results on how angular momentum characteristics of the focal optical fields can be investigated by studying the forward scattering of a strongly focused optical field and the resultant SOIs. The second part involves discussion on the optical trapping and optothermal heating due to these optical fields, which leads to unconventional dynamics of thermally active colloids.

Firstly, we address the question on how the polarization dependence of the Fourier plane scattering pattern can be utilized for simultaneous detection of spin and orbital angular momentum of light. In addition, we will discuss how the Fourier plane intensity distribution of the scattering of strongly focused linearly polarized light from a quasi-one-dimensional monocrystalline silver nanowire can be utilized to study the focal optical field characteristics. Through both numerical and experimental studies, we show detection of longitudinal spin density as well as the consequent optical spin-Hall effect.

The following part discusses the optothermal heating due to focused and defocused optical field and its effect on the interaction with thermally active colloidal particles. We show that the thermophoretic behavior of the thermally active colloids can be exploited to form

self-evolving dynamic assembly of the colloids for defocused laser beam illumination. Furthermore, it has been shown that polarization plays a key role in structural orientation of these assemblies. Driving these active colloids using optical orbital angular momentum also leads to collective dynamics, which unlike passive colloids, slows down and forms a colloidal matter while undergoing rotational motion.

The thesis concludes by summarizing the key experimental results and outlines some possibilities for extrapolation of the results for future studies.

List of Publications

Included in the thesis:

- **Diptabrata Paul**, Deepak K. Sharma, and G. V. Pavan Kumar, *Focused linearly-polarized-light scattering from a silver nanowire: experimental characterization of the optical spin-Hall effect*, **Physical Review A, 103, 013520 (2021) (arXiv:2008.12245)**

- **Diptabrata Paul**, Deepak K. Sharma, and G. V. Pavan Kumar, *Simultaneous detection of spin and orbital angular momentum of light through scattering from a single silver nanowire*, **Laser & Photonics Reviews, 16, 2200049 (2022) (arXiv:2111.14919)**

- **Diptabrata Paul***, Rahul Chand*, and G. V. Pavan Kumar, *Opto-thermal evolution of active colloidal matter in defocused laser trap*, **ACS Photonics, 9, 3440-3449 (2022) (arXiv:2203.08904) (*Equal contribution**)

- **Diptabrata Paul**, Rahul Chand, and G. V. Pavan Kumar, *Orbital angular momentum driven collective motion of active colloids*, **under preparation** (2022).

Not included in the thesis:

- Chetna Taneja*, **Diptabrata Paul***, and G. V. Pavan Kumar, *Experimental observation of transverse spin of plasmon polaritons in a single-crystalline silver nanowire*, **Applied Physics Letters, 119, 161108 (2021) (*Equal contribution**)

- Tamaghna Chowdhury*, **Diptabrata Paul***, Divya Nechiyil, Gokul M.A, Kenji Watanabe, Takashi Taniguchi, G. V. Pavan Kumar, and Atikur Rahman, *Modulation of trion and exciton formation in monolayer WS2 by dielectric and substrate engineering*, **2D Materials, 8, 045032 (2021) (*Equal contribution**)

- Vandana Sharma, **Diptabrata Paul**, Shailendra K Chaubey, Sunny Tiwari, and G. V. Pavan Kumar, *Large-scale optothermal assembly of colloids mediated by a gold microplate*, **Journal of Physics: Condensed Matter, 32, 324002 (2020)**

- Deepak K. Sharma, Vijay Kumar, Adarsh B. Vasista, **Diptabrata Paul**, Shailendra K. Chaubey and G. V. Pavan Kumar, *Optical Orbital Angular Momentum Read-Out Using a Self-Assembled Plasmonic Nanowire*, **ACS Photonics, 6(1), 148-153(2019)**

- Vandana Sharma, Sunny Tiwari, **Diptabrata Paul**, Ratimanasee Sahu, Vijayakumar Chikkadi, and G V Pavan Kumar, *Optothermal pulling, trapping, and assembly of colloids using nanowire plasmons*, **Soft Matter, 17, 10903-10909, (2021)**

- Sunny Tiwari, Adarsh B. Vasista, **Diptabrata Paul**, Shailendra K. Chaubey, and G. V. Pavan Kumar, *Beaming Elastic and SERS Emission from Bent-Plasmonic Nanowire on a Mirror Cavity*, **The Journal of Physical Chemistry Letters, 12, 6589-6595 (2021)**

- Sunny Tiwari, Adarsh Vasista, **Diptabrata Paul**, and G. V. Pavan Kumar, *Mirror enhanced directional out-coupling of SERS by remote excitation of a nanowire- nanoparticle cavity*, **Journal of Optics, 23, 124001 (2021)**

- Sunny Tiwari, Chetna Taneja, Vandana Sharma, Adarsh B. Vasista, **Diptabrata Paul**, and G. V. Pavan Kumar, *Dielectric microsphere coupled to a plasmonic nanowire: A self-assembled hybrid optical antenna*, **Advanced Optical Materials, 1901672 (2020)**

- Shailendra K. Chaubey, Gokul M. A., **Diptabrata Paul**, Sunny Tiwari, Atikur Rahman, and G. V. Pavan Kumar, *Directional emission from WS2 monolayer coupled to plasmonic Nanowire-on-Mirror Cavity*, **Advanced Photonics Research, 2100002 (2021)**

- Shailendra K. Chaubey, Sunny Tiwari, Gokul M. A., **Diptabrata Paul**, Atikur Rahman, and G. V. Pavan Kumar, *Beaming of WS2 Photoluminescence from a Film coupled Microsphere Antenna*, **Applied Physics Letters, 120, 261109, (2022)**

Acknowledgments

and many wonderful memories. In addition, I will forever cherish memories of the post-midnight mischievous adventures with Aditya and Akash. The life in Hostel 2 as well as outside the lab has been more memorable because of Tamaghna, Arnab and Ratheejit. The occasional cooking sessions brought flavors to the monotonous routine at times, and the monsoon weekend road trips have taught me to tackle rough terrains and muddy potholes in rainy roads as well as live through the tough times. I will also always fondly remember all the nice times I spent with Sagnik, Sudipta, Sayan and Anupam da.

Words cannot express how much I have been supported by the love and support from friends and family outside of IISER Pune. My parents have made tremendous sacrifices throughout my life, just to help me be the best and happiest I could be, and I strive to do the same for them in the coming years. I would like to express my heartfelt gratitude to Sruti for always being the never ending source of optimism as well as always supporting me by proof reading every document I requested, even till late night. I am very thankful to Dr. Saugata Bhattacharyya for his guidance and being an inspiration for pursuing an academic career. Finally, I am also thankful to my elder brother Soumyabrata, who has always inspired me and motivated me to pursue research in Physics.

Dedicated to Maa and Baba...

Contents

Chapter 1

Introduction

It is well known that a light beam carries energy and momentum, quantified by its Poynting vector [1]. Additionally engineering the phase and polarization of the beam can give rise to angular momentum which can be further subdivided into spin angular momentum (SAM) and orbital angular momentum (OAM) [2, 3]. These parameters play a crucial role in all light matter interaction [4]. For example, strong optical field at the focus of an objective lens and the resultant light-matter interaction at the interface of a colloidal particle's surface and the environment facilitates gradient optical force [5–7]. As a result the colloid undergoes trapping and manipulation depending on the intensity, polarization and phase profile of the beam. Interaction of the focal field with a metallic object can also lead to scattering of the optical field. Further, the scattered light profile bears the property of the incident beam as well as the scatterer. This effect has been exploited to investigate optical spin-Hall effect [8–13], orbital-Hall effect [14], directional scattering [15–18], as well as angular momentum inter-conversion [19–22].

The light matter interaction with metallic structures can also lead to generation of surface plasmon polaritons − a coupled oscillation of surface charge densities with the incident wave, owing to the availability of free electrons [23, 24]. The consequent sub-wavelength field confinement in metals and plasmonic cavities have been utilized to trap colloids [25], investigate molecular vibrational modes [26, 27], fluorescence detection [26–29] as well as single molecule detection [30–33]. The photon-phonon interaction in metallic objects can generate temperature fields [34, 35]. The resulting optothermal interactions in a fluidic environment with colloidal particles lead to temperature driven migration which may involve multiple processes such as thermophoresis [36–38], thermo-osmosis [39, 40], temperature induced depletion [41] to name a few. In recent years these processes have been studied to investigate the non-equilibrium processes [42] and extensively harnessed for low power optothermal trapping and manipulation [43] as well as reconfigurable nanofabrication processes [44, 45].

To this end, in this thesis we investigate how the light-matter interaction at nano /microscopic scale depends on characteristics of the focal optical field. Specifically, we present experimental and numerical results on forward scattering assisted investigation of focal optical fields from a single crystalline silver nanowire and show simultaneous detection spin and orbital angular momentum as well as spin-Hall effect from linearly polarized light scattering and angular momentum interconversion. We also present results on optothermal interactions due to trapping and heating of thermally active colloids in different optical excitation conditions.

In what follows, we discuss various parameters of optical fields that play crucial roles in most light-matter interactions and give an overview of different effects.

1.1   Properties of an optical field

An optical field can be characterized by its intensity profile, its phase distribution as well as its polarization state [4]. The intensity characterizes the energy (per photon hc/λ) and amplitude carried by the optical field. On the other hand, the phase distribution and its polarization state can modulate the linear momentum and angular momentum constituent of the optical field. Angular momentum of an optical field can be further subdivided into two parts − spin angular momentum (SAM) and orbital angular momentum (OAM) [3]. Engineering the polarization state of any optical field can lead to generation of spin through its two orthogonal left circularly polarized (LCP, σ_+) and right circularly polarized (RCP, σ_-) states [46]. Similarly, engineering the phase distribution of any optical field can generate orbital angular momentum (OAM) [2, 46]. As an example, Laguerre-Gaussian (LG^l_m, l azimuthal index and m radial index) beams, commonly known as vortex beams have helical phase profile through its azimuthally varying phase term i.e. $\exp(il\phi)$ (ϕ azimuthal coordinate and l an integer) and possess corresponding orbital angular momentum state quantified by the topological charge l.

1.1.1   Spin and Orbital flow density

For an optical field with electric field components ($\mathbf{E} = (E_x, E_y, E_z)$) and magnetic field components ($\mathbf{H} = (H_x, H_y, H_z)$), its momentum density ($\mathbf{p}$) is proportional to the Poynting vector ($\mathbf{S}$) and can be subdivided into its spin flow ($\mathbf{p_s}$) and orbital flow constituents ($\mathbf{p_o}$) [47].

$$\mathbf{p} \propto \mathbf{S} = \frac{g}{c}\mathrm{Re}[\mathbf{E}^* \times \mathbf{H}], \tag{1.1}$$

$$\mathbf{p_s} = \frac{g}{4\omega}\mathrm{Im}[\nabla \times (\mathbf{E}^* \times \mathbf{E} + \mathbf{H}^* \times \mathbf{H})] \propto -\mathbf{e_z} \times \nabla_\perp s_3, \tag{1.2}$$

$$\mathbf{p_o} = \frac{g}{2\omega}\text{Im}[\mathbf{E}^* \cdot (\nabla)\mathbf{E} + \mathbf{H}^* \cdot (\nabla)\mathbf{H}]. \tag{1.3}$$

here, $g = (8\pi)^{-1}$ and ω is the oscillating frequency and c is speed of light in vaccum.

For paraxial beams, the spin flow density (SFD, $\mathbf{p_s}$) is a transverse 2D vector field. The physical origin of spin flow is due to rotation of field vectors at each point of the field. It can be understood by considering a simplified picture as shown in fig. 1.1 (a). The situation is equivalent to energy circulation in microscopic loops, which get canceled out if the adjacent cells are identical. The cancellation does not occur whenever there is an inhomogeneity such as at the beam boundary or for transversely inhomogeneous beam (such as Gaussian beam) and results in a net energy flow. Consequently, SFD is proportional to the transverse gradient of the fourth Stokes parameter [48] (i.e., $\propto \nabla_\perp s_3$, $s_3 = I_{\sigma_+} - I_{\sigma_-}$, I is intensity), as shown in equation (1.2). Fig. 1.1 (b) shows the calculated $\mathbf{p_s}$ for left-circularly polarized (LCP, σ_+) and right circularly polarized (RCP, σ_-) Gaussian beams (intensity profile in inset). Arrows indicate the sense of the spin energy flow.

On th other hand, the orbital flow constituent ($\mathbf{p_o}$) of the angular momentum can be obtained from equation (1.3). For a beam carrying only orbital angular momentum (for OAM beams $\mathbf{p} = \mathbf{p_o}$) the transverse orbital flow density ($\mathbf{p_o^\perp}$) originates due to transverse projection of the momentum vector $\mathbf{p_o}$, i.e., $\mathbf{p_o^\perp} \propto \nabla_\perp\varphi$, as shown in fig. 1.1 (c). The
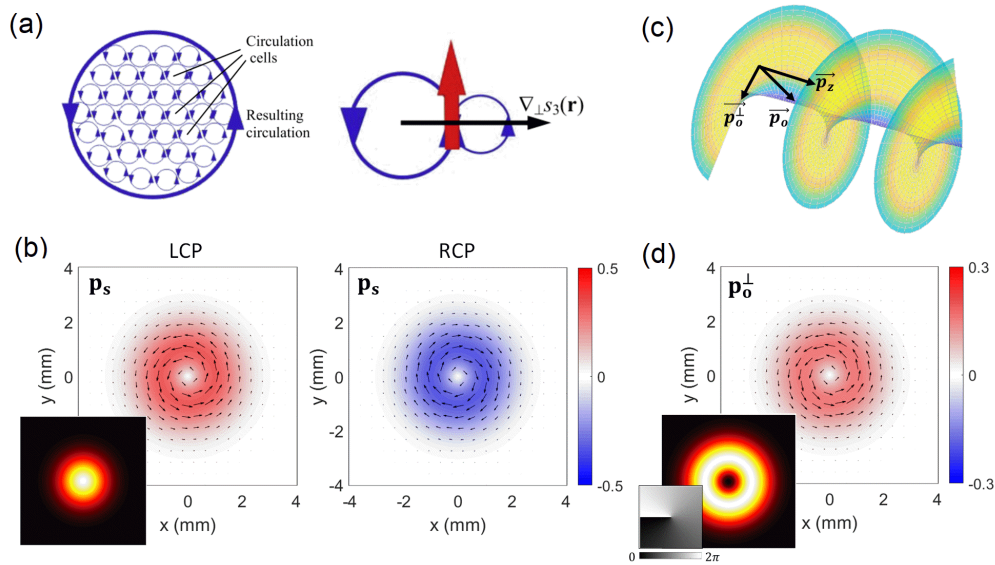
FIGURE 1.1: Transverse energy flow of light beams. (a) The origin of spin flow density can be physically understood by considering microscopic energy loops due to finite boundary of a beam as well as transversely inhomogeneous circularly polarized beam. (b) Numerically calculated spin flow density for left and right circularly polarized Gaussian beam. Inset shows the beam intensity profile. (c) Transverse orbital flow density originates from transverse projection of the momentum vector. (d) Numerically calculated orbital flow density for LG_0^1 beam. Inset shows the corresponding intensity and phase profile. Figure (a) has been adapted from [47] with permission.

longitudinal projection represent the corresponding linear momentum carried by the beam. Fig. 1.1 (d) shows orbital flow density ($\mathbf{p_o^\perp}$) of a paraxial LG_0^1 beam and the inset shows corresponding phase and intensity profiles. The orbital energy flow magnitude and sense depends on magnitude and sign of the topological charge respectively.

In addition to this, focusing of optical fields by means of an objective lens also plays a crucial role in its intensity distribution, polarization as well as phase. These parameters individually or collectively play a key role in all light-matter interactions. In the following section we discuss some prominent examples.

1.2 Examples of light-matter interactions

1.2.1 Optical trapping and manipulation

One of the most prominent examples of light-matter interaction results from radiation force imparted on a micro particle and consequent optical trapping, first demonstrated by Arthur Ashkin [5–7]. It has proven to be a pioneering techniques for high-resolution and three-dimensional manipulation of micro/nano objects. Additionally, introduction of holography has enhanced the versatility of tweezers, where optical intensity, phase as well as polarization has been modulated to manipulate objects and form reconfigurable assemblies [49–51].

The interaction at the particle-environment interface with a focused intense optical field facilitates a gradient optical force, leading to trapping of the particle at the beam center [52]. In addition, the particle also experiences a scattering force proportional to the Poynting vector of the optical field as shown in fig. 1.2 (a). For a spherical colloid of radius $R \leq \lambda$ under the influence of an optical field, the time averaged radiation force ($\langle \mathbf{F} \rangle$) can be given by [52]:

$$\langle \mathbf{F} \rangle = \frac{1}{4}\epsilon_0\epsilon_r \mathrm{Re}(\alpha)\nabla|\mathrm{E}|^2 + \frac{1}{2}\varepsilon_0\varepsilon_r \mathrm{Im}(\alpha)\mathrm{Im}\left(\sum_n \mathrm{E}_n^*\nabla\mathrm{E}_n\right) \tag{1.4}$$

where $\alpha(\omega)$ represents the complex polarizability of the colloid and $n = (x, y, z)$. The fist term in equation (1.4) represents the gradient optical force and the second represents the contribution of scattering force.

A colloid undergoing Brownian motion in a fluidic environment undergoes optical trapping under at the center of a focused Gaussian beam under the influence of the gradient optical force. Fig. 1.2 (b) shows a trapped dielectric melamine formaldehyde colloid due to a focused Gaussian beam at $\lambda = 532$ nm at laser power ≈ 40 mW. The position of the trapped colloid was tracked with the help of video microscopy and the corresponding position distribution ($\rho(x)$) is shown in fig. 1.2 (c). Since the trapped colloid is in thermal
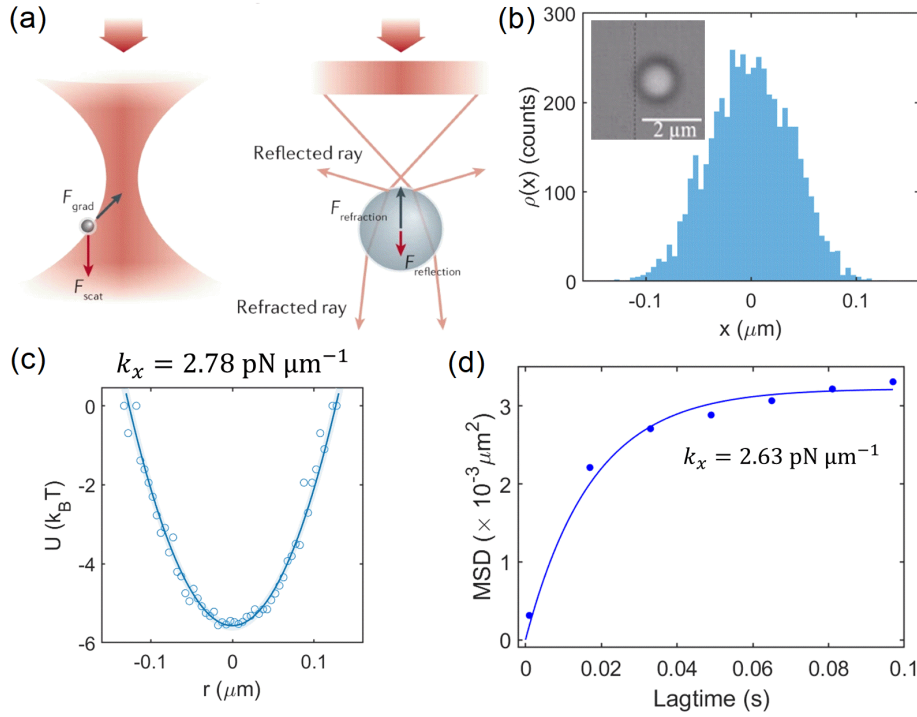
FIGURE 1.2: Optical trapping (a) The optical force at the center of a focused optical beam can be subdivided to optical gradient force (F_{grad}) and scattering force (F_{scat}). (b) Position distribution of a trapped $1\,\mu m$ polystyrene dielectric colloid due to $\lambda = 532$ nm focused beam. Inset shows the micrograph of the trapped colloid. (c) The corresponding optical gradient potential and trap stiffness can be obtained by analysing the position distribution and fitting it with harmonic function. (d) The mean square displacement of the trapped colloid and corresponding trap stiffness. Figure (a) is reproduced from [53] with permission.

equilibrium with the surrounding, the corresponding gradient optical potential ($U(x)$) can be obtained by:

$$U(x) = -k_B T \log[\rho(x)] + U_0 \qquad (1.5)$$

where, k_B is Boltzmann constant, T system temperature and U_0 is a constant. The corresponding trap-stiffness (k_x) of the colloid can be obtained by fitting the gradient optical potential with a harmonic function, i.e., $U(x) = \frac{1}{2} k_x (x - x_{eq})^2$, where x_{eq} is the equilibrium position. Alternatively, trap stiffness can also be obtained by calculating the mean squared displacement (MSD) of the trapped colloid and fitting it with the equation:

$$\text{MSD}_x(\tau) = \langle [x(t+\tau) + x(t)]^2 \rangle = 2\frac{k_B T}{k_x} \left(1 - e^{-|\tau|/\tau_{ot}}\right) \qquad (1.6)$$

where, τ is the lagtime and trap characteristic time $\tau_{ot} = \gamma/k_x$, γ being the friction coefficient. Fig 1.2 (d) shows the fitted MSD. In both cases, the obtained trap stiffness is approximately $\approx 2.7\,\text{pN}/\mu\text{m}$, indicating the corresponding gradient optical force is in $\sim$pN order range.

1.2.2   Generation of surface plasmons and optothermal heating

In metallic objects, the interaction of the time harmonic electromagnetic wave intensity and polarization with the free electrons in the surface leads to coupled oscillations of surface charges and consequent generation of surface plasmons (SPs) at the metal dielectric interface [23, 24]. SPs are sub-wavelength confinement of light at the metal-dielectric interface and evanescent in nature due to large negative permittivity value of metals (see fig. 1.3 (a)). Depending on the nature of the incident field and the geometry of the metallic object, it is possible to generate localized surface plasmon modes or propagating surface plasmon modes, also known as surface plasmon polaritons (SPPs). SPPs have been utilized for plasmonic waveguides [54–56], plasmonic tweezers [25, 57] as well as sensing applications [26, 30, 32].

The light-matter interaction with metallic objects can also lead to generation of heat due to photon-phonon conversion termed as optothermal heating [34, 58]. Fig. 1.3 (b) shows finite element method numerical simulation of generated temperature on a metallic 15 nm Fe_2O_3 nanoparticle (NP) placed on glass substrate in water environment, due to focused Gaussian beam excitation at power 30 mW. The optically induced thermal field has been greatly utilized in the field of thermoplasmonics [34]. Additionally, in fluidic medium with colloidal particles and/or solute molecules the optothermal trapping mechanisms have been employed through thermophoresis[36, 38], thermo-osmosis [39, 40] as well as depletion effects [41]. These mechanisms have enabled low power trapping manipulation [43] as well as wealth of information about the associated non-equilibrium mass transport processes [42].

1.3   Angular momentum mediated interactions

The transverse energy flow associated with the optical beams possessing angular momentum and their interaction with matter have been extensively studied in the context of spin-orbit
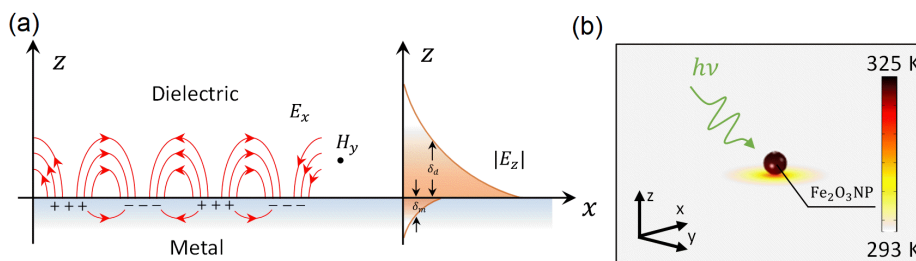
FIGURE 1.3: Generation of surface plasmon and heat. (a) Schematic of generation of surface plasmons at metal-dielectric interface and its evanescent decaying nature. (b) Optothermal heating of an Fe_2O_3 nanoparticle of diameter 15 nm due to focused 532 nm excitation.

and orbit-orbit interactions (SOI) [59, 60]. It has also led to discovering various phenomena such as directional scattering [17], angular momentum interconversion [19] as well as advancement of technologies related to optical communication [61, 62] and optical manipulation techniques [19, 49, 50].

To that end, we discuss the following effects related to the optical angular momentum mediated interaction:

1. Angular momentum mediated scattering

2. OAM controlled optical manipulation

1.3.1 Angular momentum mediated scattering

At sub-wavelength scale, the scattering direction is dependent on the Poynting energy flow of the incident optical beam [60]. Specifically, transverse energy flow mediated by the circular polarization of a Gaussian beam and helical phase of a LG beam play a critical role in light-matter interaction with a scattering object. The resulting spin energy flow or orbital energy flow mediated shift upon reflection or transmission as well as scattering have lead to investigation of spin-Hall [8, 10] and orbital-Hall effects [14]. The effects are optical equivalence of electronic spin-Hall effect exhibiting spin-dependent trajectory of electrons [63, 64]. Fig. 1.4 (a) shows an example photonic spin-Hall effect, where interaction at gold metasurface leads to generation of spin dependent directional surface plasmon polaritons [15]. Similarly, interaction of orbital angular momentum carrying beams with material environment can lead to directional scattering depending on the sign of the topological charge, termed as orbital angular momentum Hall effect or in short orbital-Hall effect. Fig. 1.4 (b) exhibits orbital angular momentum dependent preferential scattering due to interaction of linearly polarized (y polarized) $LG_0^{\pm 1}$ beam with a with a monocrystalline silver nanowire whose long axis is oriented along x axis (see schematic) [18]. The magnitude and sense of the preferential scattering depends on the magnitude and sense of the topological charge.

Various such materialization of nanoscale spin-orbit and orbit-orbit effects have been achieved to investigate photonic spin-Hall effect [17], directional scattering and coupling of SPPs [16, 18] as well as angular momentum interconversion [19–22].

1.3.2 OAM controlled optical manipulation

While optical trapping of micro/nanoscopic particles enabled by strongly focused beam have enabled studying optical forces and lead to application in bio-sensing as well as nanochemistry, the advent of holography have increased its versatility [49, 65]. This is enabled by the presence of diffractive optical elements in the path of an incoming Gaussian beam and
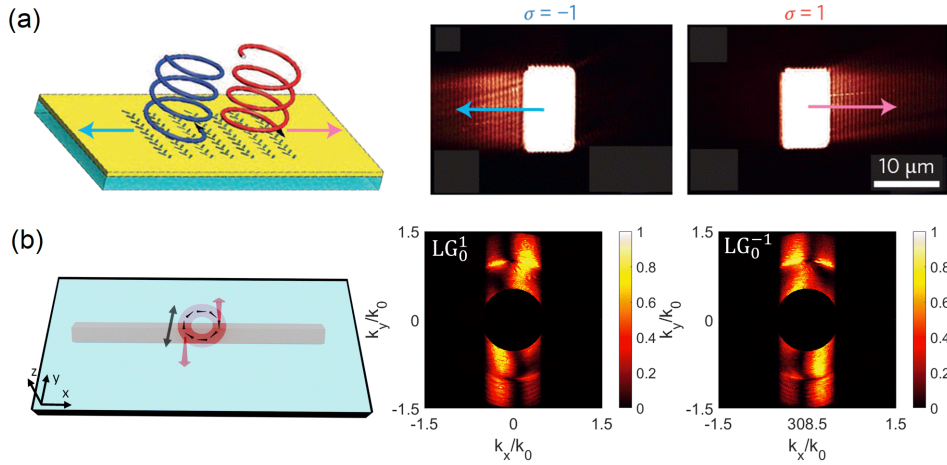
FIGURE 1.4: Angular momentum mediated direcitonal scattering. (a) Spin controlled directional SPP coupling mediated by gold metasurface. (b) Orbital energy flow mediated directional scattering of y polarized LG_0^1 beam from silver nanowire. Figure (a) is reproduced from [15] with permission.

utilizes optical polarization and phase in addition to the optical intensity to increase the versatility of optical tweezers. Such methods have been extensively used to manipulate trapped colloidal objects and are known as holographic optical tweezers [66, 67].

Specifically, introduction of orbital angular momentum carrying beams such as LG beams by introduction of spiral phase plates in the path of a paraxial Gaussian beam or diffracting it from a appropriate diffractive element such as fork diffraction pattern or Fresnel zone plates [46, 68, 69], lead to transverse orbital energy flow mediated manipulation of colloidal objects. In such cases, a trapped colloid in the optical vortex beam travels around its circumference driven by the scattering force originating due to orbital energy flow. One such example is shown in fig. 1.5. Fig. 1.5 (a) shows the beam intensity profile of an LG_0^3 beam focused onto a glass substrate with 100×0.95 NA lens. The corresponding time series of orbital motion of a dielectric trapped $1\,\mu\mathrm{m}$ polystyrene colloid in water along the circumference is shown in Fig. 1.5 (b). The time period of the rotation (ω) can be calculated by tracking the position distribution of the colloid using video microscopy and is found to be $\omega \approx 2.1$ rad/s for this case at laser power ≈ 6.4 mW.

1.4 Outline of the thesis

The work presented in this thesis investigates the light-matter interaction at micro-scale with focused and polarized optical fields. Specifically, the modulation of optical polarization state as well as the phase structure and the resultant optical spin and orbital angular momentum has been utilized for investigation of spin-orbit interactions with a monocrystalline silver
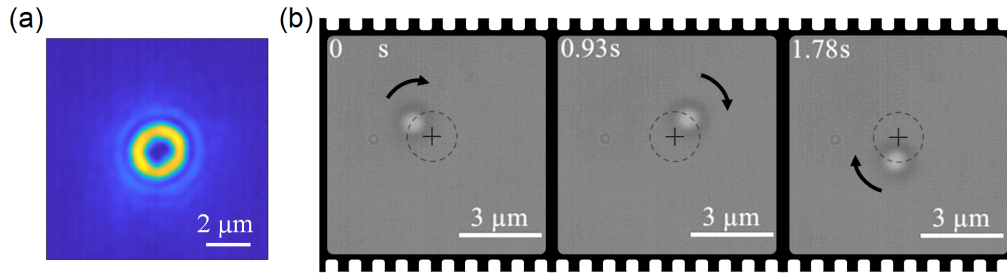
FIGURE 1.5: OAM controlled optical manipulation (a) Intensity profile of LG_0^3 beam at the focus of $100\times$ 0.95 NA lens. (b) Time series of orbital motion of a trapped $1\,\mu m$ polystyrene particle.

nanowire. On the other hand, utilization of optical intensity distribution as well as its linear polarization state allow us to investigate optothermal interactions with self-heating thermally active polystyrene colloids. Therefore, the thesis is broadly divided in two parts - Chapters 3 and 4 investigates the spin-orbit interactions upon scattering from a monocrystalline silver nanowire and chapters 5 and 6 investigates the optothermal interaction of self-heating thermally active colloids in the optical fields. In what follows we outline the structure of this thesis and provide a short summary of each of the chapters.

Chapter 2: Methodology: experimental techniques and numerical calculations

First and foremost, this chapter discusses the various methodologies employed for setting up experimental setup, acquisition of data as well as numerical calculations for corroboration and explanation. More precisely, we have discussed the process for modulation of optical phase distribution and consequent generation of Laguerre-Gaussian beams. Such beams possess orbital angular momentum and therefore have been utilized for investigation of directional scattering. Subsequently, we have discussed the implementation of Fourier plane imaging configurations for detection of directional scattering pattern as well as the architecture of the home-built two channel optical microscope employed for various experiments presented in this thesis. In addition, we have discussed the numerical methods employed for calculation of focal optical fields as well as geometry and module employed for execution of full-wave finite element method based simulations.

Chapter 3: Scattering assisted simultaneous detection of spin and orbital angular momentum of light

This chapter addresses the question - whether it is possible to simultaneously and unambiguously detect the spin and orbital angular momentum states of optical fields using a single nanostructure. To address this, we study the interaction of circularly polarized Laguerre-Gaussian beam with a monocrystalline silver nanowire (AgNW). The associated transverse

energy flow results in angular momentum dependent directional scattering, which can be detected by imaging the Fourier plane. The resulting intensity distribution has been extensively analyzed for extraction of angular momentum information as well as its spin and orbital angular momentum constituents. The method bypasses the complexity of interferometry as well as nanofabricated metasurface based approaches and is a first observation of single nano-object based unambiguous detection of spin and orbital angular momentum of light.

Chapter 4: Experimental observation of optical spin-Hall effect and detection of longitudinal spin density of focused-linearly-polarized light

In this chapter we investigate the generation of longitudinal spin density due to focusing of linearly-polarized Gaussian as well as Hermite Gaussian beams. It has been performed by studying the scattered light from a monocrystalline silver nanowire and circular polarization analysis of the signal. The resulting circular polarization dependent anti-symmetric scattering pattern indicates existence of spin-Hall effect. In addition, the resulting far-field longitudinal spin density is significantly enhanced for Hermite-Gaussian beam compared to the Gaussian beam. The studies are corroborated with focal optical field calculations and finite element method numerical simulations.

Chapter 5: Investigation of optothermal interactions of active colloids in focused and defocused Gaussian beam

This chapter utilizes the optical intensity distribution as well as its polarization state to investigate optothermal interaction of self-heating iron-oxide nanoparticle infused polystyrene active colloids. The thermophoretic as well as self-thermophoretic behavior of the colloids have been investigated to ascertain their dynamics in the optical field which shows a long-range attraction and a short-range repulsion between the colloids. The optical gradient field enabled attraction and the short-range repulsion between the active colloids have been harnessed to form reconfigurable dynamic assembly. In addition, the assembly undergoes self-evolution as a new colloid joins the structure. Further, we show that the incident polarization state of the optical field can be employed as a parameter to modulate the direction of self-thermophoretic motion as well as the structural orientation of the active colloidal matter.

Chapter 6: Orbital angular momentum driven collective motion of active colloids

The aim of this chapter is to investigate the collective dynamics of the assembly of active colloids. To this end, the self-organization and collective motion of polystyrene thermally active colloids driven by orbital energy flow of Laguerre-Gaussian beams has been studied. In doing so, we harness the self-heating and thermophoretic nature of the iron oxide infused

polystyrene colloids to investigate the interparticle interactions of colloids undergoing orbital motion in the illuminated optical field. The resulting short-range repulsion leads to self-evolution of the formed colloidal matter as a new colloid joins the assembly. Consequently, the characteristic collective motion also undergoes modifications. The results have been further investigated by studying their dynamics with respect to increasing laser power as well as introducing a passive dielectric colloid in the assembly, therefore, by modulation of the optothermal interactions.

Chapter 7: Conclusions and future directions

The thesis concludes with this chapter. In this chapter we have summarized the experimental results and the key findings of the work presented in each of the chapters. In addition, for each of the parts - investigation of spin-orbit interactions and investigation of optothermal interactions of active colloids, we provide an outline for extrapolation of the results for future studies.

Chapter 2

Methodology: experimental techniques and numerical calculations

The various light-matter interaction processes and examples described in the previous chapter has not only fundamental importance but also covers a vast realm of technological advancements. For example, optical tweezers have been extensively used in bio physics to study visco-elastic properties of biopolymers [53, 70], as well as single protein molecules, and study cell dynamics [71]. It has also been implemented for mimicking micro motors and studying Brownian dynamics as well as non-equilibrium thermodynamics [72, 73]. On the other hand, angular momentum of light has been extensively studied in context of spin-orbit and chiral light-matter interaction [60], and shown to have great potential for future optical communication devices [61, 62].

The interaction between the characteristic properties of light and matter becomes much more prominent in the sub-wavelength and wavelength-scale limits. For example, strong sub-wavelength confinement of light has enabled investigation of molecular species [27, 33], and cellular structures [74], and scattering from sub-wavelength scale structures have enabled diffraction as well as directional scattering [12, 13, 15]. Therefore, investigation of these light-matter interaction mediated phenomena require high resolution microscopy. In our experimental configuration, this is provided by incidence as well as collection of optical field through high numerical objective lenses. The architecture has enabled precise and selective excitation as well as high resolution acquisition of the desired signal to study the interactions. In addition, the exact nature of the light-matter interaction can be modulated by varying the polarization state of the incident beam as well as the phase, thereby generating structured optical fields.

We have employed Fourier plane (FP) imaging capability with our microscopy, which gives us information about the anisotropy of the emitted/scattered light over a large angular range [4, 75]. This is implemented by imaging the back focal plane of the collecting objective lens through relay optics and projecting onto a charge-coupled device (CCD) [76, 77]. This signal bears the signature of the incident optical field, the scatterer placed at the focal

plane, as well as the nature of the interaction. The analysis of the collected data can give us information of the directionality of the scattered light as well as its polarization state - therefore, enabling us to tailor the light matter interaction accordingly.

The exact nature of the interaction depends on the characteristics of the optical field at the focus. To get an insight into the nature of the optical field at the focal plane, we have employed Debye-Wolf integral formulation to calculate the field intensity as well as polarization distribution [4, 78]. In addition, we have employed finite element method (FEM) based full-wave scattering formulation for numerical investigation of the light-matter interactions. FEM have been also employed to investigate opto-thermal interaction in fluidic environments.

To this end, in this chapter, I will discuss the experimental and numerical techniques employed to investigate various light matter interactions. The first part of the chapter will focus on the experimental configuration used for different studies, namely,

- Phase modulation and generation of structured fields

- Fourier plane imaging technique

- Architecture of the microscope.

The second part will focus on various numerical techniques employed to corroborate the studies as well as understand the mechanisms. This part will be further subdivided into two subsections:

- Calculation of focal optical fields.

- Finite element methods simulations

2.1   Experimental configuration

2.1.1   Phase modulation and generation of structured fields

A Gaussian beam has a plane wavefront at its beam waist, representing that phase is constant at each point in the plane transverse to the propagation direction. As a consequence a Gaussian optical field does not contain any phase singularities i.e., a point or region of zero intensity within the beam envelope around which the phase of the field circulates. In contrast, beams such as Laguerre-Gaussian beams (LG_m^l, l azimuthal order, m radial order) or Hermite-Gaussian (HG_{mn}, m, n nodal line along x, y respectively) possess phase singularities or nodes. These beams are solutions of the paraxial wave equation in cylindrical coordinates and known as higher-order Gaussian modes.

We will look at the specific case of Laguerre-Gaussian beam. An LG beam is given by the equation,

$$u_m^l(r, \phi) \propto \left(\frac{r\sqrt{2}}{\omega_0} \right)^{|l|} L_m^{|l|} \left(\frac{2\,r^2}{\omega_0{}^2} \right) \exp(-\frac{r^2}{\omega_0{}^2}) \exp(il\phi) \qquad (2.1)$$

where, ω_0 is the beam waist radius, $L_m^{|l|}$ is associated Laguerre polynomial function, $\exp(il\phi)$ expresses the linear variation of the phase with azimuthal angle ϕ. l is termed as topological charge or the azimuthal order and indicates the number of twists the helical wavefront undergoes within a wavelength [46, 69]. The magnitude of the orbital angular momentum carried per photon is given by $l\hbar$.

Therefore, the beam can be produced by modulating the azimuthal phase of a conventional Gaussian beam i.e, imparting a azimuthal phase term $\exp(il\phi)$ leading to helical wavefront. One approach of preparing such a beam with helical phase pattern is to pass a plane-wavefront Gaussian beam through an optical element with helical surface known as spiral phase plate as shown in fig. 2.1 (a). It is a transmission element of helicoidal nature, which imparts an azimuthally dependent phase relation on an incident plane wavefront, preserving the beam propagation direction. Alternatively, it is possible to design and fabricate complex diffractive optical elements which can mimic any desired refractive element, with the drawback of working at only single wavelength. On axis spiral Fresnel zone plates is a prominent example [68]. On the other hand, advent of spatial light modulators, offer great advantage as these are liquid crystal operated devices, which can not only be programmed to impart and
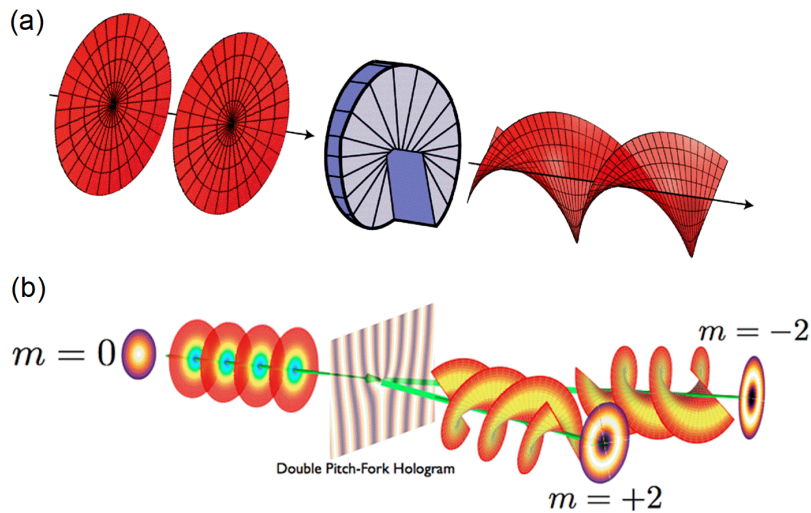
FIGURE 2.1: Generation of Laguerre-Gaussian (LG) beam. (a) Modulation of azimuthal phase of a Gaussian beam having plane wave front can be achieved via spiral phase plates. (b) Diffraction of Gaussian beam through Fork hologram leads to generation of LG beams. Figure (a) is reproduced with permission from [46] and (b) is from [79].
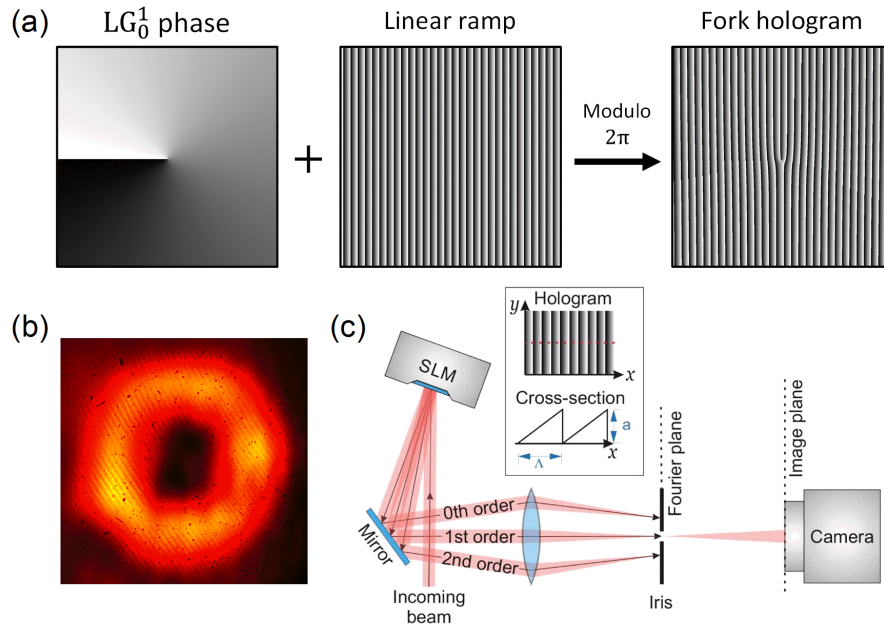
FIGURE 2.2: Generation and implementation of fork diffraction holograms in SLM. (a) Fork diffraction pattern can be generated by adding azimuthal phase distribution to a linear ramp and expressing the sum as modulo 2π. (b) Corresponding intensity distribution of generated LG_0^1 beam. (c) Implementation of phase modulation by employing a SLM. Figure (c) is reproduced with permission from [81].

create different wave fronts, but can also have a large range of operating wavelengths [46]. Projection of appropriate diffraction patterns onto these devices are done through a video interface of a computer and the desired optical fields are produced at the first diffraction order as shown in fig. 2.1 (b).

The diffraction pattern is generated by adding a desired phase distribution (of the desired beam) to a linear ramp and the sum expressed as modulo 2π. Fig. 2.2 (a) shows the generation of forked diffraction grating [80]. The corresponding LG beam pattern is shown in fig. 2.2 (b). A central dark intensity region indicates the phase singularity. Fig. 2.2 (c) shows the typical off axis operation of a SLM [81]. The linear polarization of the incoming beam is aligned with respect to the extraordinary axis of liquid crystal. The SLM used in our experiments have resolution 1024×768 with pixel pitch $19\,\mu$m. The manufacturer calibrates the SLM at each pixel to have a linear response to the control voltage, given by a 8-bit number which indicates the gray level of the projected hologram pattern. The first order diffraction pattern is filtered out with the help of an iris and routed to the microscope objective with the help of mirror and lenses.

2.1.2 Fourier plane imaging technique

Fourier plane microscopy has emerged to be an important tool to study emission and scattering properties of nano-photonic systems such as quantum emitters, optical nano structures and associated light-matter interactions [4, 75, 76]. For example, it has been employed to ascertain orientation of single molecules [82] as well as directivity of optical antennas [27] with the common goal of quantitative measurement of angular radiation spectrum. In typical microscopy setup, the Fourier plane (FP) information is obtained by imaging intensity distribution at the back focal plane (BFP) of an objective lens [75–77].

The optical field emanating from the focal plane of the lens can be represented by a weighted sum of plane wave components, traveling along different directions angles given by (θ_x, θ_y). An objective lens separates these plane wave components and transforms them into paraboloidal waves which converge to a point at the back focal plane of the lens [75]. As shown in the fig. 2.3 (a), any plane wave traveling along direction given by the angles (θ_x, θ_y), is focused onto a point $(\theta_x f, \theta_y f)$, f is the focal length of the lens. Therefore, each direction is mapped by a point in the back focal plane (BFP) of the objective lens and hence gives us information about the angular radiation spectrum. In a high-resolution microscopy setup, the emitted/scattered light collected with the help of an high numerical aperture objective lens and the corresponding Fourier plane is projected to an external imaging device by means of external optics.
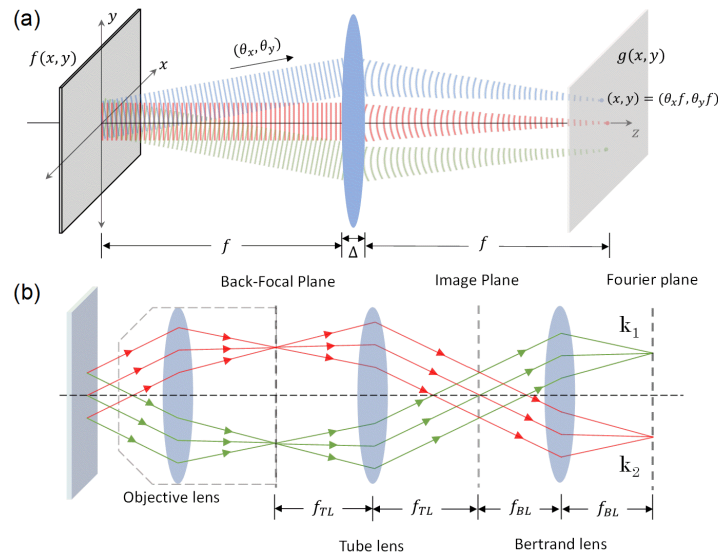
FIGURE 2.3: Concept and implementation of Fourier plane imaging. (a) Schematic showing transformation of emanating plane waves from a focal plane of a lens to paraboloidal waves due to a lens, and their convergence to points, hence mapping the direction. (b) $4f$ configuration for imaging of the Fourier plane using three components, namely objective lens, tube lens (TL) and Bertrand lens(BL). k_1 and k_2 are wave-vectors, f_{TL} and f_{BL} are focal lengths of TL and BL respectively. Figure (a) reproduced with permission from [75].
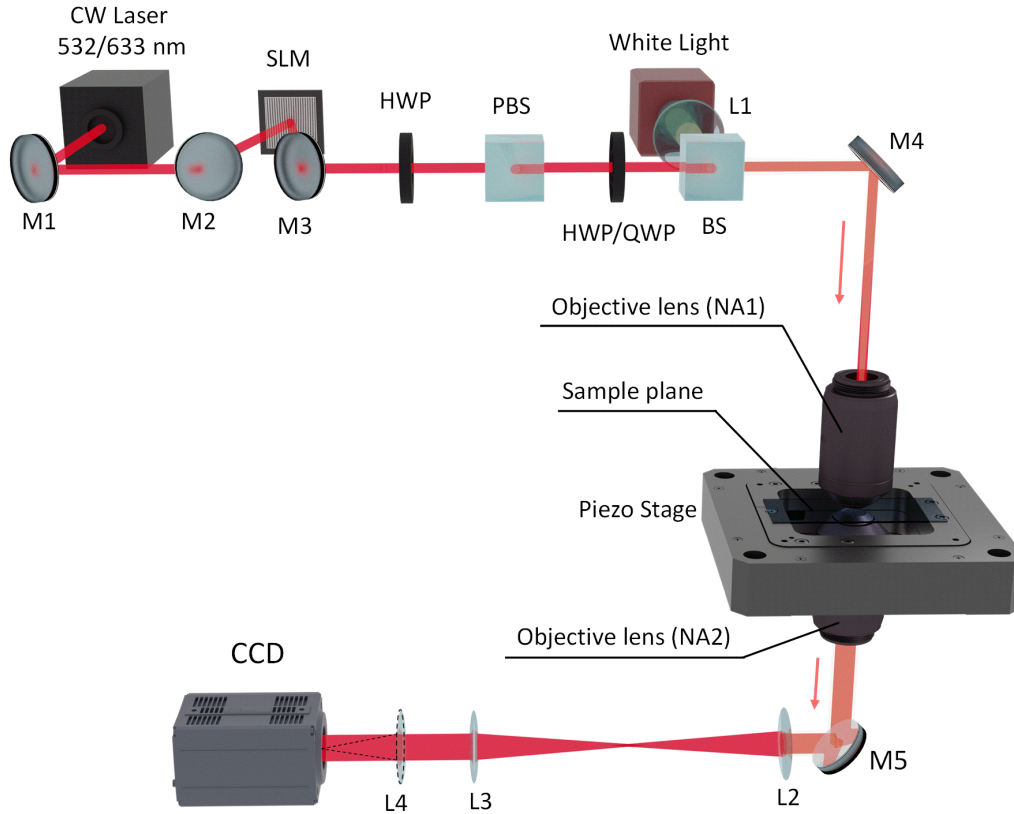
FIGURE 2.4: Architecture of the microscope. A two-channel optical microscope is employed for the experiments. The upper objective lens (NA1) is used to focus incident CW laser at wavelength λ = 633 or 532 nm and lower higher numerical aperture objective lens (NA2, NA2 > NA1) collects the desired signal. Incident laser can be structured by employing a SLM. The power is modulated by using a combination of half-wave plate (HWP) and polarizing beam splitter (PBS). The collected light is routed towards the detection device with the help of mirrors and lenses. M1-M5: mirros, L1-L4 lenses.

Implementation: Fourier microscopy typically involves three components: a microscope objective along with a tube lens and a Bertrand lens, which acts as a two-lens optical system used to image the BFP of the objective lens. Fig. 2.3 (b) shows an implemented $4f$ configuration for imaging the BFP [76]. In $4f$ configuration, a tube lens (TL) is placed a focal length (f_{TL}) away from the BFP of the objective lens. TL transforms the collected FP from the BFP of the objective lens to real plane image. Another lens, termed as Bertrand lens (BL) is placed focal length (f_{BL}) away from this real plane, which transforms this information back to FP at f_{BL} away and projects onto a CCD. Therefore, the light emanating from the focal plane in a given direction is focused onto singular points (k_1) at the FP, hence, allowing us to measure the wave-vector distribution of the optical field of interest.

2.1.3 Architecture of the microscope

The experimental configuration implemented for various light-matter investigations prsented in this thesis, is shown by the schematic in fig. 2.4. A home-built two-channel microscopy system has been used for the studies. The setup consists of two objective lenses with lower objective lens (numerical aperture NA2) having larger numerical aperture than the upper objective lens (NA1), i.e., NA2 > NA1. The experiments have been performed in the transmission configuration i.e., upper objective lens is used for excitation of the sample placed on a piezo stage and the lower objective lens has been used to collect the desired signal. The experiments have been performed with continuous wave (CW) laser illumination at wavelength $\lambda = 532$ or 633 nm. The laser can be directly used for experiments with Gaussian beam or can be routed towards an off axis phase-only spatial light modulator (SLM) with the help of mirrors (M) for experiments related to structured beams. A combination of half-wave plate (HWP) and polarizing beam-splitter (PBS) has been used to modulate the incident laser power. The polarization of the incident beam can be modulated with the help of half-wave plate (HWP) or quarter-wave plate (QWP). The collected signal both in real and Fourier plane is routed towards a charge-coupled device (CCD) using combination of lenses (L) and mirrors (M). Additional placement of analyser, QWP as well as filters in the collection path allows for investigation of various parameters of the optical field as well as the system under study. In addition to the versatility of the operating parameters of the system the experimental design allows us to independently modulate the focusing conditions of the excitation beam from the collection path.

2.2 Numerical calculations

2.2.1 Calculation of focal optical fields

The nature of the light-matter interaction at microscopic scale is dependent on the nature of the focal optical fields. Focusing of a paraxial optical beam through an objective lens leads to complex non-paraxial distribution of the optical fields. To get an insight into the nature of the focal optical fields, we have employed Debye-Wolf integral representation [4, 78, 83]. Considering an objective lens represented by parameters focal length f, numerical aperture $\mathrm{NA} = n_1 \sin(\theta_{max})$ (n_1 refractive index of the medium), the focal optical field for an incident paraxial beam with electric field amplitude $\mathbf{E_{in}}$ and wave vector $k = k\,\hat{\mathbf{z}}$ can be obtained by,

$$\mathbf{E}(\rho, \varphi, z) = -\frac{ikf\, e^{-ikf}}{2\pi} \int\limits_{0}^{\theta_{max}} \int\limits_{0}^{2\pi} \mathbf{E_{ref}}(\theta, \phi)\, e^{ikz\cos\theta} e^{ik\rho\sin\theta\cos(\phi-\varphi)} \sin\theta\, \mathrm{d}\phi\, \mathrm{d}\theta \qquad (2.2)$$

$$\mathbf{E_{ref}} = [t^s[\mathbf{E_{in}} \cdot \mathbf{n}_\phi]\mathbf{n}_\phi + t^p[\mathbf{E_{in}} \cdot \mathbf{n}_\rho]\mathbf{n}_\theta]\sqrt{\cos\theta} \qquad (2.3)$$

The formulation takes into account both the refraction of the paraxial beam at the lens spherical surface ($\mathbf{E_{ref}}(\theta, \phi)$) as well as the focusing thereafter as shown by the geometry in fig. 2.5 (a). t^s and t^p are the transmission coefficients corresponding to s and p polarized electric field components respectively. $\mathbf{n}_\rho$ and $\mathbf{n}_\phi$ represents the unit vectors of a cylindrical coordinate system whereas the unit vectors of a spherical polar coordinate are given by $\mathbf{n}_\theta$ and $\mathbf{n}_\phi$, origin of the coordinate system being the focal point $(x, y, z) = (0, 0, 0)$, as shown in fig. 2.5 (a). n_1 and n_2 represent the medium refractive index.

Fig. 2.5 (b) shows the focal electric field intensity distribution ($I = \varepsilon_0 |\mathbf{E}|^2$) due to focusing of the paraxial x polarized Gaussian beam at wavelength $\lambda = 633$ nm, propagating along the z axis by 0.5 NA objective lens. The corresponding intensity distribution of the x polarized ($I_x = \varepsilon_0 |E_x|^2$), y polarized ($I_y = \varepsilon_0 |E_y|^2$) and z polarized ($I_z = \varepsilon_0 |E_z|^2$) constituent of the total electric field is shown in fig. 2.5 (c). In comparison to polarized
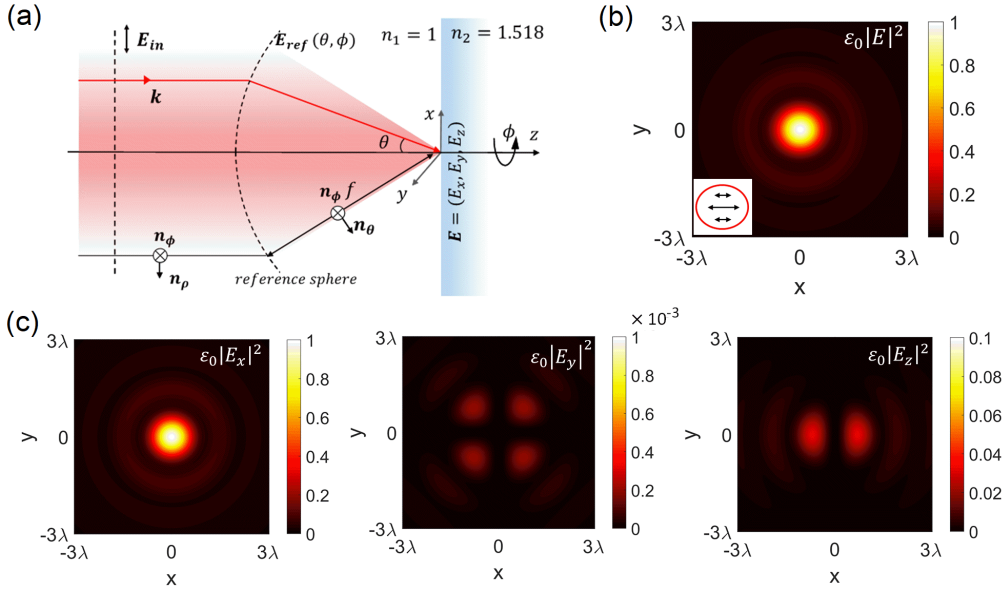
FIGURE 2.5: Calculation of focal optical fields (a) Schematic of the focusing configuration. The incident field ($\mathbf{E_{in}}$) gets refracted by the spherical lens surface, with focal length f and leads to generation of refracted field ($\mathbf{E_{ref}}$). Consequent focal electric field components are given by $\mathbf{E} = (E_x, E_y, E_z)$. (b) Focal electric field intensity distribution due to focusing of incident x polarized Gaussian beam. (c) Corresponding intensity distribution of x, y and z polarized component of the total electric field.

paraxial optical fields, the vectorial nature of the focal optical fields are much more intense owing to the stronger z component of the field, and therefore leads to generation complex polarization structures. Calculation of focal optical fields allow us to investigate focal optical field characteristics such as Poynting energy flow as well as its spin and orbital constituents. The knowledge of focal optical fields also enables numerical investigation of the resultant light-matter interaction mediated effects such as optical forces and optical heating as well as inter-conversion of angular momentum components in specific cases [19].

2.2.2 Finite element method simulations

In addition to the calculation of the focal optical fields we have employed finite element method simulations (FEM) to corroborate the experimental results, gain insight about the optical interactions for effects such as directional scattering, optical forces as well as optothermal effects. FEM subdivides a large geometry to finite elements through space discretization, achieved through meshing. Thereby, the concerned partial differential equations are numerically solved in each discretized domain with appropriate boundary conditions by minimizing an associated error function. For our studies, we employed commercial software COMSOL Multiphysics 5.5 for FEM simulations. In the following paragraphs, we describe a finite element method simulation geometry and results employed for investigation of elastic scattering from silver nanowire.

For numerical investigation of light-matter interactions, Maxwell's equations are numerically solved. This is performed by incorporating the wave-optics module and solving it to find the steady state solution. Fig. 2.6 (a) shows a typical geometry employed for investigation of scattering of linearly polarized Gaussian beam from a plasmonic silver nanowire (AgNW) [13]. AgNW have been modelled using a pentagonal cross-sectional geometry of length $5\,\mu\text{m}$ and width 350 nm, with refractive index set to Ag at 633 nm wavelength, placed on a cuboid geometry set to mimic glass substrate. The Gaussian beam is set to incident through a port of $2.5\,\mu\text{m} \times 2.5\,\mu\text{m}$ and the beam waist was kept ≈ 633 nm to mimic the focusing conditions. The entire geometry was meshed by employing tetrahedral meshing with minimum dimension 50 nm. Appropriate scattering boundary conditions were applied to avoid spurious reflections from the boundaries of the simulation geometry. This formulation provides qualitative investigation of the problem and not an exact ones as it is very difficult to mimic the exact strong focusing conditions, as achieved in experiments with the help of objective lenses.

In addition to the geometry described in the previous paragraph, an inner cuboid geometry of dimension $5.5\,\mu\text{m} \times 3\,\mu\text{m} \times 2\,\mu\text{m}$ is employed for calculation of far-field scattering pattern, given by the Fourier plane in experiments, based on reciprocity arguments [84]. It is achieved by integrating MATLAB via livelink feature of COMSOL Multiphysics. Fig. 2.6
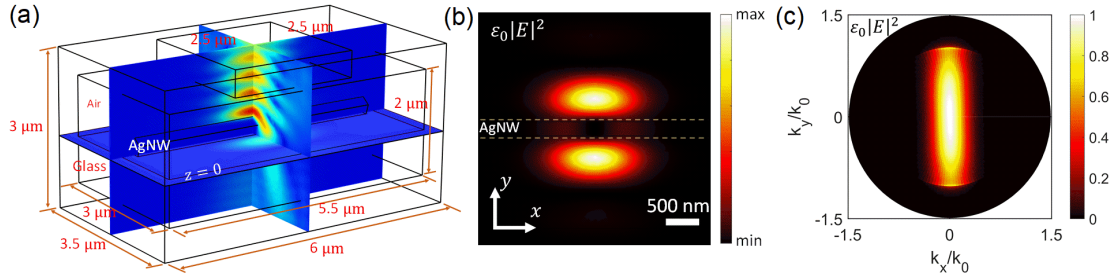
FIGURE 2.6: Numerical calculation of scattered optical fields. (a) Schematic of the numerical simulation geometry. (b) Numerically simulated scattered electric field intensity distribution at the focal plane ($z = 0$) corresponding to x polarized Gaussian beam incidence. (c) Corresponding Fourier plane intensity distribution with collection numerical aperture set to 1.49 NA is calculated by employing reciprocity arguments.

(b) shows the numerically calculated scattered near field electric field intensity distribution at $z = 0$ plane for x polarized incident Gaussian beam (see [13]). Fig. 2.6 (c) shows the corresponding forward scattered far-field intensity distrbution or Fourier plane intensity distribution where the maximum numerical aperture of collection is set to 1.49 NA, through the glass substrate. The Fourier plane intensity distribution is plotted in k_x and k_y axes which are basically the Fourier transform of the spatial coordinates (x and y axes). In the following chapters we will discuss the implications of the wave-vector distribution through analysis of the Fourier plane intensity distribution.

The numerically calculated optical fields can also be employed to calculate the optical force on objects placed on the focal plane by employing Maxwell upward stress tensor formulation and will be discussed in the context of optical trapping and binding in Chapter 5. On the other hand, opto-thermal interactions in fluidic environments are investigated by coupling the heat diffusion equation with the Navier-Stokes equation. Within the COMSOL Multiphysics 5.5 environment, it is achieved by interfacing the heat-transfer module with the laminar flow module through non-isothermal flow coupling module. The results will also be discussed in the context of opto-thermal interactions in Chapter 5.

Chapter 3

Scattering assisted simultaneous detection of spin and orbital angular momentum of light

Abstract:

In this chapter, I will discuss about preferential scattering from single nano-structure, namely a mono-crystalline silver nanowire (AgNW) due to its interaction with optical beams having transverse energy flow owing to their angular momentum state. Specifically, by employing Fourier plane (FP) microscopy, we show how elastic scattering pattern from AgNW can be analyzed for the simultaneous detection of spin and orbital angular momentum of incident optical beam. The method bypasses the complexity of interferometry as well as nanofabricated metasurface based approaches and is a first observation of single nano-object based unambiguous detection of spin and orbital angular momentum of light. This chapter is an adaptation of the research article "Laser & Photonics Reviews 2022, 16, 2200049, (arXiv:2111.14919)" [85].

3.1 Introduction and motivation

In an optical field, the spin angular momentum (SAM) is manifested through its circular polarization states and orbital angular momentum (OAM) is manifested through helical phase front [2, 3]. SAM can have two orthogonal states corresponding to left- and right-circularly polarized light, whereas OAM is theoretically unbounded with its infinite orthogonal states, corresponding to the topological charge of vortex beams such as Laguerre-Gaussian beams (LG_m^l, l topological charge, m radial index) [46]. However due to finite aperture size, space-bandwidth only finite number of basis states can be produced.

Hence, in recent years, deterministic sensing of SAM and OAM state of an optical field has become a relevant problem. Detection of OAM in macroscopic scale has been achieved through conventional interferometry [86–88], as well as diffraction [89–92] and projection
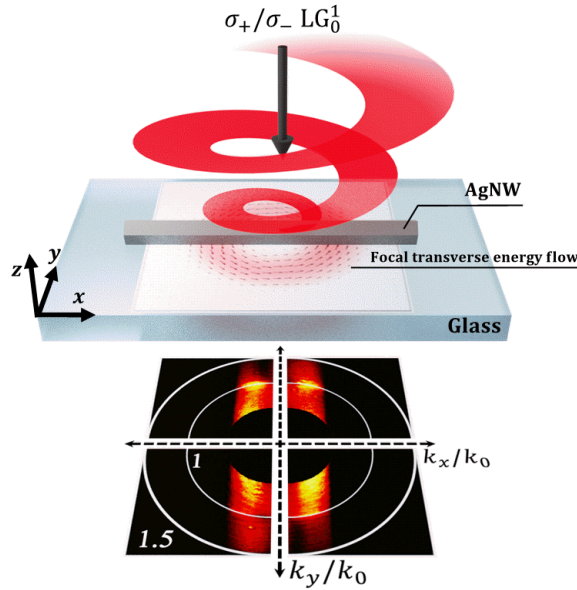
FIGURE 3.1: Schematic of the experimental configuration. An AgNW is placed on a glass substrate and the scattered LG beam intensity distribution in the Fourier plane is analyzed to determine the angular momentum state.

through a reciprocal forked diffraction grating [93]. The complexity of optical setups of these methods have been overcome through the advancement of nanofabrication methods. It has enabled nanoscale generation [94, 95], as well as detection of OAM and SAM states [96–98]. The sub-wavelength operation of on chip plasmonic devices offer great advancement from the interferometric based techniques with their lower footprint but with the inherent requirement of complex fabrication methods.

Therefore, it is imperative to find a method which are devoid of either complication optical setups as well as complex nanofabrication methods. In addition, deterministic and simultaneous sensing of spin and orbital angular momentum component of a light beam using a single nano-object is yet to be achieved. This motivated us to propose a angular momentum state detection mechanism based on scattering from a chemically synthesized quasi-one-dimensional monocrystalline silver nanowire (AgNW).

The solution phase simple synthesis method enables necessary tunability of their size as well as their self-assembly on any desired substrate [99, 100]. The uniform nature of the morphology renders them useful for low loss surface plasmon waveguiding property [56] and makes them ideal for fundamental photonic circuit applications such as plasmonic waveguide [56, 101], plasmonic antenna [27, 102] and logic gates [103]. In addition, our previous reports indicate that AgNW can act as a plasmonic scatterer and sense total transverse energy flow of an incident beam [12, 18], as well as spin densities [13].

The presented approach requires dropcasting of AgNWs on a glass substrate and a single

AgNW has been used as a nanoscopic strip diffractor. The OAM and SAM state of the incident optical field has been determined by analysis of the Fourier plane intensity distribution of the scattered light, as shown in fig. 3.1. Consideration of the total transverse energy flow as well as the individual component due to spin flow and orbital flow at the focus allows distinction of individual effect on the scattering pattern, therefore, enabling their detection.

In the following section, we numerically calculate the total transverse energy flow, its spin and orbital constituent and study the resultant scattering patterns.

3.2 Theoretical calculation of the transverse energy flow

The first step for determination of spin angular momentum (SAM) and orbital angular momentum (OAM) is to ascertain their contribution to the transverse energy flow of the beam [47]. As discussed in chapter 1, a Laguerre Gaussian (LG_m^l) beam, owing to its helical wavefront, can possess transverse energy flow corresponding to its orbital flow density ($\mathbf{p_o^\perp}$). The magnitude and the sense of flow gets dictated by the magnitude and sign of the topological charge (l) of the beam. On the other hand, the transverse energy flow in circularly polarized beam originates due to its spin flow density ($\mathbf{p_s}$), the sense of which gets dictated by the handedness of the circular polarization. At the focal plane these quantities can be obtained by employing Debye-Wolf integral formulation [78, 83], as discussed in chapter 2.
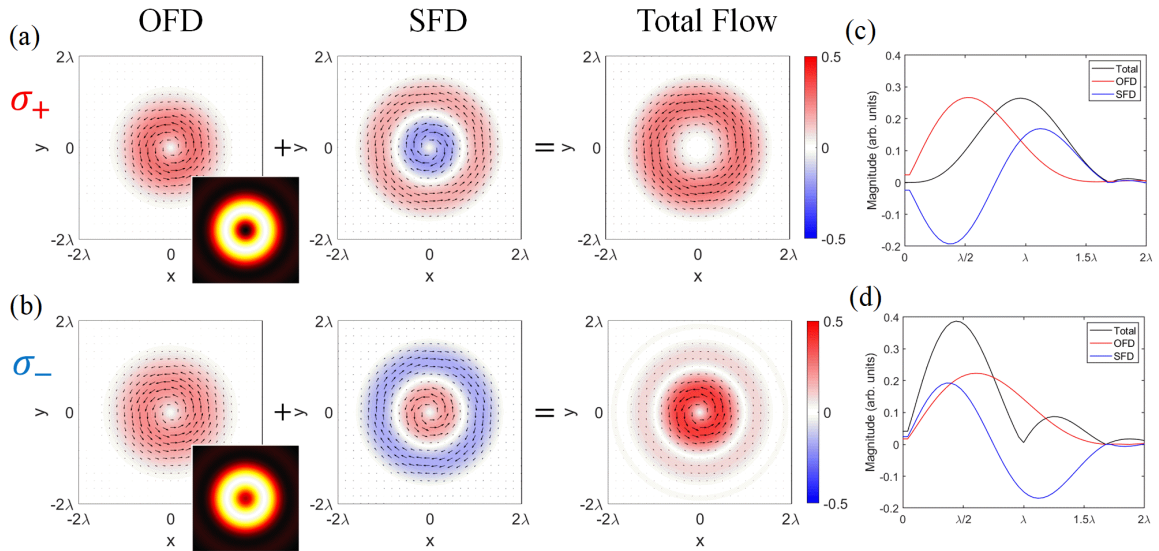
FIGURE 3.2: Calculation of focal transverse energy flow constituents. Calculated focal orbital flow density (OFD, $\mathbf{p_o^\perp}$), spin flow density (SFD, $\mathbf{p_s}$) and total transverse energy flow ($\mathbf{p^\perp}$) distribution for (a) left-circularly polarized (σ_+) and, (b) right-circularly polarized (σ_-) LG_0^1 beam. Inset shows the corresponding total field intensity. (c) and (d) represents the $\mathbf{p_o^\perp}$, $\mathbf{p_s}$ and $\mathbf{p^\perp}$ line profile along x axis from 0 to 2λ.

Fig. 3.2 (a) and (b) show the calculated OFD, SFD and total transverse energy flow density ($\mathbf{p}^\perp = \mathbf{p_s} + \mathbf{p_o}^\perp$) corresponding to left-circularly polarized (σ_+) and right-circularly polarized (σ_-) LG$_0^1$ beams at wavelength $\lambda = 633$ nm. The inset shows the total electric field intensity at the focal plane. As expected, for both σ_+ and σ_- polarized LG$_0^1$ beam, the $\mathbf{p_o}^\perp$ has similar magnitude and similar counter-clock orbital flow sense. But, for σ_+ LG$_0^1$ beam, the $\mathbf{p_s}$ has both clockwise and counter-clock energy flow in its inner and outer part respectively. Additionally, the magnitude of $\mathbf{p_s}$ is higher in its inner radius ($|\mathbf{p_s}| = 0.1085$ at $R = 0.322\lambda$) and lower in its outer radius ($|\mathbf{p_s}| = 0.0731$ at $R = 1.068\lambda$). It is exactly opposite for the σ_- LG$_0^1$ beam. Hence, for σ_+ LG$_0^1$ beam, counter-clock orbital flow towards the center cancels the clockwise spin flow, whereas, in the outer part the counter-clock spin flow gets added up with orbital flow, resulting an overall counter clock total transverse energy flow. This results in the transverse energy flow having a maximum magnitude of $|\mathbf{p}^\perp| = 0.1515$ at radius $R = 0.868\lambda$. For σ_- LG$_0^1$ the counter-clock inner spin flow gets added up with the counter-clock orbital flow resulting in higher counter-clock transverse energy flow, $|\mathbf{p}^\perp| = 0.2551$ at $R = 0.4\lambda$. The line profile of $\mathbf{p_s}$, $\mathbf{p_o}^\perp$ and $\mathbf{p}^\perp$ at the focal plane from 0 to 2λ corresponding to σ_+ and σ_- polarized LG$_0^1$ beams are shown in fig. 3.2 (c) and (d) respectively. In this context, it is important to point out the subtle differences of the intensity profile for σ_+ and σ_- polarized LG$_0^1$ beams as focusing of circularly polarized LG beam aids spin-to-orbital angular momentum transformation [19].

3.3 Detection of Fourier plane intensity distribution

The angular momentum state enabled focal transverse energy flow leads to flow dependent forward scattering pattern upon interaction with a nano structure, which can be detected through Fourier plane (FP) imaging. The implementation of forward scattering configuration is achieved by dropcasting AgNWs of width ≈ 350 nm onto a glass cover-slip, which acts as a nanoscopic strip scatterer [89, 92], and placing it on a piezo stage. The incident optical field is focused using a 50×0.5 NA objective lens and a 100×1.49 NA lens has been used in transmission configuration, for collection of the scattered signal (see section 2.1.3 of chapter 2), as shown in fig. 3.3 (a). FP intensity distribution of the forward scattered light was collected by projecting the back focal plane of the collection objective lens onto a CCD using relay optics [76, 77] (see section 2.1.2 chapter of 2). The collected FP intensity distribution can be divided into two regions, sub-critical region (NA < 1) and super-critical region (NA > 1). The incident NA part (NA $0 - 0.5$) in the sub-critical region is dominated by the un-scattered incident light, and is omitted from our analysis, appears as a black disk at the center of the measured FP. The detection mechanism works at a low power illumination, a very low power of $0.13\,\mu$W has been used for the scattering of LG$_0^{\pm 1}$ beam.
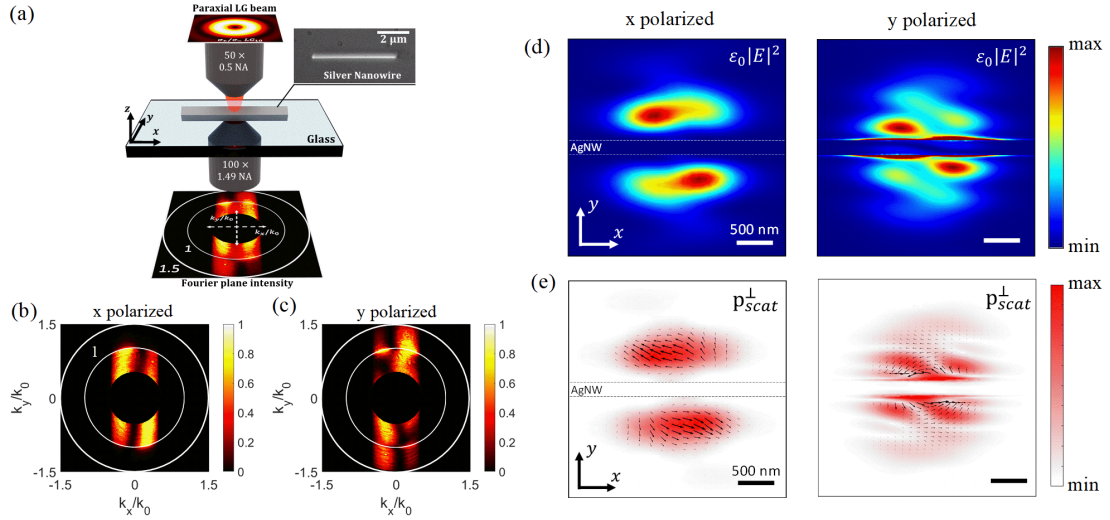
FIGURE 3.3: Experimental implementation and polarization dependent scattering pattern. (a) Experimental configuration for the Fourier plane (FP) imaging. Inset shows the bright field optical micrograph of AgNW. Measured FP intensity distribution for scattering of (b) x polarized and, (c) y polarized LG_0^1 beam. Inner and outer white circles represent the critical angle at the air-glass interface and the collection limit of the objective lens NA respectively. Incident NA region is blocked and appears as a black disk at the center. (d) Simulated near-field electric field intensity distribution at the air-glass interface for x and y polarized incident beam. (e) Corresponding scattered total transverse energy flow density ($p_{scat}^{\perp}$) distribution for x and y polarized LG_0^1 beam. The black arrows indicate the energy flow direction.

3.4 Polarization dependence of scattering pattern

To determine the contribution due SAM and OAM in the scattered FP, it is imperative to understand the scattered FP patterns of its constituent linear polarization components.

Incidence of longitudinally polarized (x polarized) optical field on a nanowire with long axis along x axis leads to signal in sub-critical region. Since the longitudinal length of the nanowire is not comparable to the wavelength, it does not lead to significant field enhancement at the nanowire edges, leading to reflective behaviour. On the other hand, for transversely polarized optical fields (y polarized) and lead to near-field (NF) at the NW edges. The evanescent NF gets partially converted into propagating waves at the air-glass interface and can be observed in the supercritical region of the far field intensity distribution. Therefore, for transversely polarized incident field signal can be observed in both sub- and super-critical region of the FP. The respective cases are shown in fig. 3.3 (b) for x polarized incident beam and fig. 3.3 (c) for y polarized incident LG_0^1 beam, where the nanowire's long axis is oriented along x axis. In fig. 3.3 (b) and (c) the inner white circle represents the critical angle at the air-glass interface and outer white circle represents the collection limit of the objective lens.

In addition to polarization dependent signature, the recorded FP intensity distribution

exhibit directional/preferential scattering pattern due to orbital energy flow present in these beams [18, 47]. But, the preference for x polarized case is opposite to that of y polarized case. This can be attributed to the polarization dependent interaction of the NW with the incident beam as shown through numerical simulation in fig. 3.3 (d) and (e). The finite element method simulation employed for these results have been described in section 2.2.2 of chapter 2. For x polarized LG_0^1 beam the field gets scattered from the NW and the corresponding total transverse energy flow ($\mathbf{p}_{\mathbf{scat}}^{\perp}$) points away from the NW and opposite to the incident beam $\mathbf{p}^{\perp}$. On the other hand, y polarized LG_0^1 beam aids the interaction of the transverse energy flow with the nanowire and leads to generation of evanescent near-field at nanowire edges, apparent with the presence of scattered light signal in the super-critical region of FP in fig. 3.3 (c). Consequently, the scattered field $\mathbf{p}_{\mathbf{scat}}^{\perp}$ flow is along the same direction as that of the incident beam. Thus, a nanowire through its scattering can detect OAM modes as well as its linear polarization states. The effect is qualitatively similar to a nanoscopic strip scatterer [89, 92].

In addition, it is possible to ascertain the polarization of the scattered light, by placing an analyzer in the collection path. Fig. 3.4 (a) shows FP intensity distribution of x polarized $LG_0^{\pm 1}$ beam and corresponding E_x and E_y analyzed intensity distribution. Therefore, the polarization of the scattered light for the x polarized incident beam is predominantly x polarized. Similarly, for y polarized beam scattering, the light scattered in the sub- and super-critical region is mostly y polarized, as shown in 3.4 (b). Similarly, the E_x and E_y polarization component analyzed FP intensity distributions for σ_+ polarized incident beam, shown in fig. 3.4 (c), indicates that x polarized component contributes to signal in the sub-critical region, where as, signal for the y polarized component appears in both sub- and super-critical region. Therefore, we can recover the FP intensity distribution for x and y polarized intensity distribution as shown in fig. 3.3 (b) and (c) respectively. Thus, for scattering of circularly polarized LG_0^1 beam, the state of circular polarization can be determined by analyzing the sub-critical region intensity distribution as only in this regime both in-plane x and y components of polarization scatter. Whereas, in super-critical region, predominantly scattered light is from y polarized field and will posses information about OAM state of the incident beam.

3.5 Simultaneous Detection of optical angular momentum state

3.5.1 Detection of OAM and SAM for fist order LG beam

To understand the scattering assisted spin and orbital angular momentum detection mechanism, we investigate the FP intensity distribution for σ_+ and σ_- polarized $\mathrm{LG}_0^{\pm 1}$ beam. Fig. 3.5 (a) and (b) shows the FP intensity distribution for σ_+ and σ_- LG_0^1 beam respectively. The intensity distribution has been analyzed by division of the pattern into four parts looking into the intensity distribution of either upper ($k_y > 0$ region) or lower half ($k_y < 0$ region). In addition, since SAM and OAM can be obtained by analysis of the signal in the sub-critical and super-critical region, the intensity distribution in sub- and super-critical region have been individually considered. Fig. 3.5 (c) and (d) shows the intensity distribution
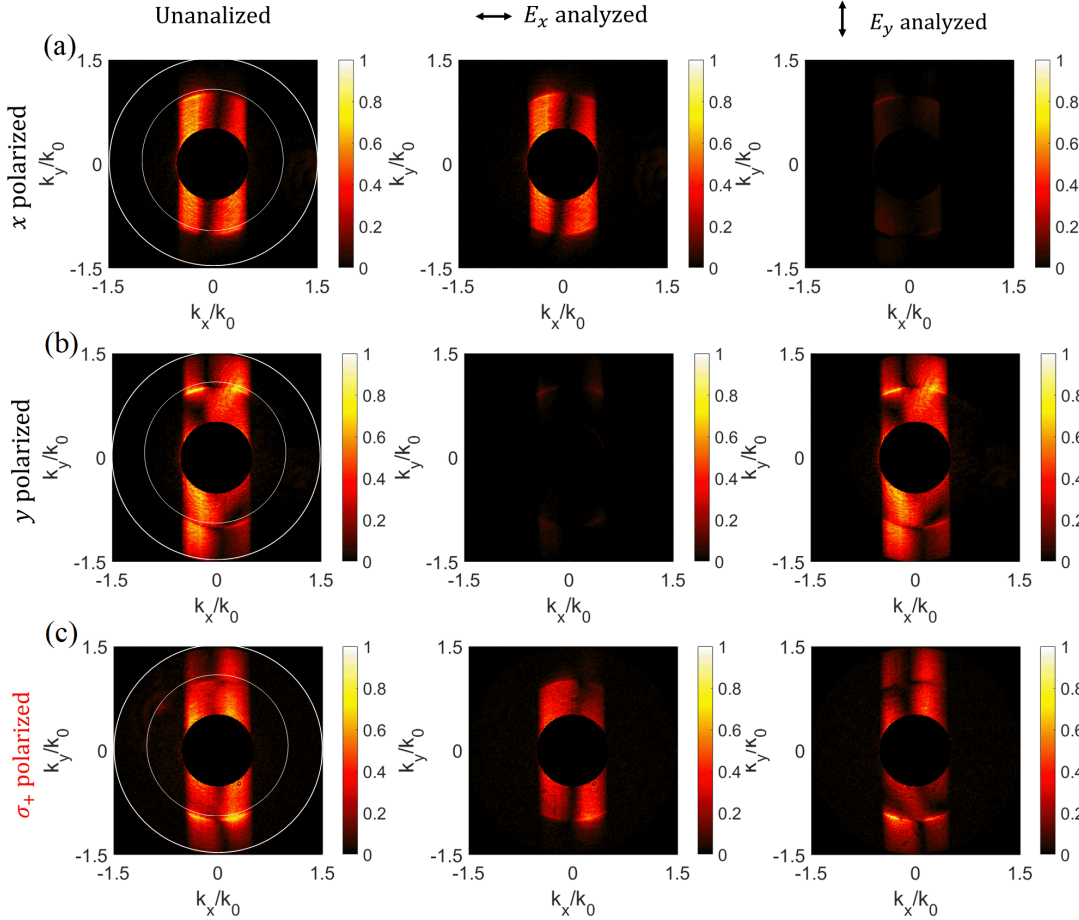
FIGURE 3.4: Polarization analysis of measured FP intensity distribution. (a)FP due to x polarized incident beam and polarization analysis along x and y respectively indicate almost all the scattered light is x polarized. (b) FP due to y polarized incident beam and analyzed along x and y respectively to indicate the light is predominantly y polarized. (c) FP due to incident σ_+ LG_0^1 beam and its polarization analysis along x and y direction respectively.

profile within the sub-critical region of the $k_y > 0$ part in the FP, for σ_+ and σ_- polarized LG_0^1 beam respectively. The preference of the scattering is opposite for σ_+ polarized case with respect to that of σ_- LG_0^1 beam data as indicated by the black arrows. The preference is the result of spin flow. Since the dominant contribution to the spin flow occurs due to the inner circular part of the beam as shown in fig. 3.2, the preference follows the same handedness. The super-critical region intensity distribution profile in the $k_y > 0$ half for both σ_+ and σ_- polarized LG_0^1 beam exhibit similar preference as shown in fig. 3.5 (e) and (f). This preference as well as the number of lobes indicates the OAM state of the incident beam [18].

FIGURE 3.5: Spin dependent FP intensity distribution for LG_0^1 beam and analysis of $k_y > 0$ region. FP intensity distribution for (a) σ_+ and (b) σ_- polarized LG_0^1 beam. The corresponding intensity distribution profile in the sub-critical region of the $k_y > 0$ part of the FP for σ_+ and σ_- polarized LG_0^1 beam is shown in (c) and (d) respectively. The same for super-critical region is shown in (e) and (f). The black arrows indicate the preference of distribution.

The quantification of the intensity distribution can be performed by calculating the directionality $D = (I_2 - I_1)/(I_2 + I_1)$, where I_i represents the integrated intensity of ith lobe for sub- or super-critical region. The experimentally measured directionality value from fig. 3.5 (c) and (d) we find, $D_{sub} = 0.094$ for σ_+ LG_0^1 beam and $D_{sub} = -0.123$ for σ_- LG_0^1 beam in the sub-critical region. Therefore, $D_{sub} > 0$ for σ_+ polarization case and $D_{sub} < 0$ for σ_- polarized beam, i.e., sign of the directionality in the sub-critical region inverts depending upon the spin flow direction and hence the SAM state. On the other hand, the preferential

scattering in the super-critical region of the FP indicates the sense of orbital flow and hence the OAM state: $D_{super} = -0.284$ for σ_+ polarized and $D_{super} = -0.563$ for σ_- polarized LG_0^1 beam, i.e., directionality sign ($D_{super} < 0$) remains the same. Hence, $D_{sub} > 0$ and $D_{super} < 0$ indicates σ_+ LG_0^1 beam excitation and $D_{sub} < 0$ and $D_{super} < 0$ indicates σ_- LG_0^1 beam excitation. Although, selective analysis of the FP intensity distribution allows differential sensing of the spin and orbital energy flow, the total transverse energy flow influences the effective directionality magnitude in the super-critical region to some extent. The measured directionality for the super-critical region is significantly lower for σ_+ LG_0^1 beam than for σ_- LG_0^1 beam, which is due to the higher total transverse energy flow density for σ_- polarized beam, as shown in fig. 3.2. For sub-critical region the change is much smaller due lower directionality value as well as positional sensitivity.

3.5.2 Inversion of the orbital flow sense

To further establish the detection mechanism, we investigate the FP intensity distribution by inverting the orbital flow sense, i.e., for LG_0^{-1} beam. Fig. 3.6 (a) and (b) shows the scattered

FIGURE 3.6: Spin dependent FP intensity distribution for LG_0^{-1} beam and analysis of $k_y > 0$ region. FP intensity distribution for (a) σ_+ and (b) σ_- polarized LG_0^{-1} beam. The corresponding intensity distribution profile in the sub-critical region of the $k_y > 0$ part of the FP for σ_+ and σ_- polarized LG_0^{-1} beam is shown in (c) and (d) respectively. The same for super-critical region is shown in (e) and (f). The black arrows indicate the preference of distribution.

FP intensity distribution for σ_+ polarized and σ_- polarized LG_0^{-1} beam. Fig. 3.6 (c) and (d) shows the corresponding intensity distribution profile in sub critical region of the the $k_y > 0$ half for the σ_+ and σ_- polarized case respectively. The directionality values turns out to be $D_{sub} = 0.054$ for σ_+ and $D_{sub} = -0.132$ for σ_- polarized LG_0^{-1} beam. The identical directionality sign as that of the σ_+ and σ_- polarized LG_0^1 beam (see fig. 3.5) indicates the same SAM sign. On the other hand, for the super-critical region intensity distribution, shown in fig. 3.6 (e) ($D_{super} = 0.369$) and (f) ($D_{super} = 0.114$), the sign of the directionality is opposite to that of the LG_0^1 case. This indicates the sign inversion of the topological charge and hence the orbital as well as total transverse energy flow of the beam. Therefore, the detection mechanism is robust with respect to the inversion of the orbital flow.

3.5.3 Detection of OAM and SAM for higher order LG beam

In order to investigate the detection mechanism for higher order LG beams, we investigate the scattered FP intensity distribution for LG_0^2 beam. Fig. 3.7(a) and (b) shows the FP intensity distribution for σ_+ and σ_- polarized LG_0^2 beam respectively. In this case, 3 lobes can be observed, instead of 2, like in the previous case, indicating the magnitude of the topological charge ($l + 1$ lobes for LG_0^l beam)[18]. The corresponding intensity distribution in the sub-critical region of the $k_y > 0$ half is shown in fig. 3.7 (c) and (d). The intensity
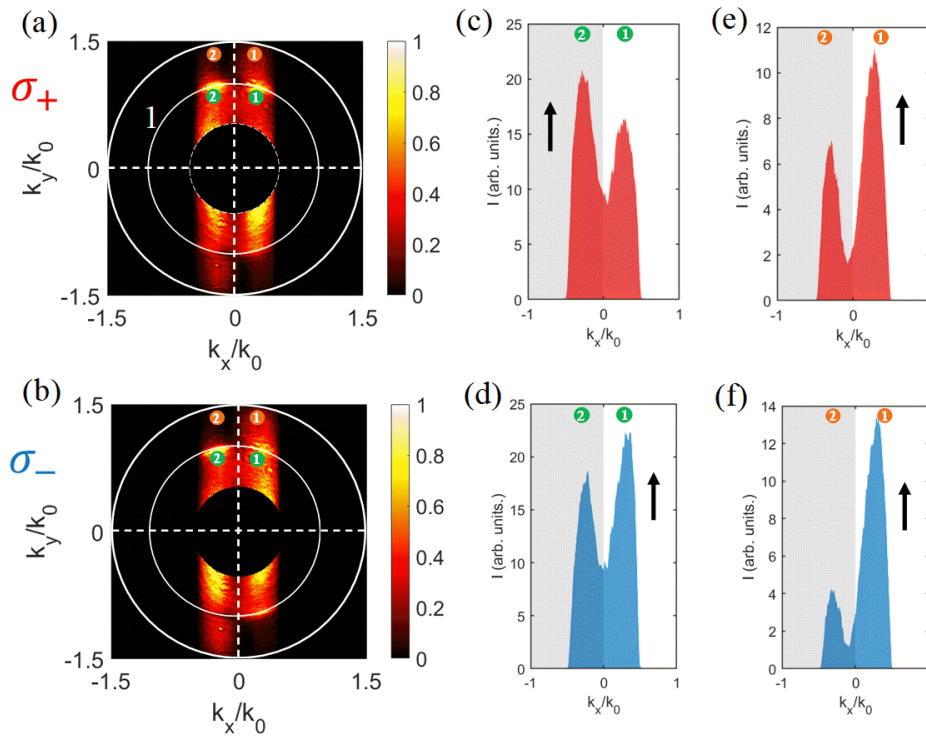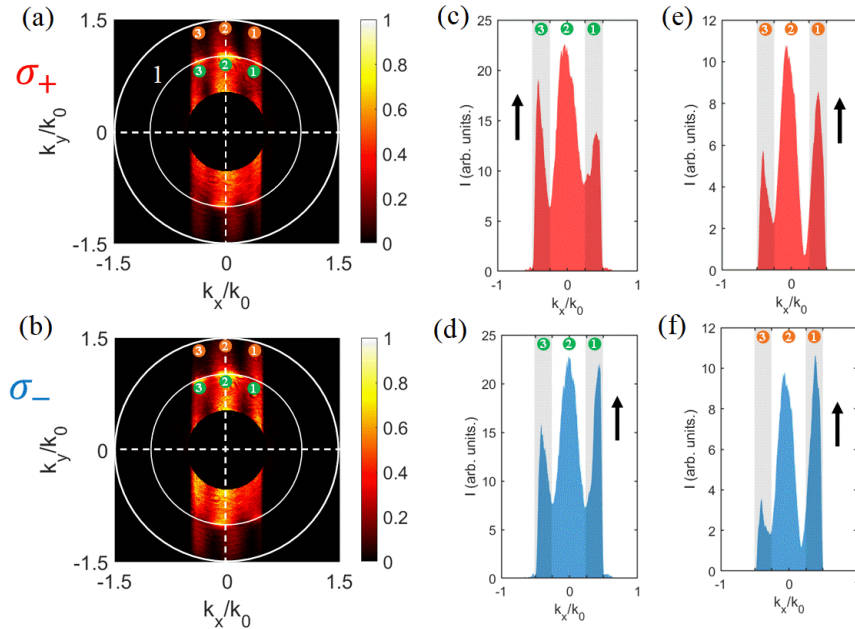

FIGURE 3.7: Spin dependent FP intensity distribution for LG_0^2 beam and analysis of $k_y > 0$ region. FP intensity distribution for (a) σ_+ and (b) σ_- polarized LG_0^2 beam. The corresponding intensity distribution profile in the sub-critical region of the $k_y > 0$ part of the FP for σ_+ and σ_- polarized LG_0^2 beam is shown in (c) and (d) respectively. The same for super-critical region is shown in (e) and (f). The black arrows indicate the preference of distribution.
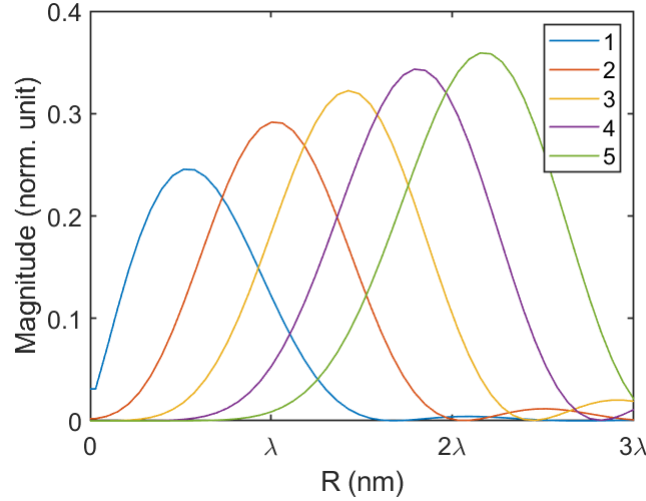
FIGURE 3.8: Incremental focal OFD ($\mathbf{p_o^\perp}$) of LG beams. Calculated normalized transverse flow density at the focal plane of 0.5 NA lens for x polarized LG_0^l beam from $l = 1\ 5$ exhibits incremental $\mathbf{p_o^\perp}$. The values are normalized with respect to maximum of Poynting vector magnitude.

distribution for the super-critical region for σ_+ and σ_- polarized case is shown in fig. 3.7 (e) and (f) respectively. From both fig. 3.7 (c) and (d) as well as fig. 3.7 (e) and (f) it can be seen that the central lobe remains of almost same intensity for σ_+ and σ_- polarized case, whereas the gray-shaded right-most (numbered 1) and left-most (numbered 3) lobes undergo intensity change. Thus we consider the integrated intensity of these two lobes only (1: NA 0.5 to 0.25 and 3: NA -0.25 to -0.5). The directionality values for the sub-critical region intensity distribution in fig. 3.7 (c) and (d) are $D_{sub} = 0.029$ and $D_{sub} = -0.157$ respectively. As before, the sign inversion of directionality allows us to accurately detect the SAM sign and the signs are same as in the case of LG_0^1 beam. On the other hand, the directionality for the super-critical region from fig. 3.7 (e) and (f), $D_{super} = -0.278$ for σ_+ polarized and $D_{super} = -0.555$ for σ_- polarized case, indicates the OAM sign.

It is worthwhile to notice that the directionality values we get in the sub-critical region for σ_+ polarized beam is lower for LG_0^2 beam than that of LG_0^1 beam. This is because, as the topological charge magnitude of LG beam increases, the magnitude of the orbital flow increases as shown in fig. 3.8. Therefore, it will have majority contribution in the total transverse energy flow, making its more difficult to distinguish the effect of the spin flow. Additionally, presence of $l + 1$ lobes for large l for LG_0^l beam scattering [18] in a small scattered width ($k_x = -0.5$ to 0.5) in the FP intensity distribution, will make it harder for us to detect the fluctuation in the polarization dependent magnitude of the lobes.

Hence, owing to the polarization and transverse energy flow dependent interaction of the AgNW with the incident beam, we are able to unambiguously detect OAM and SAM of the incident beam.
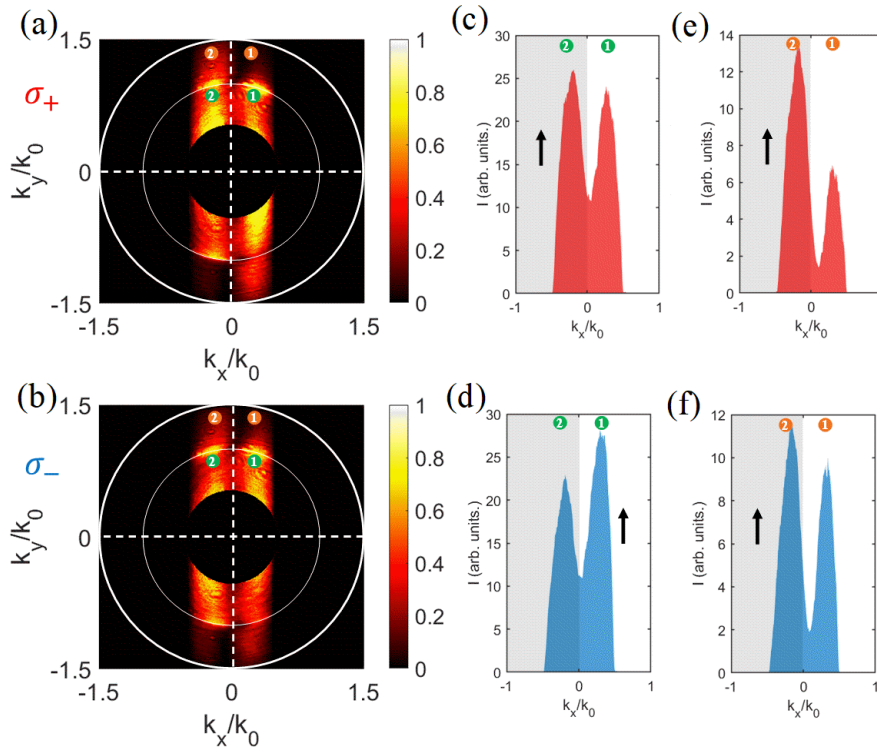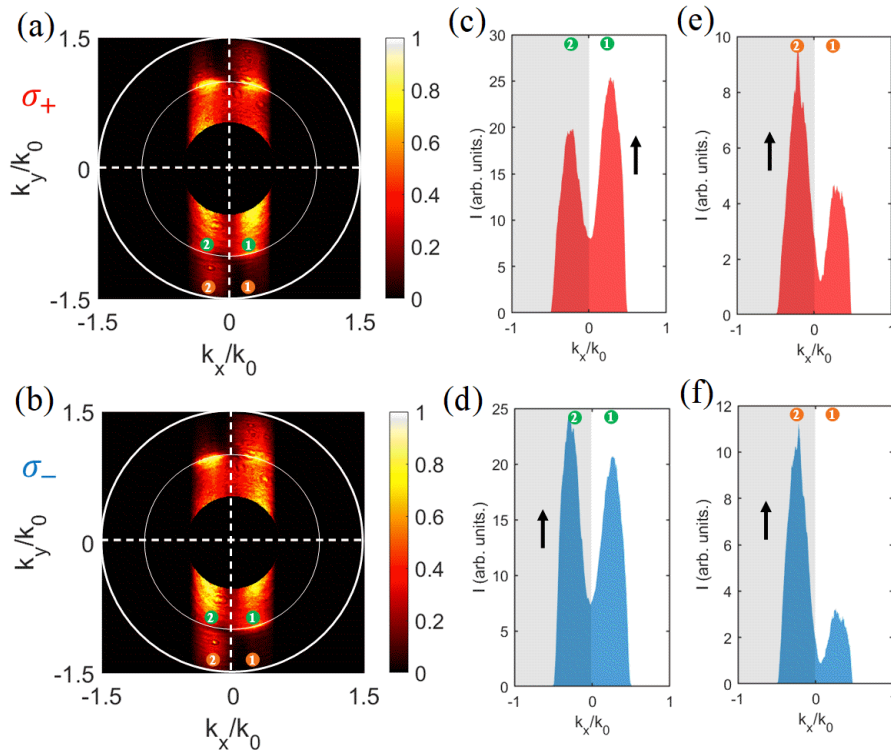
FIGURE 3.9: Spin dependent FP intensity distribution for LG_0^1 beam and analysis of $k_y < 0$ region. FP intensity distribution for (a) σ_+ and (b) σ_- polarized LG_0^1 beam. The corresponding intensity distribution profile in the sub-critical region of the $k_y < 0$ part of the FP for σ_+ and σ_- polarized LG_0^1 beam is shown in (c) and (d) respectively. The same for super-critical region is shown in (e) and (f). The black arrows indicate the preference of distribution.

We now look at three specific alteration of the detection mechanism and investigate their effect on the overall mechanism:

3.6 Alterations of the detection mechanism

3.6.1 Inversion of the detection region

While we have investigated the directionality for the $k_y > 0$ region of the FP intensity distribution, here we investigate the FP intensity distribution profile in $k_y < 0$ region for LG_0^1 beam. Fig. 3.9 (a) and (b) shows FP intensity distribution for σ_+ and σ_- polarized LG_0^1 beam respectively. The corresponding intensity distribution in the sub-critical region of $k_y < 0$ half for σ_+ and σ_- polarized beam is shown in fig. 3.9 (c) ($D_{sub} = 0.130$) and (d) ($D_{sub} = 0.0425$)respectively. The super-critical region intensity distribution for $k_y < 0$ half for σ_+ and σ_- polarized beam is shown in fig. 3.9 (e) ($D_{super} = 0.290$) and (f) ($D_{super} = 0.526$) respectively. The directionality values are exactly opposite in the sign
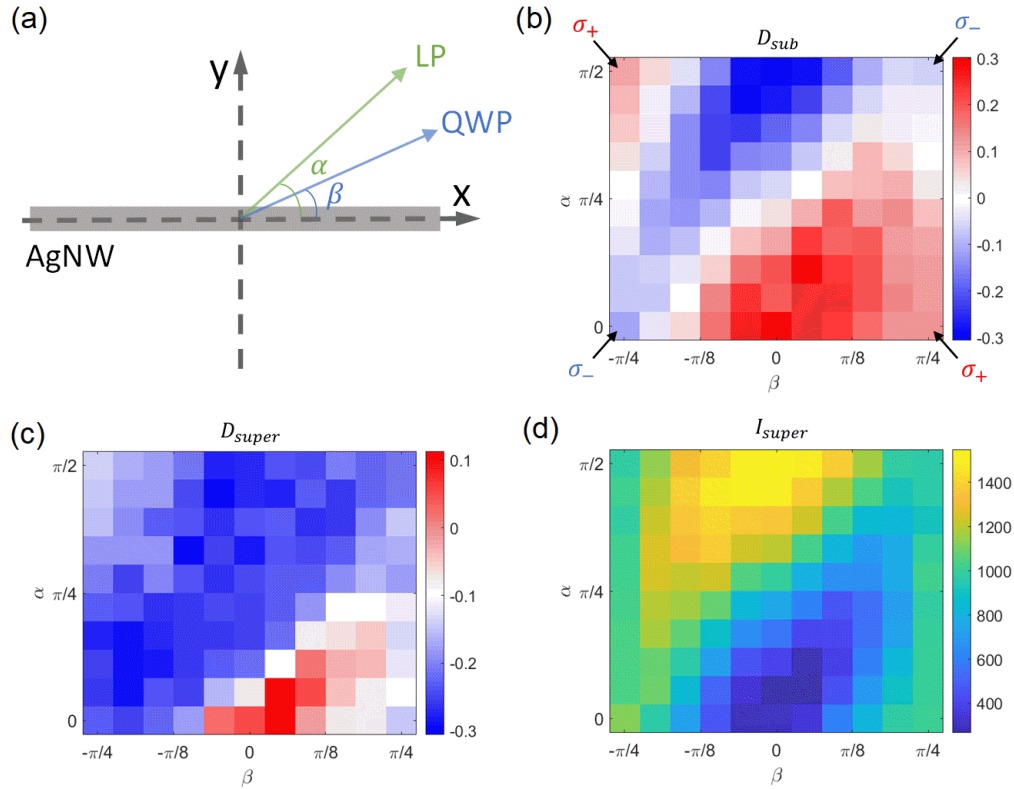
FIGURE 3.10: Polarization dependent directionality for LG_0^1 beam. (a) The linear polarization (LP) angle (α) and quarter-wave plate (QWP) angle (β) is defined with respect to nanowire long axis. Measured directionality in the (b) sub-critical region (c) super-critical region of the FP. (c) Integrated intensity in the super-critical region. The σ_+ and σ_- states used in our experiments are indicated by black arrows and show inversion of D_{sub} sign for σ_+ and σ_- states, whereas the sign of D_{super} remains the same, effectively reading out the SAM and OAM states.

compared to the $k_y > 0$ half as shown in fig. 3.5, as the intensity pattern for $k_y > 0$ region is anti-symmetric with respect to $k_y < 0$ region.

3.6.2 Elliptical polarization dependence on directionality

We have investigated the polarization dependence of the directionality in the sub- (D_{sub}) and super-critical (D_{super}) region of $k_y > 0$ region of the FP by changing the incident polarization through a half-wave plate (HWP) followed by a quarter-wave plate (QWP). In addition, we have also investigated the elliptical polarization dependence of the intensity in the super-critical region (I_{super}) of $k_y > 0$ part of the FP. The linear polarization angle (LP) due to the HWP is represented as α and QWP angle is represented by β, and are measured with respect to nanowire long axis (x axis) as shown in figure 3.10 (a).

Simultaneous measurement of spin and orbital angular momentum states are possible due to the reference set by the orbital energy flow, the readout of which is performed by

measurement of the directionality in the super critical region of the FP. The SAM states can then be measured by comparing the directionality in the sub-critical region of the FP, which is dominantly due to the contribution of spin energy flow of circularly polarized beams. For elliptically polarized beams, no such reference can be established based on just the directionality measurements as the directionality magnitudes in both the sub- and super-critical region depends on the polarization states as well as transverse energy flow. However, with the data presented in figure 3.10 (b)−(d) for D_{sub}, D_{super} and I_{super} respectively, the following observations can be made:

1. The LCP (σ_+) and RCP (σ_-) state used in our experiments, indicated by black arrows in figure 3.10 (a), show inversion of D_{sub} values from σ_+ to σ_- case, whereas D_{super} remains the same, effectively reading out SAM and OAM states. The determination is performed by comparing the sign of directionality in the sub- and super-critical region.

2. To determine linear polarization states, the magnitude of the directionality also has to be considered in addition to its sign. For example, if $D_{sub} \approx -0.3$ and $D_{super} < 0$, the state can be either determined as y polarized LG_0^1 beam ($\alpha = pi/2$, $\beta = 0$), or conversely, it can be x polarized LG_0^{-1} beam. To further distinguish between these two cases, the integrated intensity in the super-critical region (I_{super}) of the $k_y > 0$ region has to be considered. A low I_{super} indicates x polarized beam and high I_{super} indicates y polarized beam. Thus, this distinction can be made by considering the parameters: D_{sub}, D_{super} and I_{super}.

3. For other cases, it is not possible to determine and reconstruct the elliptical polarization states accurately by considering the above parameters (D_{sub}, D_{super} and I_{super}).

However, by studying elliptical polarization dependence of D_{sub}, D_{super} and I_{super}, the elliptical polarization states can be reconstructed if either α or β is known. The accuracy of the elliptical polarization measurement in such cases will be subject to standardization of the directionality values, which can vary depending on the NW width and incident beam profile. Repetition of such measurements on different nanowire, or different region of a single nanowire may result in determination of error bar on D.

3.6.3 Directionality dependence on AgNW dimension

The accuracy of the simultaneous detection of the SAM and OAM state depends upon the width of the nanowire used for the scattering process. We have performed the experiments for AgNWs having width ≈ 200 nm.
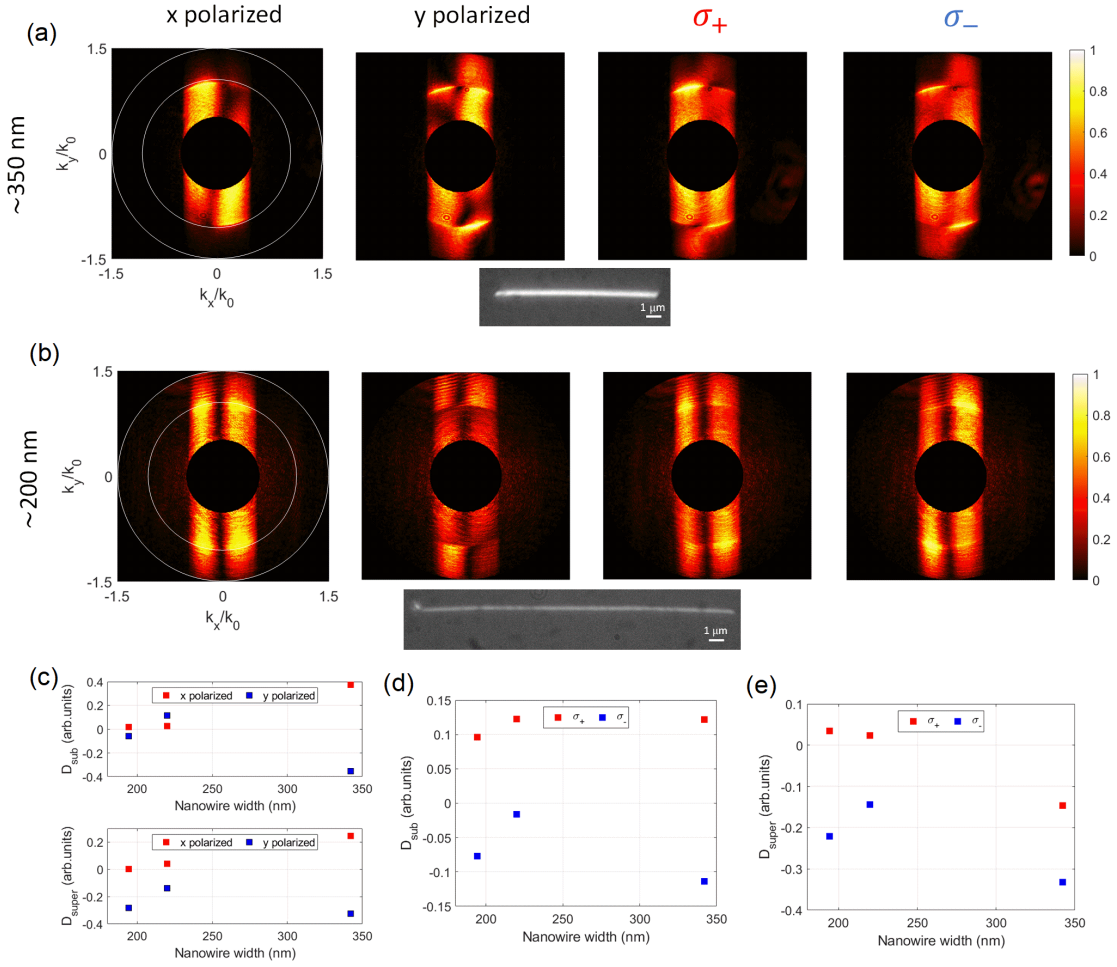
FIGURE 3.11: Dependence of FP intensity distribution on width of AgNW. FP intensity distribution for x, y, σ_+ and σ_- polarized LG_0^1 beam for (a) ≈ 350 nm and (b) ≈ 200 nm. Nanowire micrographs are shown below the corresponding row. (c) Directionality values in the sub- (D_sub) and super-critical region (D_{super}) for $k_y > 0$ region of FP for x and y polarized LG_0^1 beam, (d) D_{sub} for σ_+ and σ_- polarized LG_0^1 beam. (e) D_{super} for $k_y > 0$ part of FP for σ_+ and σ_- polarized LG_0^1 beam.

Comparison of fig. 3.11 (a) and (b) allows us to distinguish the sattering pattern due to different width of the nanowire. For x polarized LG_0^1 beam, scattering from ≈ 200 nm NW leads to significant signal in the super-critical region compared to ≈ 350 nm NW. It leads to different directionality values in the sub- and super-critical region in the FP for ≈ 200 wire from that of the ≈ 350 nm case, as shown in figure 3.11 (c)-(e). For the thinner nanowires, both the magnitudes of D_{sub} and D_{super} for x and y polarized incident beam is small compared to the ≈ 350 nm wire, rendering measurement of OAM mode with ≈ 350 nm more accurate. For σ_+ or σ_- polarized LG_0^1 beam, both ≈ 200 nm and ≈ 350 nm wires detect the polarization state through the inversion of the D_{sub} sign, although with relatively lesser magnitude for thinner nanowire. But, for thinner nanowires D_{super} may take opposite

sign for σ_+ LG$_0^1$ beam, resulting incorrect reading out of the OAM mode. This can be attributed to the fact that for ≈ 200 nm wires, there is significant signal in the super-critical region of FP for x polarized beam.

3.7 Conclusion

In summary, we present an experimental study of forwards scattering assisted simultaneous and unambiguous detection of spin and orbital angular momentum of light by employing Fourier plane microscopy.

We have analyzed the intensity distribution due to scattering from left and right circularly polarized LG beams from an AgNW, in the sub- and super-critical region in the Fourier plane. It leads to the conclusion that preference of scattering in the sub-critical region changes when the spin is inverted, whereas the super-critical region intensity distribution preference depends predominantly on the orbital energy flow of the incident beam. The detection mechanism have been explored through investigation of the incident linear polarization dependant scattering pattern from the AgNW, in the sub-critical region or both sub- and super-critical region in the FP. The effective directionality trends have been further investigated through calculation of focal optical field and corresponding transverse energy flow constituent due to spin and orbital angular momentum of the light beam.

Therefore, the work presented in the chapter emphasizes spin-orbit interaction based on simple single element chipscale detection configuration with prominent spin and orbital angular momentum detection capability. The detection scheme exhibits significant improvement over interferometric based approaches [86–88] and diffraction based approaches [89–92] owing to the robustness of the detection mechanism. On the other hand, the single scatterer-based approach represents simplicity over the complex nanofabrication requirement of metasurface and nanoantenna approaches [96–98]. However, where this approach lacks are the ability to detection to many higher order LG modes, as compared to approach of dielectric metasurface approach discussed in [98]. Nonetheless, with more rigorous polarization dependent directionality study, it can potentially act as a polarization detector. Additionally, the spin-orbit interaction dependent scattering may lead to opportunities in harnessing the resulting optical forces for optical manipulation at nano scale as well as furthering our understanding of spin-orbit interaction.

Chapter 4

Experimental observation of optical spin-Hall effect and detection of longitudinal spin density of focused-linearly-polarized light

Abstract:

This chapter discusses the generation of longitudinal spin due to focusing of linearly polarized Gaussian and HG_{10} beam and consequent spin-Hall effect of upon scattering from a single silver nanowire (AgNW). Specifically, we report generation spin-dependent antisymmetric Fourier plane (FP) intensity distribution upon circular polarization analysis of the scattered light. The corresponding far-field longitudinal spin density (s_3) is significantly enhanced for HG_{10} beam compared to the Gaussian beam. The studies are corroborated with focal optical field calculations and finite element method numerical calculations. The content of this chapter is adapted from the research article "Physical Review A, 103, 013520 (2021), (arXiv:2008.12245)" [13].

4.1 Introduction and motivation

In recent times, the spin and orbital angular momentum of light has been extensively harnessed in the context of spin-orbit interaction (SOI) as well as orbit-orbit interaction [14, 59, 60]. Among different examples, optical spin-Hall effect is one of the unique examples, where, equivalent to its electronic counterpart [63, 64], a transverse shift in the scattered beam location is perceived due to the transverse energy flow of the impinging light beam on a dielectric interface [9–11] or a scatterer [12, 104]. In addition, opposite spins of the impinging beam leads to opposite transverse shifts.

The discussed SOI effects are weak for paraxial beams. Hence, for a beam having no transverse energy flow results no net transverse shift. Focusing of a paraxial light beam

39
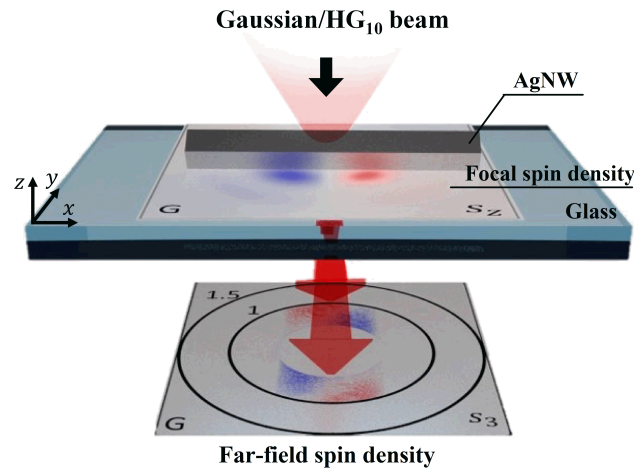
FIGURE 4.1: Schematic of the measurement scheme of optical spin-Hall effect. An AgNW placed at the focal plane scatters the generated focal longitudinal spin density (s_z), and the signal is detected at the Fourier plane as far-field longitudinal spin distribution (s_3).

and consequent non-paraxial optical fields can lead to generation higher angular momentum [105, 106], leading to enhanced SOI effects [17, 107]. Along with this, the optical fields due to strong focusing have been harnessed for studies in optical trapping [5–7], sub-wavelength position sensing [108, 109] as well as angular momentum interconversion [19, 110]. The interaction of focal optical fields with matter can lead to additional SOI mediated photonic applications such as directional scattering and nano probing [15–17, 111].

These studies motivated us to investigate generation and detection of longitudinal spin density through scattering of focused linearly polarized Gaussian and HG_{10} beam from a quasi one dimensional scatterer, namely a monocrystalline silver nanowire (AgNW) placed on a glass substrate, as shown in fig. 4.1. Polarization analysis of the forward scattered light in the Fourier plane (FP) reveals anti-symmetric distribution of intensity for opposite circular polarization states, with respect to long axis of the AgNW. The pattern inverts for left circular polarization (LCP) analyzed case with respect to that of right circular polarization (RCP) analyzed one, indicating existence of intrinsic spin-Hall effect. The difference between the two FP intensity distributions quantify the spin-Hall signal as well as far-field longitudinal spin density (s_3). Furthermore, the comparison of s_3 for Gaussian beam with respect to that of HG_{10} beam reveals higher spin-Hall signal for HG_{10} beam. All the results have been examined through calculation of focal optical fields and corroborated through numerical simulations.

In the following sections, we examine theoretically calculated optical focal field and show the existence of longitudinally spinning fields at focal plane.

4.2 Calculation of focal optical fields

Focusing of paraxial optical beams through an objective lens leads to complex distribution of optical fields at the focal plane. The complex distribution of optical fields at the focus of an objective lens can be calculated by employing Debye-Wolf integral formulation [78, 83], as described in section 2.2.1 of chapter 2.

4.2.1 Focal electric field intensity distribution

Employing equation 2.2 we calculate the electric field components, $\mathbf{E} = (E_x, E_y, E_z)$ at the focal plane of a 0.5 NA lens for linearly polarized (x polarized) paraxial Gaussian(G) and Hermite-Gaussian (HG) beam (HG_{10}) at wavelength $\lambda = 633$ nm, propagating along z axis. Fig. 4.2 (a) shows the intensity distribution corresponding to E_x component ($I_x = \varepsilon_0 |E_x|^2$) of the focal optical field for Gaussian(G) and HG_{10} (HG) beams. Similarly, the intensity distribution for the E_y component ($I_y = \varepsilon_0 |E_y|^2$) of the field is shown in fig. 4.2 (b). The intensity distribution values are normalized with respect to maximum value of total intensity, $I = \varepsilon_0 |E|^2$. The paraxial polarization profile of the beams are given in 4.2 (a) insets. Although the intensity distribution I_y of Gaussian beam differ from that of HG_{10} beam, it can be observed in fig. 4.2 (b) that, the maximum magnitude for HG_{10} beam is significantly higher than that of Gaussian beam. The ratio of maximum value of I_y of HG_{10} beam to that of Gaussian beam turns out to be ≈ 2.97.

4.2.2 Focal spin density distribution

One of the unique feature that emerge due to focusing of optical field is complex distribution of energy flows. Specifically, the rich feature of polarized optical fields lead to generation of transverse energy flow associated with spin angular momentum as described by equation 1.2 in chapter 1. This can be further quantified by spin density, given by [112],

$$\mathbf{s} \propto \mathrm{Im}\left[\varepsilon_0(\mathbf{E}^* \times \mathbf{E}) + \mu_0(\mathbf{H}^* \times \mathbf{H})\right]. \tag{4.1}$$

The symmetric nature of equation (4.1) allows us to consider the contribution of either the electric field ($\mathbf{E}$) part or the magnetic field ($\mathbf{H}$) part. Considering the fact that a plasmonic scatterer responds more to incident electric field component, we take into account that part. The spin density components given by equation (4.1) can either by longitudinal or transverse with respect to the propagation axis (z axis) [113]. The longitudinal component of the spin density is given by,

$$s_z \propto 2\,\mathrm{Im}[E_x E_y^*] \propto s_3. \tag{4.2}$$

In the far-field it can be quantified through measurement of the fourth Stokes parameter s_3, which determines the degree of circular polarization of a planar optical field [48].

Fig. 4.2 (c) shows the calculated focal plane (xy plane) s_z distribution for focusing of x polarized Gaussian and HG_{10} beams. The values have been normalized with respect to maximum of I. To get a more quantitative measure, we compute distribution of spin density (S_z) of one half of the focal plane, i.e. by integrating over the one of the spatial coordinates $y = 0$ to 3λ, i.e., $S_z(x) = \int_{y=0}^{3\lambda} s_z(x, y)\, dy$. Comparison of s_z for Gaussian and HG_{10} beams, shown in fig. 4.2 (c), it can observed that s_z is higher for HG_{10} beam compared to that of Gaussian beam. The same is reflected in fig. 4.2 (d), which shows the comparative magnitude of S_z for x polarized Gaussian and HG_{10} beams as a function of x coordinates at the focal plane. We can therefore, assign a corresponding enhancement factor by taking ratio of extremum magnitudes of S_z, which in this case turns out to be $\eta_{theory} = 1.29$.

In the following sections we discuss the detection mechanism employed for measuring the longitudinal spin density and consequent generation of optical spin-Hall effect.
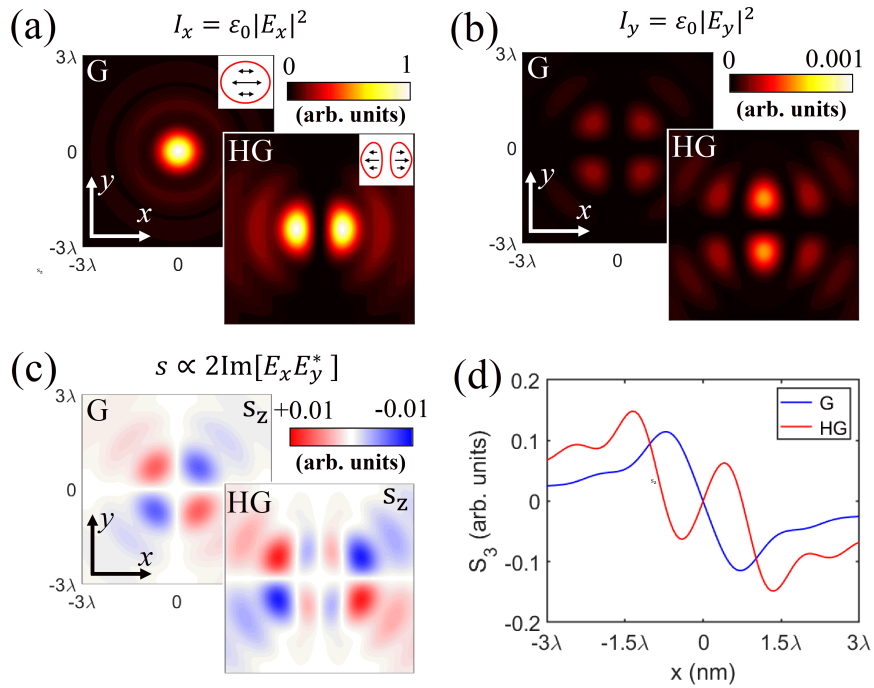
FIGURE 4.2: Calculation of focal optical fields. Calculated focal intensity profiles corresponding to (a) x polarized field component, (b) y polarized field component of the total optical field for Gaussian and HG_{10} beams. Insets in (a) shows the x polarized paraxial beam profiles. (c) Longitudinal spin density (s_z) at the focus for Gaussian and HG_{10} beams. (d) Comparative plot of longitudinal spin density distribution (S_z) for Gaussian and HG_{10} beam.

4.3 Detection mechanism of scattered spin density

4.3.1 Experimental configuration for forward scattering

The experimental implementation of detection of longitudinal spin density and consequent observation of optical spin-Hall effect relies on elastic scattering of focal optical fields. We employ a monocrystalline silver nanowire (AgNW) having pentagonal cross-section with width ≈ 350 nm and width $\approx 5\,\mu$m. These nanowires are chemically synthesized [99], and were drop-casted onto a glass substrate. Fig. 4.3 (a) shows an bright field optical image of the AgNW used for our experiments. Fig. 4.3 (b) shows scanning electron micrograph of a nanowire section.

A nanowire section is illuminated Gaussian and HG_{10} beam, prepared by projecting Gaussian beam onto a spatial light modulator with blazed hologram, at wavelength $\lambda = 632.8$ nm. The experimental configuration is similar to our previous study [12] and the setup has been elaborated in section 2.1.3 of chapter 2. The schematic of forward scattering setup is depicted in fig. 4.3 (c). The paraxial (Gaussian/HG_{10}) beam having polarization along the long axis of the nanowire (x axis) is focused onto the center of the AgNW placed at ($x = 0$, $y = 0$), with a $50\times$ 0.5 NA objective lens and the forward scattered light is collected using an $100\times$ 1.49 NA oil immersion objective lens. The collected signal is analysed using a combination of analyzer and quarter-wave plate and the Fourier plane is projected onto a CCD using relay optics as depicted in sections 2.1.2 and 2.1.3 of chapter 2. The use of low NA (0.5 NA) excitation and high NA (1.49 NA) collection objective lens facilitates the collection of scattered light in higher angles in the FP. The un-scattered
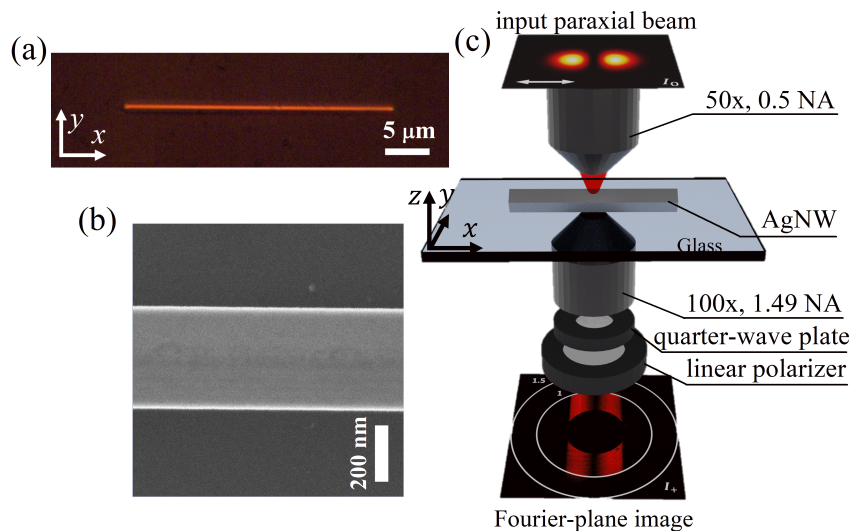
FIGURE 4.3: Experimental configuration. (a) Optical bright-field image of the AgNW used for our experiments. (b) FESEM image of an AgNW section. (c) The schematic of experimental setup for the elastic forward scattering and its polarization analysis.

44

Chapter 4. Experimental observation of optical spin-Hall effect and detection of longitudinal spin density of focused-linearly-polarized light

light, which dominates the incident NA part of the FP intensity distribution, is omitted for analysis.

4.3.2 Nanowire as a scatterer

An AgNW placed at the focal plane of an objective lens mimics the effect of a nanoscopic strip diffraction [92, 114]. It is possible to obtain the scattering pattern by employing scalar diffraction theory and Babinet's principle, in case of strip diffraction. However, the complex and vectorial distribution of the optical field as well as the unconventional pentagonal geometry of the nanowire cross-section renders the use of full scattering theory essential in this case [115].

As explained in the previous chapter, the scattered optical field from the AgNW can be collected in two distinct regions in the far-field, i.e., sub-critical or allowed region (NA < 1) and super-critical or forbidden region (NA > 1) in FP. The longitudinally polarized field (x polarized) with respect to the nanowire long axis (x axis) components gets scattered in the sub-critical region, as shown in fig. 4.4 (a) and (c) for Gaussian and HG beams respectively. The transversely polarized field (y polarized) lead to near-field accumulation at the nanowire edges and hence, contribute to signal in both sub- and super-critical region [55, 56]. The
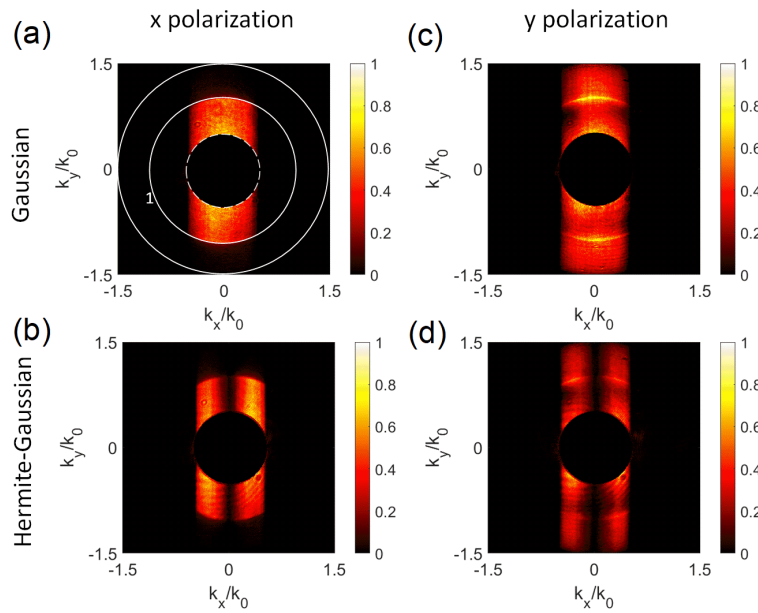
FIGURE 4.4: Polarization dependence of scattering pattern. Measured far-field intensity pattern for x polarized (a) Gaussian and (b) HG beams respectively for a nanowire oriented along x axis. Measured far-field intensity pattern for y polarized (c) Gaussian and (d) HG beams respectively. The inner and outer white circle in (a) represents critical angle for air-glass interface and collection limit of the objective lens. Dashed black disk and white circle represent the incident NA region.

evanescent NF gets partially converted into propagating waves at the air-glass interface and can be observed in the super-critical region of the far-field [4], as shown in fig. 4.4 (b) and (d) for Gaussian ang HG beams respectively. Hence, elastic scattering from an AgNW allows us to route a portion of the scattered light either in the sub-critical region or both sub- and super-critical region by engineering the incident linear polarization state as longitudinal or transverse to the wire. Therefore, to extract the optical field information through scattering without it being modified due to evanescent wave components, we operate with incident longitudinally polarized fields and analyze the sub-critical region of the resultant FP intensity distribution.

4.4   Detection of longitudinal spin density and spin-Hall effect

4.4.1   Experimentally measured scattering intensity

First, we examine the elastic scattering of optical fields due to focusing of longitudinally polarized Gaussian and HG_{10} beams from an AgNW. Fig. 4.5 (a) and (b) shows the experimentally measured FP intensity distribution of forward scattered Gaussian and HG_{10} beams (I) and corresponding left circular polarization (LCP, I_+) and right circular polarization (RCP, I_-) analyzed distributions. The inner and outer white circles in fig. 4.5 (a) indicate the critical angle at air-glass interface and collection limit of the objective lens respectively. The incident NA is blocked and is shown by a black disk at the center. Absence of light in the super-critical region (NA $= k_x/k_0 = k_y/k_0 > 1$) in the measured FP intensity distribution indicates the minimal accumulation of NF at the NW edges.

Comparison of the FP intensity distribution shown in fig. 4.5 (a) and (b) indicates that for Gaussian beam the distribution has only one lobe, where as, presence of nodal line in the intensity profile of HG_{10} beam leads to presence of two intensity lobes. But, both the intensity patterns corresponding to I in fig. 4.5 (a) and (b) exhibit symmetric pattern with respect to k_x/k_0 axis (parallel to AgNW long axis). In contrast, the FP intensity distribution corresponding to I_+ and I_- of Gaussian beam exhibit shift along $k_x/k_0 < 0$ and $k_x/k_0 > 0$ (for $k_y/k_0 > 0$ region) respectively, revealing anti-symmetric scattering pattern, as depicted by the white arrows in fig. 4.5 (a). On the other hand, the analyzed I_+ and I_- components for HG_{10} beam exhibit shift along $k_y/k_0 < 0$ and $k_y/k_0 > 0$ direction for $k_x/k_0 > 0$ region respectively (and vice versa for $k_x/k_0 < 0$ region), as depicted by the white arrows in fig. 4.5 (b). The anti-symmetric distribution of the circular polarization analyzed FP intensity distribution indicates the presence of partial circular polarization in the optical fields [116]. This spin dependent opposite angular shift of the lobe(s) in the FP is analogous to optical

46

Chapter 4. Experimental observation of optical spin-Hall effect and detection of longitudinal spin density of focused-linearly-polarized light

spin-Hall effect of light [9, 12]. Therefore, the presence of longitudinal spin and the magnitude of the spin-Hall effect can be obtained by calculation of the far-field longitudinal spin density (s_3) as, $s_3 \propto I_+ - I_-$. Fig. 4.5 (c) and (d) shows the experimentally measured far-field longitudinal spin density for Gaussian and HG_{10} beams respectively. Experimentally measured intensity values are normalized with respect to the maximum value of I.

4.4.2 Numerically simulated scattering intensity

The experimental results are corroborated by full wave 3-dimensional finite element method (FEM) simulation. Details of the calculations have been elaborated in section 2.2.2 of chapter 2. We further extract the far-field scattering pattern by employing reciprocity arguments [84].
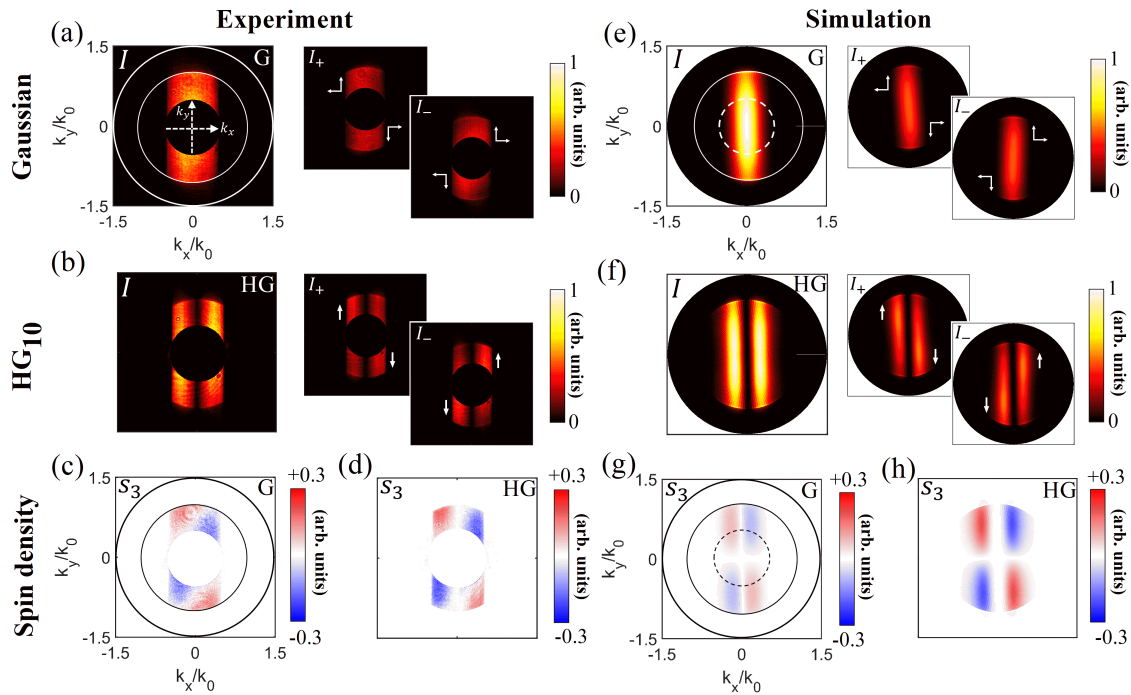
FIGURE 4.5: Far field intensity distribution and its analysis. Experimentally measured FP intensity distribution for (a) Gaussian, (b) HG_{10} beam. I represents total intensity, I_+ and I_- represents LCP and RCP analyzed FP intensity distribution respectively. Inner and outer circles in (a) represent the critical angle at air-glass interface and the collection limit of the objective lens NA respectively. The bias of the scattered field for I_+ and I_- is shown by white arrows. Incident NA region is omitted for analysis and shown by a black disk. Measured far-field longitudinal spin density (s_3) distributions are shown in (c) Gaussian and (d) HG_{10} beam. Numerically simulated FP intensity distributions of I, I_+, I_- for Gaussian and HG_{10} beams are given in (e) and (f) respectively. (g) and (h) show numerically calculated s_3 for Gaussian and HG_{10} beams respectively. The inner dashed white circle in (e) and dashed white circle in (g) represent the incident NA region equivalent to experimental counterpart.

Fig. 4.5 (e) and (f) shows the numerically calculated FP intensity distribution for Gaussian and HG_{10} beams and the corresponding LCP (I_+) and RCP (I_-) analyzed components. Similar to the experimentally measured data as shown in fig. 4.5 (a), the I_+ and I_- component shown in fig. 4.5 (e) exhibit opposite shift of the intensity lobe along k_x/k_0 axis, as indicated by the white arrows. The numerically simulated FP intensity distribution corresponding to I_+ and I_- of HG_{10} beam in fig. 4.5 (f), similar to its experimental counterpart in fig. 4.5 (b), exhibit shift along $k_y/k_0 < 0$ and $k_y/k_0 > 0$ direction for $k_x/k_0 > 0$ region respectively (and vice versa for $k_x/k_0 < 0$ region), indicated by the white arrows. The opposite shifts for I_+ and I_- components are analogous to angular spin-Hall shift. The anti-symmetric distribution corresponding to I_+ and I_- component indicate presence of longitudinal spin density and angular spin-Hall effect. The corresponding far-field longitudinal spin density (s_3) is obtained as $s_3 \propto I_+ - I_-$. Numerically simulated s_3 for Gaussian and HG_{10} beams are given in fig. 4.5 (g) and (h) respectively. The intensity values are normalized with respect to the maximum value of I. The simulated FP intensity patterns are in good agreement with their experimental counterparts.

4.5   Characterisation of optical spin-Hall effect

4.5.1   Enhancement of spin-Hall effect and longitudinal spin density

The characterization of the generated longitudinal spin density and the spin-Hall signal is further quantified by comparison of the s_3 for Gaussian and HG_{10} beams. Since the wire is centered at ($x = 0$, $y = 0$) with its long axis is aligned along x axis and the scattering is prominent in k_y/k_0 direction, we consider the $s_3(\kappa_x, \kappa_y)$ distribution along κ_x, where $\kappa_x = k_x/k_0$ and $\kappa_y = k_y/k_0$. In addition, symmetric nature of the intensity distribution allows us to consider either upper or lower half of the FP. We consider the upper half only, i.e., $\kappa_y \geq 0$ half, up to the critical angle. Therefore, we can compute distribution of far-field longitudinal spin density (S_3) as, $S_3(\kappa_x) = \int_{\kappa_y=0}^{1} s_3(\kappa_x, \kappa_y) \, d\kappa_y$.

Fig. 4.6 (a) and (b) shows distribution of $S_3(\kappa_x)$ for Gaussian and HG_{10} beam for both experimentally measured and numerically calculated far-field longitudinal spin density distribution. Both fig. 4.6 (a) and (b) higher longitudinal spin density values and hence higher spin-Hall signal for HG_{10} beam compared to Gaussian beam. The enhancement can be quantified by computing the enhancement factor by taking the ratio of extremum values of $S_3(\kappa_x)$ of HG_{10} to that of Gaussian beam. The computed enhancement factor from fig. 4.6 (a) is $\eta_{exp} = 1.31$, and from fig. 4.6 (b) it is $\eta_{sim} = 2.39$. Since focal $s_z \propto s_3$, the enhancement can be attributed to higher s_z of HG_{10} beam with respect to that of Gaussian beam (From fig. 4.2 (c) and (d): $\eta_{theory} = 1.29$). The difference between the measured s_3

48

Chapter 4. Experimental observation of optical spin-Hall effect and detection of longitudinal spin density of focused-linearly-polarized light
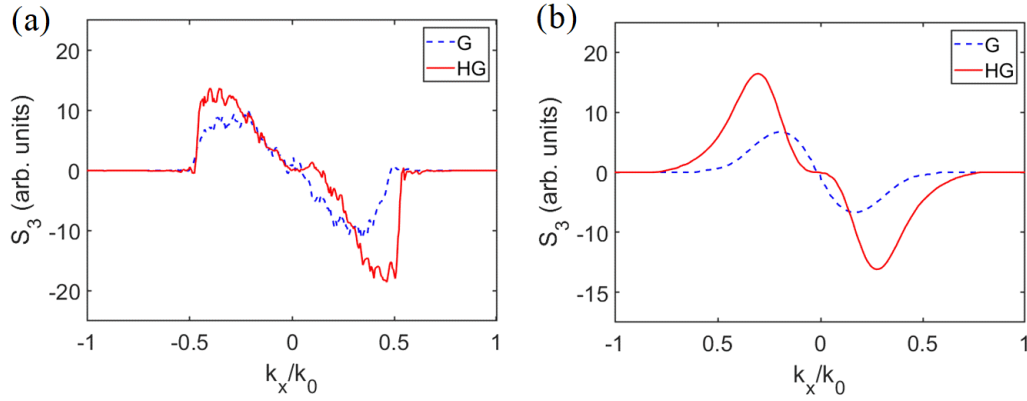
FIGURE 4.6: Comparison of far-field longitudinal spin density distribution ($S_3(\kappa_x)$). Comparative plot of $S_3(\kappa_x)$ for Gaussian and HG_{10} beam extracted from (a) experimentally measured and (b) numerically calculated FP intensity distributions.

enhancement values η_{exp} and η_{sim} can be attributed to omission of incident NA region in the experimental data as well as subtle difference of focusing in the numerical simulations with the experimental focusing conditions.

4.5.2 Wave-vector shift in the Fourier plane

The FP image of total intensity (I) for Gaussian and HG_{10} beam exhibit symmetrical characteristic about k_x/k_0 axis, in contrast to anti-symmetrical distribution of I_+ and I_-. To probe the shift of the intensity lobe(s) of $I_+(I_-)$, we plot the distribution $I_{+(-)}^{tot}(\kappa_x) = \int_{\kappa_y=0}^{1} I_{+(-)}(\kappa_x, \kappa_y)d\kappa_y$ and compare it with the distribution $I^{tot}(\kappa_x) = \int_{\kappa_y=0}^{1} I(\kappa_x, \kappa_y)d\kappa_y$ for Gaussian and HG_{10} beam in fig. 4.7.

Fig. 4.7 (a) and (b) shows indicates the wave vector shift along κ_x for Gaussian beam for experimentally measured and numerically calculated FP intensity distribution. In both the figures it can be seen that the $I_+^{tot}(\kappa_x)$ and $I_-^{tot}(\kappa_x)$ analysed distributions exhibit angular shift along $\kappa_x < 0$ and $\kappa_x > 0$ direction respectively. The measured shift from the experimental data in fig. 4.7 (a) is $\delta\kappa_{x,\text{expt}}^G = 0.34$, where as from the numerically simulated data the shift measured in fig. 4.7 (b) is $\delta\kappa_{x,\text{sim}}^G = 0.05$. On the other hand, for HG_{10} beam, the shift along κ_x, obtained from experimental data in fig. 4.7 (c) is $\delta\kappa_{x,\text{expt}}^{HG} = 0.01$ and that obtained from numerically simulated data in Fig. 4.7 (d) is $\delta\kappa_{x,\text{sim}}^{HG} = 0.01$. Therefore the shift along κ_x for HG_{10} beam is negligible compared to Gaussian beam. For HG_{10} beam, the shift is more along κ_y as can be determined from examining the FP intensity distribution corresponding to I_+ and I_- in fig. 4.5 (b) and (f). The nodal line of HG_{10} beam acts as a marker for the angular spin-Hall shift. In addition, the phase change at the nodal line of the Hermite Gaussian beam does not allow the beam intensity to be shifted along this direction upon scattering and hence we donâĂŹt observe measurable shift along κ_x direction.
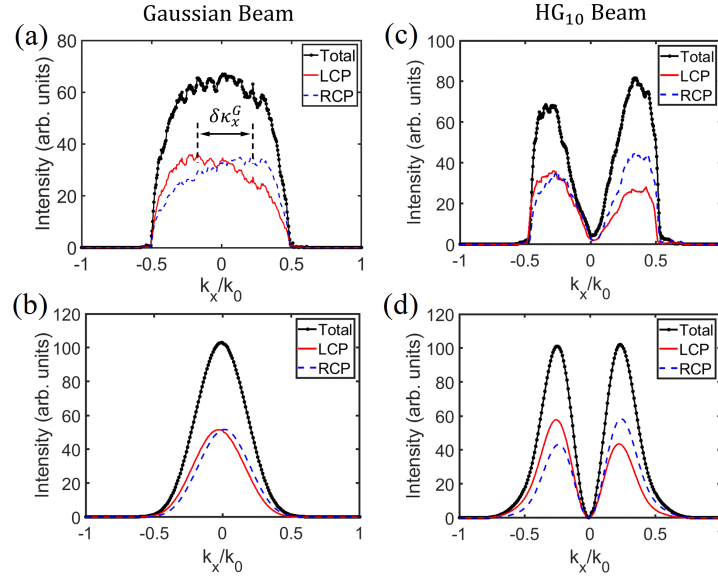
FIGURE 4.7: Calculation of wave-vector shift. Integrated ($\kappa_y = [0, 1]$) intensity distribution profile along κ_x of I, I_+ and I_- components FP for Gaussian beam from (a) experimentally measured and (b) from numerically calculated FP intensity distribution. The corresponding distribution plot for HG_{10} beam from experimentally measured and numerically calculated data is given in (c) and (d) respectively.
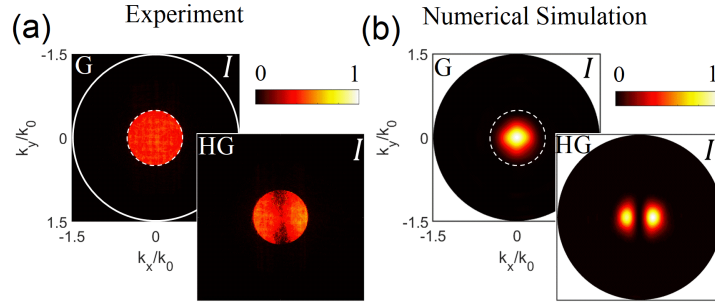
FIGURE 4.8: Comparison of NA of experimental and numerical simulation study. (a) Experimentally measured and (b) numerically simulated FP intensity distribution without any scatterer for Gaussian (G) and HG_0^1 (HG) beam. White dashed circle represents the region of incident NA.

    The shift obtained from the experimentally data and numerically simulated data depict a qualitative comparison of the angular shift between Gaussian and HG_{10} beams. The values differ due to difference in exact focusing conditions as well as due to omission of excitation NA region for experimentally measured FP intensity distribution. The difference can be seen by comparing the far-field intensity distributions of the incident NA region (shown by the white dashed circle) without any scatterer present, as shown in fig. 4.8 (a) and (b) respectively. For experimental excitation condition, the entire incident NA region (shown by the white dashed circle) is filled, whereas, for numerical study it is very difficult to achieve so.

50

Chapter 4. Experimental observation of optical spin-Hall effect and detection of longitudinal spin density of focused-linearly-polarized light
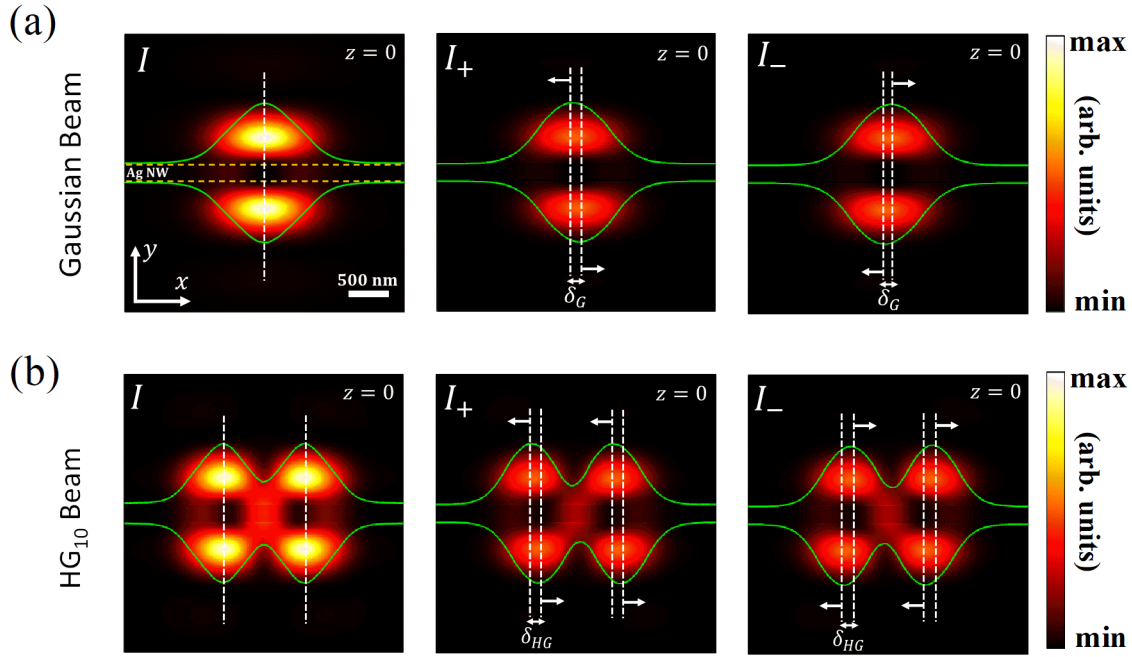
FIGURE 4.9: Numerically calculated scattered electric field intensity distribution at the focal plane ($z = 0$). Normalized electric field intensity distribution corresponding to (a) Gaussian beam and (b) HG_{10} beam. I represents total scattered electric field, I_+ and I_- indicates the LCP and RCP polarized components scattered electric fields respectively. The intensity distribution plot (green line) of lobes in $y > 0$ and $y < 0$ half as a function of x coordinates are super imposed on the figures.

4.5.3 Shift in scattered focal plane intensity distribution

Further investigation of the optical spin-Hall effect is performed through numerical calculation of the scattered electric field from an AgNW at focal plane ($z = 0$ plane) for Gaussian and HG_{10} beams, as shown in fig. 4.9 (a) and (b) respectively. The NW positioned at ($x = 0$, $y = 0$) and along x axis is indicated by the yellow dashed lines. I represents total scattered intensity, I_+ and I_- represents the LCP and RCP analyzed components respectively. The intensity distribution plot of the lobe(s) as a function of x coordinates (green lines) in both $y > 0$ and $y < 0$ halves are superimposed in the figures.

Close inspection of intensity profiles corresponding to I_+ and I_- exhibit that with respect to symmetric intensity profile of I, the intensity lobe(s) in $y > 0$ and $y < 0$ regions of I_+ and I_- show opposite shifts, as indicated by the white arrows. The spatial shift (δ) along x axis can be quantified by calculating the shift of I_+ (or I_-) distribution maxima of each of the lobe(s) in $y > 0$ half with respect to the corresponding lobe(s) in $y < 0$ half. For scattered Gaussian beam the average shift is $\delta_G = 64.0$ nm and that for HG_{10} beam is $\delta_{HG} = 92.2$ nm. The enhancement of the positional shift can be obtained as the ratio $\delta_{HG}/\delta_G = 1.44$. The average shift calculated here are discussed in more general terms as shift vectors in different

systems [117, 118]. The average shifts are consequence of breaking of symmetry in the x-y plane due to the presence of an extended geometry such as a NW. These shift correspond to the angular shift of the intensity distribution of I_+ and I_- components, as discussed in the previous sections.

4.6 Conclusion

To summarize, we have shown numerical and experimental investigation of generation of longitudinal spin density through focusing of linearly polarized Gaussian beam and HG_{10} beam. In addition, circular polarization analysis of the forward elastic scattered optical field from an AgNW reveals intrinsic spin-Hall effect. The measurement of the far-field longitudinal spin density (s_3) for Gaussian and HG_{10} beam indicates enhancement of s_3 for HG_{10} beam compared to Gaussian beam, quantified by the enhancement factor $\eta_{exp} = 1.31$. By studying the focal optical fields, we attribute the observed effect to the generation of longitudinally spinning optical fields due to focusing, hinting the geometrical origin of the effect.

The chapter therefore discusses the very intricate nature of the spin-orbit interaction between non paraxial optical fields and nanoscopic scatterers. The method presented here discusses a simple polarization analysis-based approach for measuring longitudinal spin of optical fields. Similar method has also been employed for measuring the spin of linearly polarized dipoles realized by optical excitation of dipolar metal particles [116]. The directional scattering from dipolar particles have also been analyzed to reveal the transverse spin of polarized and unpolarized optical fields [119, 120], angular momentum interconversion [110] as well as used for position sensing [108, 109]. Hence the scattered signal for a nanoscopic scatterer such as a single silver nanowire possess rich information about optical fields and can potentially be useful for investigation of polarized signals as well as SOI phenomenon such as angular momentum interconversion.

Chapter 5

Investigation of optothermal interactions of active colloids in focused and defocused Gaussian beam

Abstract:

In this chapter, I will discuss about optothermal interaction active colloids under the influence of illuminated focused and defocused optical field. Specifically, we harness the self heating colloids and harness their thermophoretic behaviour to study optothermal interaction which shows a long-range attraction and a short-range repulsion between the colloids. The optical gradient field enabled attraction and the short-range repulsion between the active colloids have been harnessed to form re-configurable dynamic assembly. In addition, the assembly undergoes self-evolution as a new colloid joins the structure. Further, we show that the incident polarization state of the optical field can be employed as a parameter to modulate the structural orientation of the active colloidal matter. This chapter is an adaptation of the research article referenced as arXiv:2203.08904 [121]

5.1 Introduction and motivation

One of the most unique feature of light matter interaction is optical forces, first proposed by Ashkin [5–7]. The optical forces have been extensively harnessed to facilitate optical tweezers to trap and manipulate colloidal matter as well as to investigate their dynamics [25, 49, 53, 71–73, 122–124]. The strong optical field required for optical tweezing can also facilitate optical heating, resulting in optothermal interactions in a fluidic environment. It has been employed to trap and manipulate colloids through thermophoresis [36–38, 44, 125], thermo-osmosis [40, 126, 127], depletion [41] as well as to understand the non-equilibrium nature of the interaction [42]. In this context, artificial active matter has become an important system of study specifically because it can self-propel, absorbing energy from the environment and can mimic systems which are out of thermodynamic equilibrium [128–

53

134]. Similar to naturally occurring active matter systems such as swimming bacteria [135, 136] and flocks of birds [137, 138], these systems provide a test bed for many biophysical and cellular phenomena.

Interaction of an artificial active colloid with an optical field leads to heating and consequent release of thermal energy, resulting in a non uniform temperature distribution in the surrounding region. This acts as an environmental cue to influence normal Brownian motion of the colloids, leading to thermophoreis [36, 37]. For self-heating colloids, this effect can be harnessed for self-thermophoretic propulsion [133], feedback-controlled ordering of colloids [131] as well as for studying microscopic engines [139]. As such, generating and studying the dynamic assembly of colloidal matter is particularly interesting because these can lead to better understanding of the collective dynamics and act as a model for various biological systems [132, 140, 141]. To this end, previous approaches of generating spatio-temporally ordered assembly involved holographic optical trapping as well as multiplexing of the incident optical beams to trap multiple colloids [65–67, 131, 133, 142]. However, a single optical beam enabled spatio-temporal ordering of active colloids remains to be explored in detail.

Motivated by that, herein we report spatio-temporal ordering of iron oxide infused polystyrene active colloids (PS ACs) in a defocused laser trap. The colloids undergo self-thermophoretic motion under asymmetric laser illumination, rendering their active nature. In addition, the temperature distribution generated due to heating colloids act as an environmental cue for the colloids in the vicinity. The resulting thermophoretic motion of the colloids towards the heat center render a long-range attraction and a short-range repulsion between a trapped and a migrating colloid. Upon encountering the defocused optical field, the counteracting effect of attraction due to optical gradient potential and short-range repulsion due to thermal gradient, the colloids form ordered assembly as shown in the schematic fig. 5.1 (a) and timeseries fig. 5.1 (d) (Video 1) [143]. Unlike the active colloids, passive colloids (1.01 μm polystyrene colloids in aqueous medium) do not exhibit any active dynamics in the defocused optical field and get trapped to form a two-dimensional array (Video 2) [143].

5.2 Experimental implementation and characterisation

5.2.1 Experimental implementation

The dynamics of the polstyrene active colloids (PS ACs) employed for the study are achieved by dispersing them within a microchamber (height ~ 100 μm) enclosed with two glass coverslips. It is placed on a piezo stage and a two channel optical microscope enables
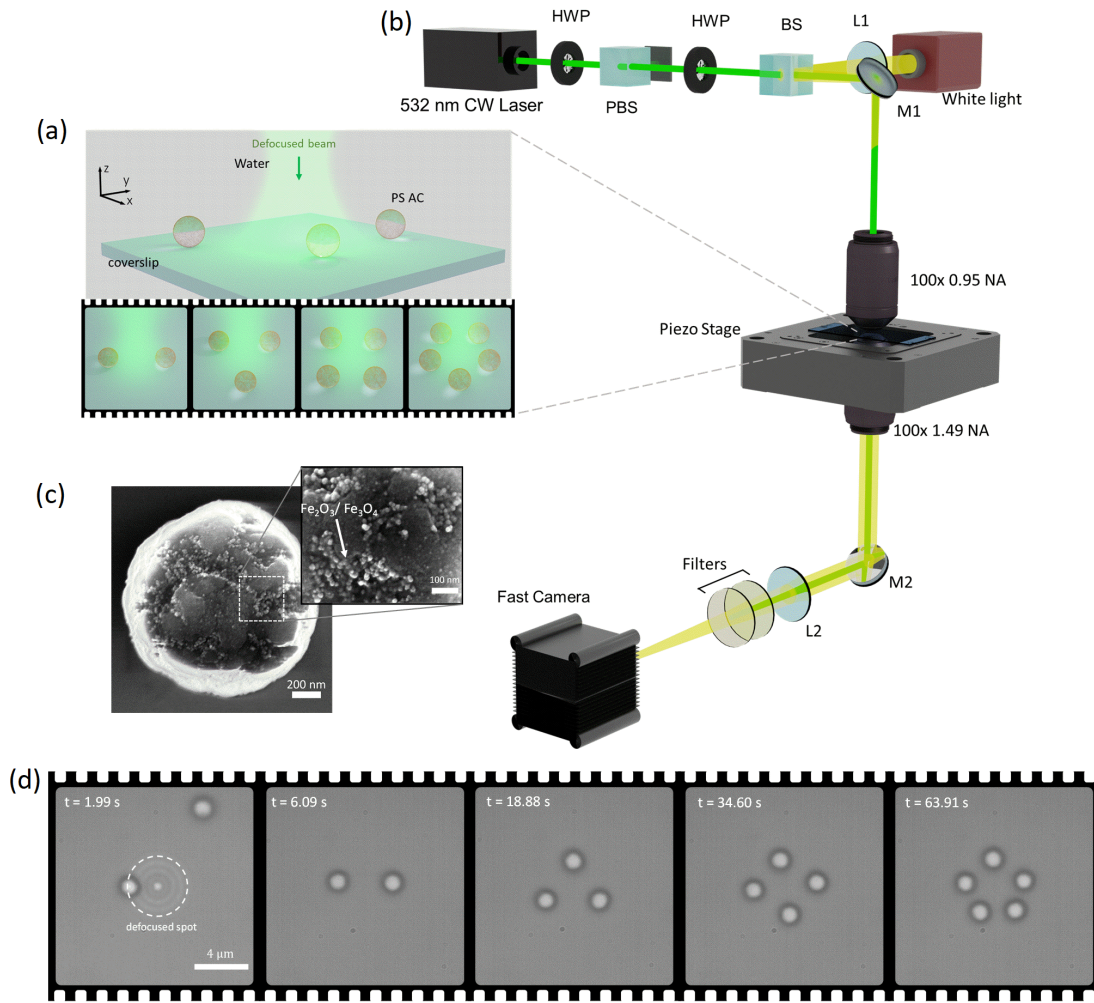
FIGURE 5.1: Optothermal assembly of reconfigurable colloidal matter. (a) Schematic of assembly of polystyrene active colloids (PS ACs) in an defocused Gaussian field. (b) A dual channel optical microscope setup is used for the experiments. A $100\times$ 0.95 NA objective lens is used for focusing/defocusing of incident laser at wavelength $\lambda = 532$ nm and a $100\times$ 1.49 NA lens is used to collect the signal and projected onto the Fast camera ($100 - 1000$ fps) using relay optics. (c) Scanning electron micrograph of a PS AC shows the embedded $Fe_2O_3/Fe_3O_4 \sim 15$ nm nanoparticles with $\sim 30\%$ mass fraction. (d) Timeseries of the assembly of PS ACs under a defocused illumination.

illumination of $\lambda = 532$ nm laser beam from the top-side using $100\times$ 0.95 NA lens and collection of the signal from the bottom-side with $100\times$ 1.49 NA objective lens, as shown in fig 5.1 (b). Continuous variation of the laser power is performed by using a combination of half-wave plate (HWP) and polarizing beam-splitter (PBS). The excitation wavelength from the collected signal is rejected by using a combination of notch and edge filter and the signal is projected to a fast camera (fps $100 - 1000$) to record the dynamics of the PS ACs. The architecture of the optical setup has been elaborated in section 2.1.3 of chapter 2.The trajectories of the dynamics are extracted by employing Trackmate [144]. The experimental

design allows us to independently modulate the focusing conditions of the excitation beam from the collection path.

5.2.2 Composition of PS ACs and calculation of effective parameters

The colloids employed for the experimental investigations are composed of polystyrene having diameter 1.31 μm with nanoparticulate (diameter $\sim$ 15 nm) iron oxide (Fe_2O_3/Fe_3O_4) distributed ($\sim$ 30% mass fraction) throughout the pores within the polymer colloid interior, rendering them symmetric (Microparticles GmbH) as shown in fig. 5.1 (c). Each nanoparticle act like a point heat source and collectively they lead to asymmetric temperature distribution due to absorption of asymmetrically incident laser beam, rendering the colloids active.

Considering the iron oxide inclusions distributed uniformly through out the polystyrene active colloids, we can get the estimate of effective dielectric constant (ε_{eff}) of PS ACs by employing Maxwell-Garnett effective medium approximation as [145],

$$\frac{\varepsilon_{\text{eff}}}{\varepsilon_{\text{PS}}} = \frac{1 + 2\phi\frac{\varepsilon_{\text{i}}-\varepsilon_{\text{PS}}}{\varepsilon_{\text{i}}+2\varepsilon_{\text{PS}}}}{1 - \phi\frac{\varepsilon_{\text{i}}-\varepsilon_{\text{PS}}}{\varepsilon_{\text{i}}+2\varepsilon_{\text{PS}}}} \tag{5.1}$$

where ε_i and ε_{PS} are the dielectric constant of the iron oxide inclusions and polystyrene respectively. The volume fraction of the iron oxide inclusions (Fe_2O_3/Fe_3O_3) is obtained by assuming a thin shell (thickness t) of iron oxide around a passive dielectric polystyrene sphere, the combination of both results in a sphere of radius $R = 1.31\,\mu$m. The 30% mass fraction of the of iron oxide inclusion in the PS ACs results in volume fraction $\phi = 7.7\%$. Assuming, $Fe_2O_3 : Fe_3O_3 = 1 : 1$, the effective dielectric constant turns out to be $\varepsilon_{\text{eff}} = 2.8145 + 0.0567i$, leading to effective refractive index $n_{\text{eff}} = \sqrt{\varepsilon_{\text{eff}}} = 1.6777 + 0.0169i$.

Similarly to get the effective thermal conductivity(κ_{eff}) we have used Maxwell's formula as[146],

$$\frac{\kappa_{\text{eff}}}{\kappa_{\text{PS}}} = 1 + \frac{3\phi}{\frac{\kappa_{\text{i}}+2\kappa_{\text{PS}}}{\kappa_{\text{i}}-2\kappa_{\text{PS}}} - \phi}. \tag{5.2}$$

Where κ_{i} and κ_{PS} are the thermal conductivity of the inclusion and the polystyrene media respectively. We get effective thermal conductivity as $\kappa_{\text{eff}} = 0.1861$.

Following are the medium property used for the calculations

Material	Polystyrene	Fe_2O_3	Fe_3O_4	Inclusion
ε	2.5546	$10.3810 + 3.6546i$	$5.4933 + 0.4344i$	$7.9371 + 2.0445i$
$\kappa\,(\text{W}\,\text{m}^{-1}\,\text{K}^{-1})$	0.15	7	17.65	12.33

TABLE 5.1: Material properties used for the calculation of effective parameters.

5.2.3 Calculation of diffusion coefficient

The bulk diffusion constant for a freely diffusing PS AC can be obtained theoretically by considering the equation $D_0 = k_B T/\gamma_0$ where k_B is the Boltzmann Constant, T absolute temperature, and $\gamma_0 = 6\pi\eta_0 a$ is the bulk viscous coefficient, a radius of PS AC and η_0 bulk viscosity of the fluid. Experimentally, the diffusion constant of a colloid can be obtained analysis of the trajectory of the freely diffusing colloids and fitting the calculated of mean square displacement (MSD) with the equation $\mathrm{MSD}(\tau) = 4D\tau$, where τ represents lagtime, as shown in fig. 5.2 (a). The measured value $D = 0.14 \ \mu\mathrm{m^2 s^{-1}}$ is lower than the bulk diffusion coefficient ($D_0 = 0.33 \ \mu\mathrm{m^2 s^{-1}}$). The difference can be attributed to their proximity to the glass surface [52, 147] and is discussed below.

Near to a surface, these values (D, γ, η) differ significantly from the corresponding bulk value and a correction factor α has to be considered α is given by (see fig. 5.2 (b)):

$$\alpha = \frac{\gamma}{\gamma_0} = \frac{\eta}{\eta_0} = \frac{D_0}{D} \tag{5.3}$$

$$\alpha^{-1}(h) = 1 - \frac{9}{16}\left(\frac{a}{h}\right) + \frac{1}{8}\left(\frac{a}{h}\right)^3 - \frac{45}{256}\left(\frac{a}{h}\right)^4 - \frac{1}{16}\left(\frac{a}{h}\right)^5 + \ldots \tag{5.4}$$

Thus, $\alpha^{-1} = D/D_0 = 0.42$, indicates the distance of the colloid from the surface. Comparing this value to the Fig. 5.2 (c), we find $h/a = 1.09$, implies that PS ACs are very close to the surface.

The freely diffusing PS ACs in the vicinity of an optically trapped and heated colloid undergo thermophoretic motion towards the heated region as a result of the generated temperature gradient [37]. Therefore, in the following section we discuss about the temperature
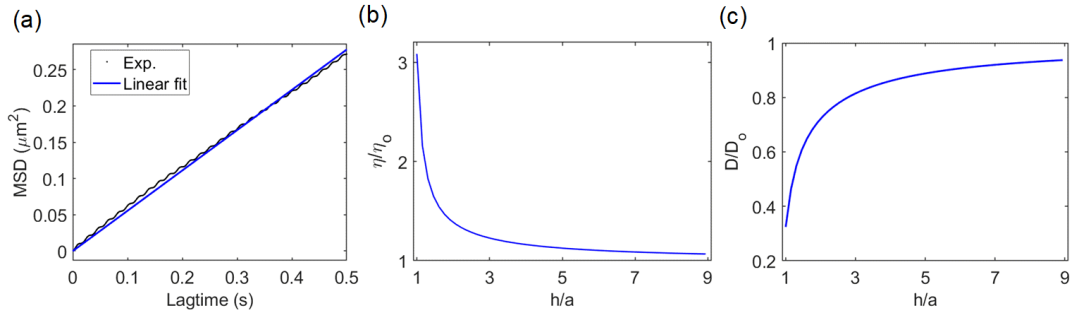
FIGURE 5.2: Diffusion constant of PS AC. (a) Diffusion constant is obtained by fitting of experimentally measured MSD with $\mathrm{MSD}(\tau) = 4D\tau$, ($\tau$ is the lag time). (b) Variation of bulk viscosity of water (η) as a function of distance from the surface. η near a surface deviates significantly from the bulk value η_0. (c) Deviation of diffusion constant (D) from its bulk value (D$_0$) as a function of distance from the glass surface.

generated due to optical heating and corresponding measurement technique.

5.3   Temperature measurement technique

The nanoparticulate iron oxide infused within the polystyrene interior of the colloid acts like heat sources upon absorption of incident optical field and facilitate corresponding optothermal effects. The maximum surface of a heated PS AC can be obtained by studying the nematic to isotropic phase transition of 5CB liquid crystal (phase transition temperature $T_{pt} = 35°$ C$= 308$ K)[133, 148], as shown in the schematic in fig. 5.3 (a).

The temperature distribution due to uniform optical heating of a colloid with maximum surface temperature ΔT_0 can be given by, $\Delta T(r) = \Delta T_0 \frac{a}{r}$, where a is the radius of the colloid [40]. The surrounding 5CB medium undergoes nematic to isotropic phase transition in the region where $T(r) \geq 308$ K. Due to the difference of refractive index of nematic and isotropic phase of the 5CB, the boundary of phase transition can be clearly visible in bright field as shown in fig. 5.3 (b) for a centrally heated immobile PS AC with a focused laser beam. Therefore, measuring the radius of the phase transition boundary (R) leads to the
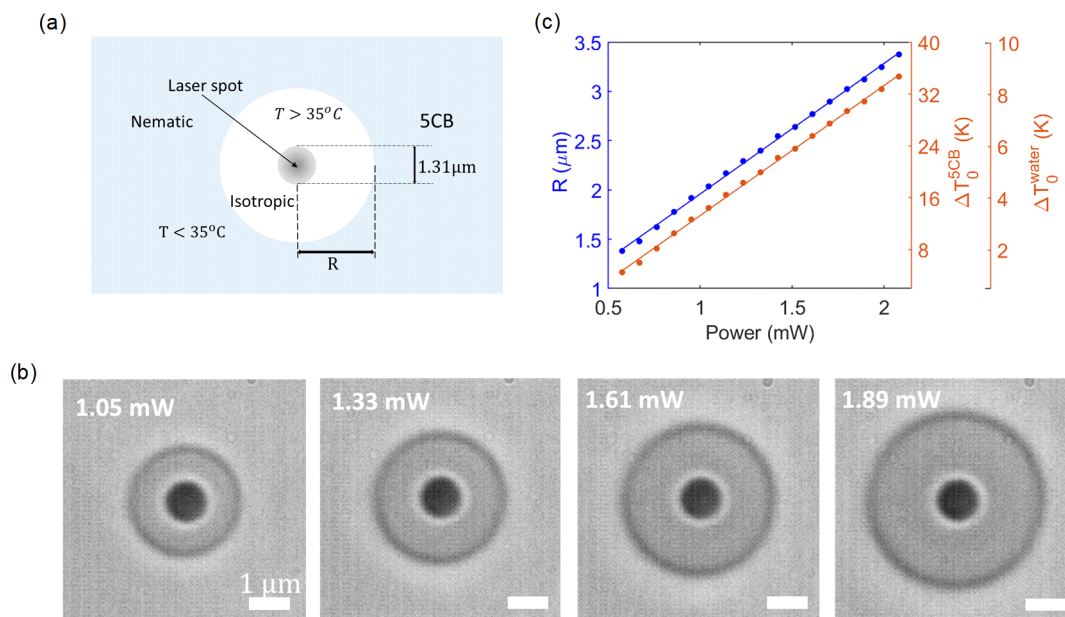
FIGURE 5.3: Temperature measurement using 5CB liquid crystal. (a) The measurement technique utilises an immobile PS AC heated centrally with 532 nm laser and the resulting phase transition due to temperature distribution in the surrounding region.(b) The bright field optical image of 5CB phase transition for incremental incident laser power shows increase of isotropic region radius. (c) The maximum surface temperature of the PS AC increases linearly with the laser power.

estimation of the maximum surface temperature of the heated PS AC from the equation,

$$\Delta T_0 = (T_{pt} - 298\,K)\frac{R - a}{a}.$$ (5.5)

In addition, the measured temperature increment on the surface of PS AC due to laser absorption is inversely proportional to the thermal conductivity of the surrounding 5CB medium (κ_{5CB}). Hence, measurement of the increment in 5CB medium ΔT_0^{5CB} leads to estimation of the temperature increment in the aqueous medium ΔT_0^{water} by employing the equation,

$$\Delta T_0^{water} = \Delta T_0^{5CB}\frac{\kappa_{5CB}}{\kappa_{water}}.$$ (5.6)

where, $\kappa_{water} = 0.60\ Wm^{-1}K^{-1}$ and $\kappa_{5CB} = 0.15\ Wm^{-1}K^{-1}$. The temperature increment scales linearly with the incident laser power with equation $\Delta T\,[K] = 0.801\,P_0\,[mW] - 1.658$, as shown in fig. 5.3 (c)

5.4 Optical trapping and self-thermophoretic motion of the colloids in focused laser Gaussian beam

The freely diffusing PS ACs in the vicinity of an optically trapped and heated colloid undergo thermophoretic motion towards the heated region as a consequence of the generated temperature gradient [36]. Additionally, the self-heating of the PS ACs undergoing thermophoretic motion leads to short-range repulsion between a trapped and an incoming colloid. Finally, under the collective influence of the defocused optical field and the generated thermal gradient, the PS ACs attain a dynamic equilibrium to form a stable structural orientation as shown in Fig. 1(d) (Video 1). Thus, to understand the phenomena, it is important to first investigate the dynamic characteristics of individual PS AC in an focused optical trap.

5.4.1 Optical trapping of the colloids

The colloids undergo trapping under the action of gradient optical force due to a focused laser beam. The gradient optical force and the consequent trap stiffness for the colloids can be determined by tacking the position distribution of the colloids in very low power, such that the effect of thermal gradient remains minimal [52].

Fig. 5.4 shows the power dependence of the trap stiffness of a PS AC trapped with a focused optical field. As expected, the trap stiffness scales linearly with increasing power as $k\,[pN/\mu m] = 1.53\,P_0\,[mW] - 0.12$.
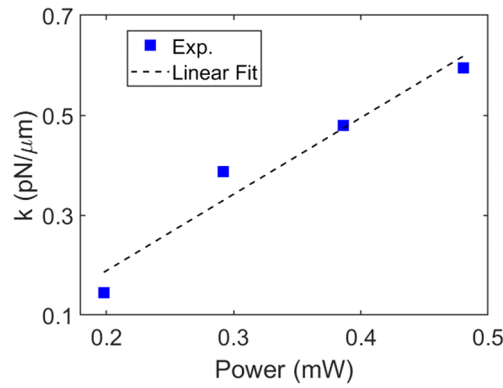
FIGURE 5.4: Variation of the optical trap stiffness (k) as a function of the incident laser power (P_0), showing linear dependence.

5.4.2 Self-thermophoretic behaviour of the colloids

With increasing laser power, the large optical field at the focal spot leads to heating of the PS ACs [34]. The vectorial nature of the optical field at the focal spot in addition to the motion of the colloid leads to asymmetric heating of the trapped colloid. The generated thermal gradient along the surface of the colloid results in an interfacial flow of fluid, confined to a thin layer along the colloid surface, termed as thermo-osmotic slip flow [39, 40, 126, 127], and consequent self-thermophoretic motion of the trapped colloid. Such self-thermophoretic motion of colloids have been investigated for Janus colloids [126] as well as symmetric microswimmers [131, 133]. As a result, the colloid settles in an off-center position (δx) where the harmonic optical force ($F_{\text{opt}} = k \, \delta x$, k is trap stiffness) pulling the colloid towards the center balances the thermal gradient induced drift force ($F_{\text{drift}} = \gamma v = -\gamma D_T \nabla T$, D_T is thermo-diffusion coefficient, γ represent bulk viscous coefficient), resulting from the fluid flow, as shown in fig. 5.5 (a). Fig. 5.5 (b) shows the power dependence of the distance from the focus center (δx) at which the colloids gets trapped, which exhibits non-linear trend (Video 3 [143]).

Experimental insight into the maximum surface temperature which drives such self-thermophoretic behaviour is extracted using 5CB liquid crystal as a media as explained in section 5.3. Fig. 5.5 (c) shows the nematic to isotropic transition of liquid crystal around a centrally heated immobile PS AC at laser power $P_0 = 2 \, \text{mW}$. The maximum temperature increment on the surface scales linearly with increasing laser power as shown in fig. 5.5 (d).

To further study the trapping state, we study the non-linear power dependence of the off-center position by considering temperature dependence of the thermo-diffusion coefficient (D_T) as well as the Soret coefficient (S_T, $S_T = D_T/D_0$). In addition, we also investigate the associated forces and drift velocity.
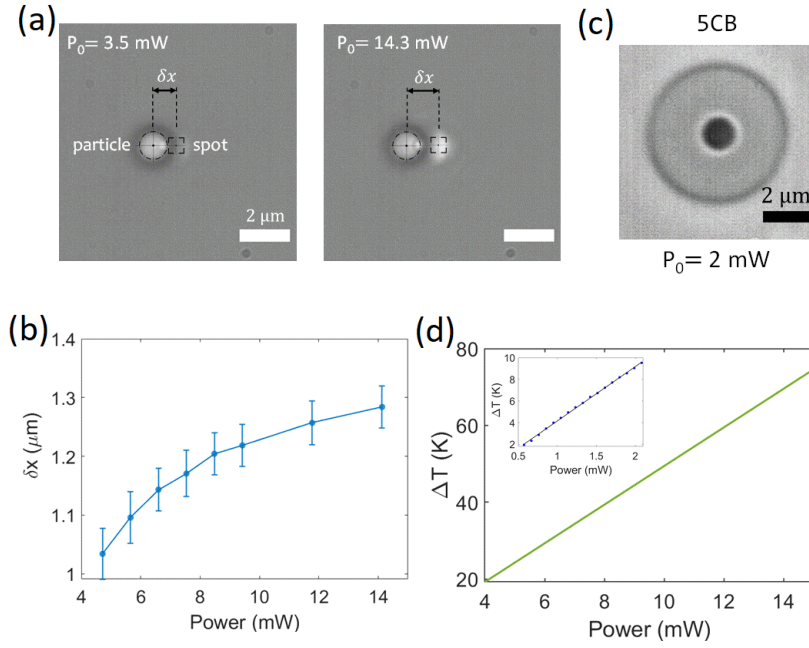
FIGURE 5.5: Self-thermophoretic motion of a PS AC in the optical trap. (a) A trapped PS AC heats up and undergoes self-thermophoresis resulting from thermo-osmotic slipping of fluid along the colloid surface and settles in an off-center position. (b) The equilibrium position of the trapped PS AC from the focal spot increases non-linearly with the laser power. (c) A bright-field optical image of 5CB liquid crystal phase transition from nematic to isotropic around an immobilised centrally heated PS AC at power $P_0 = 2.0$ mW. (d) Temperature increment of the PS AC as a function of laser power is estimated from the radius of the isotropic phase region. Temperature increment at higher laser power can be estimated by extrapolating the measured temperature increment at lower power shown in the inset.

A. Examination of non-linearity of off-center position:

To analyse the non-linear dependence of the δx of the trapped colloid with increasing laser power, δx is plotted against the estimated temperature increment of the colloid, obtained by $\Delta T^{\text{est}} = \Delta T^{\text{exp}} e^{-\delta x^2/2w_0^2}$, where ΔT^{exp} is the experimentally measured temperature of an immobile centrally heated PS AC, and $w_0 = 0.8$ μm is the beam waist. The plot is shown in fig. 5.6 (a). The data was then fitted in the following ways:

- **Case 1:** Considering temperature dependence of D_T, i.e, $D_T = C(T - T^*)$
  Considering temperature dependence of thermo-diffusion coefficient: $D_T = C(T - T^*)$
  (T^* is the sign inversion temperature) [149], we get,

$$\delta x = \left(\frac{\gamma C \Delta T_0 a}{k} \right)^{1/3} (T - T^*)^{1/3} \qquad (5.7)$$
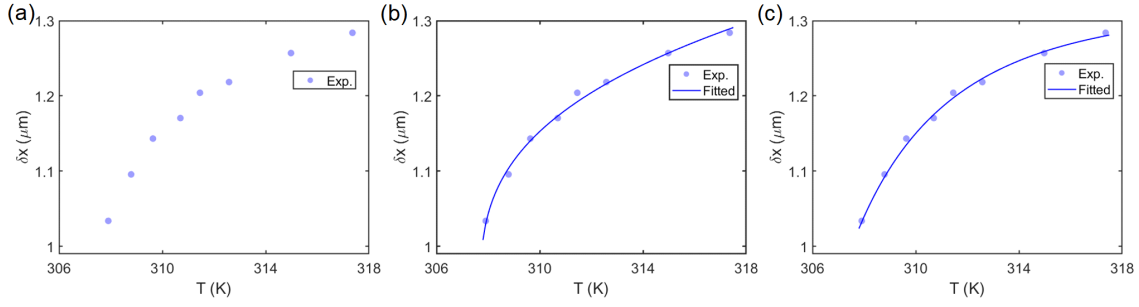
FIGURE 5.6: Analysis of non-linear slipping distance. (a) The off-center distance of the trapped colloid as a function of estimated temperature increment. (b) The data is fitted according to case 1, from which we obtain $T^* = 307.7$ K. (c) The data is fitted with equation 5.9 and obtained the fitting parameter are $T^* = 304.9$ K and $T_f = 4.173$ K.

where, γ is the viscosity, a is the radius of the particle, k is the trap stiffness and ΔT_0 is the increment in temperature of the trapped colloid. Since both ΔT_0 and the k has linear power dependence, the above equation reduces to the form: $\delta x = A(T - T^*)^{1/3}$. Fig. 5.6 (b) shows the corresponding fitted plot with equation, $\delta x = A(T - T^*)^{1/3} + B$. From the plot we can extract the parameter $T^* = 307.7$ K.

- **Case 2:** Considering temperature dependence of S_T, i.e, $S_T = S_T^\infty \left(1 - e^{(T^* - T)/T_f}\right)$

Considering temperature dependence of Soret coefficient: $S_T = S_T^\infty \left(1 - e^{(T^* - T)/T_f}\right)$ (S_T^∞ is high temperature limit of the S_T and T^* and T_f are Soret inversion temperature and fitting parameter respectively) [149–151], we get,

$$\delta x = \left(\frac{k_B \Delta T_0 a S_T^\infty}{k}\right)^{1/3} \left(T \left(1 - e^{(T^* - T)/T_f}\right)\right)^{1/3} \tag{5.8}$$

where, k_B is Boltzmann constant, a is the radius of the particle, k is the trap stiffness and ΔT_0 is the increment in temperature of the trapped particle. As before, since both ΔT_0 and the k has linear power dependence, the above equation reduces to the form:

$$\delta x = A \left(T \left(1 - e^{(T^* - T)/T_f}\right)\right)^{1/3} \tag{5.9}$$

Fitting the data in fig. 5.6 (a) with the equation yields $T^* = 304.9$ K and $T_f = 4.173$ K, shown in fig. 5.6 (c).

Therefore, T^* value obtained from both the cases are similar to values reported in various literature for variety of colloids [149–151]. Hence, temperate dependence of thermo-diffusion coefficient and the Soret coefficient can offer possible explanation for the non-linear dependence of the off-center position (δx) of the trapped colloid with increasing laser
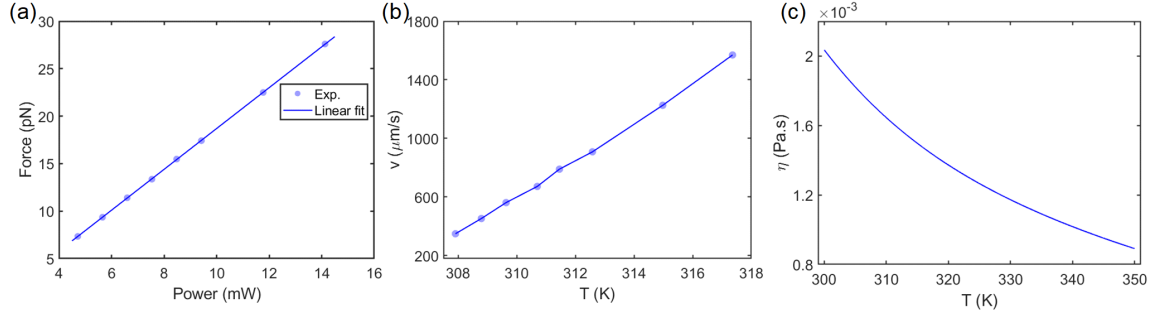
FIGURE 5.7: Analysis of optical trapping state. (a) Optical gradient force as function of laser power with experimentally measured off-center distance ($\delta s = x$) and power dependence of the trap-stiffness. (b) The drift velocity as a function of the estimated maximum temperature of the colloid is obtained by diving the optical gradient force (F_{opt}) by the bulk viscous coefficient (γ). (c) Temperature dependence of the dynamic viscosity (η).

power.

B. Estimation of optical force and drift velocity:

The off-center trapping state of the colloid can be further analyzed by quantification of the optical gradient forces and the corresponding thermal drift velocity. Fig. 5.7 (a) shows the calculated optical force $F_{opt} = k\delta x$, acting on the off-center (δx) trapped colloid. The approximate values of the trap stiffness k at a given power is estimated from its power dependence as described in section 5.4.1. As before, the extent of heating can be estimated by $\Delta T^{est} = \Delta T^{exp} e^{-\delta x^2/2w_0^2}$, where $w_0 = 0.8\ \mu m$ is the beam waist and ΔT^{exp} is the experimentally measured temperature of an immobile centrally heated colloid. The approximate temperature gradient can be calculated by: $|\nabla T(\delta x)| = \Delta T^{exp}\, a/\delta x^2$ which is of the order $\sim 10^7\ K\, m^{-1}$.

The consequent drift velocity generated due to presence of temperature gradient can be calculated by balancing of the forces, i.e., $v = k\delta x/\gamma$. Fig. 5.7 (b) show the corresponding increase of drift velocity with estimated increment of the temperature of the colloid $T = \Delta T^{est} + T_s$ ($T_s = 298\ K$ is the surrounding temperature). The calculation incorporates the temperature dependence of the dynamic viscosity (η), as shown in fig. 5.7 (c), corrected with the factor ($f = 1/0.42 = 2.38$) which considers the distance from the glass surface (see section 5.2.3).

$$\eta(T) = f \left(1.380 - 2.122 \cdot 10^{-2}\, T + 1.360 \cdot 10^{-4}\, T^2 - 4.645 \cdot 10^{-7}\, T^3\right) \tag{5.10}$$

The thermophoretic velocity of the colloid can be represented as:

$$v = \frac{2}{3}\chi\beta\frac{\nabla T}{T} \tag{5.11}$$

where, χ is the thermo-osmotic coefficient and $\beta = 2\,\kappa_{\mathrm{w}}/(2\,\kappa_{\mathrm{w}} + \kappa_{\mathrm{PS}}) \approx 1.3$ ($\kappa_{\mathrm{w}} = 0.6$ W m^{-1} K^{-1} and $\kappa_{\mathrm{PS}} = 0.186$ W m^{-1} K^{-1}), accounts for the difference in thermal conductivities. Considering $v \sim 5\cdot10^2\ \mu$m s^{-1} and T ~ 300 K, the ratio $v/(\frac{\nabla T}{T}) = \frac{2}{3}\chi\beta \approx 1.50 \cdot 10^{-8}$ m^{2}s^{-1}. This leads to rough estimation of the parameter $\chi \sim 1.73 \cdot 10^{-8}$ m^2 s^{-1}. With the thermophoretic velocity defined as $v = -\mathrm{D_T}\nabla T$, the order of magnitude of approximate value of thermo-diffusion coefficient turns out to be $\mathrm{D_T} = 2\chi/3\mathrm{T} \approx 38.5\ \mu$m^2 K^{-1} s^{-1}.

5.4.3 Polarization dependence of self-thermophoretic motion

The direction of self-thermophoretic drift of the colloid upon heating due to asymmetric laser illumination depends on the polarization of the incident laser beam (Video 4 [143]). For a y polarized focused beam, the trapped PS AC drifts along x direction and vice-versa for x polarized focused beam, as shown in fig. 5.8 (a) respectively. Further quantification of this polarization dependence is performed by calculating MSD for y polarized case and fitting it with $\mathrm{MSD}(\tau) = 2k_BT/k[1 - e^{-|\tau|/\tau_{ot}}]$, where τ is the lag time and $\tau_{ot} = \gamma/k$ is
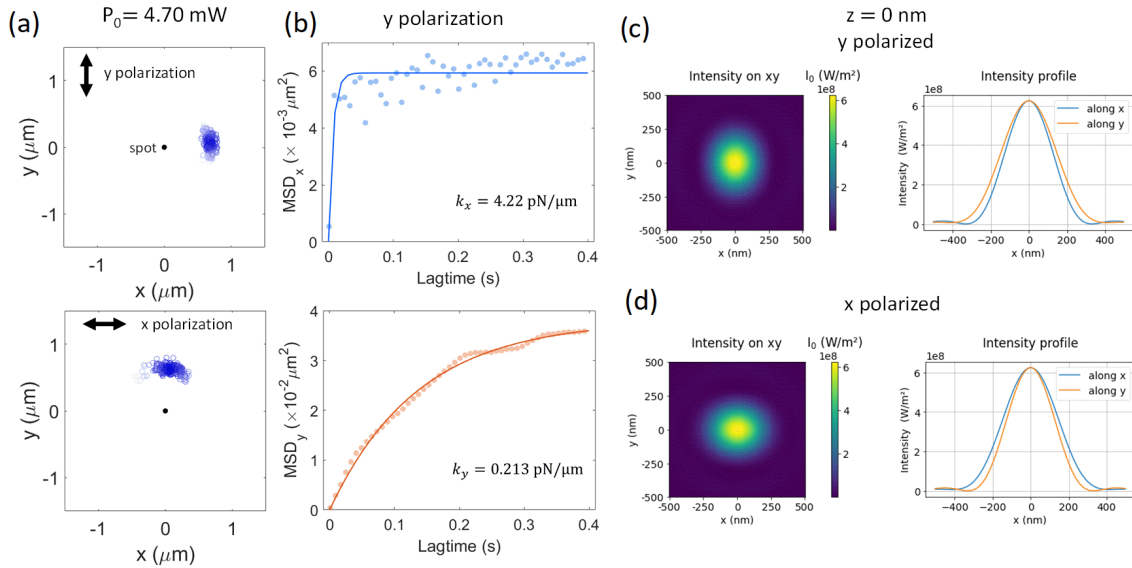
FIGURE 5.8: Polarization dependence of the self-thermophoretic motion.(a) A colloid undergoes self-thermophoretic motion along x direction for y polarized beam and along y direction for x polarized beam. (b) The corresponding spring constant (k_x, k_y) for y polarized incident beam is obtained by calculating corresponding MSD in x (MSD$_x$) and y (MSD$_y$) direction and is more along x direction compared to the y direction. Numerically calculated focal ($z = 0$ nm) electric field intensity distribution and corresponding line profile along x and y axis for (c) focused y and (d) x polarized incident beam.

trap characteristic time [52]. Fig. 5.8 (b) shows the MSD along x (MSD_x) and y (MSD_y) direction for y polarized incident beam. The corresponding trap stiffness along x direction $k_x = 4.22$ pN/μm is one order magnitude more than that in the y direction $k_y = 0.213$ pN/μm. This effect can be attributed to the ellipsoidal shape of the electric field intensity distribution at the focus, with major axis along the linear polarization direction, contributing to the heating, shown in fig. 5.8 (c) and (d). In such cases, a colloid can drift along the minor axis (x direction for y polarized beam and vice versa for x polarized beam), which will lead to lesser heating at a given distance from the potential minima compared to the same distance along major axis and hence the forces can be balanced relatively easily. Therefore, for y polarized beam, the colloid drifts in x direction due to the self-thermophoretic effect, which in this case represents both the minor axis and radial direction, and consequently is pulled towards the center along this x axis due to the optical gradient force ($\mathrm{F_{opt}} = k(\mathrm{P_0}) \cdot \delta x \approx 4.9$ pN).

This polarization dependence of the self-thermophoretic drifting direction opens up an additional parameter for manipulation of propulsion direction of active colloids. Further, the temperature distribution set up by a trapped and heated colloid results in an environmental cue for the motion of the freely diffusing PS ACs leading to unconventional interaction between them, which is discussed below.

5.5 Effect on surrounding colloids: Thermophoretic hovering

The heating of a trapped colloid due to a focused Gaussian beam generates an environmental cue, which leads to thermophoretic motion of the PS ACs in the surrounding region towards the heat center. The experimental results indicate that a second colloid migrates towards the heat center due to thermophoresis and eventually near to the trapped colloid undergoes hovering at a certain distance, shown in fig. 5.9 (a). Fig. 5.9 (b) shows the position distribution of the tapped and hovering PS ACs. It can be seen that, at the trapping laser power of $\mathrm{P_0} = 3.6$ mW, the hovering occurs at distance ≈ 2.59 μm. The temperature increment of the trapped colloid can be estimated by the $\Delta \mathrm{T^{est}} = \Delta \mathrm{T^{exp}} e^{-\delta x^2/2w_0^2}$, which assumes uniform heating of the off-center ($\delta x = -0.5$ μm) trapped colloid. The corresponding temperature distribution due to the trapped colloid will approximately vary as, $\mathrm{T}(r) = \Delta \mathrm{T} a/r + \mathrm{T_0}$, where r is the distance and a is the radius of the colloid, $\Delta \mathrm{T}$ is the temperature increment on the surface of the trapped colloid, $\mathrm{T_0} = 298$ K is the ambient temperature. The generated radially symmetric temperature distribution is shown in fig. 5.9 (c). Inset shows the line profile of the temperature increment along x axis.
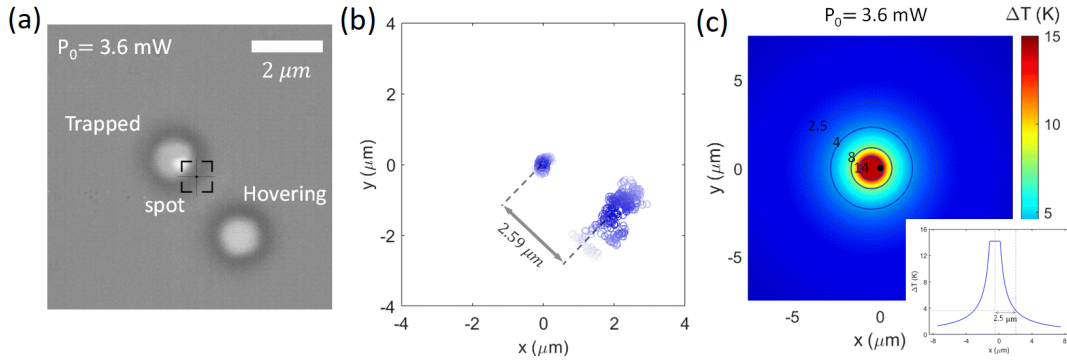
FIGURE 5.9: Thermophoretic hovering of PS AC. (a) A heated trapped colloid at the focal spot results in temperature distribution in the surrounding medium. A second PS AC undergoes thermophoretic migration towards the heat center and eventually hovers near a trapped colloid at a certain distance. (b) Position distribution of the trapped and hovering colloid. (c) The temperature distribution that can be generated due to off-center trapped ($\delta x = -0.5$ μm)colloid at power $P_0 = 3.6$ mW can be estimated from the experimentally measured temperature using 5CB, which assumes uniform heating. The corresponding line profile along x axis is shown in the inset.

The colloids migrate towards the heat center, indicating their negative Soret coefficient (S_T). However, the hovering resulting from thermophoretic repulsion can be attributed to temperature dependence of S_T, i.e., assuming $S_T = S_T^\infty(1 - e^{(T^*-T)/T_f})$ [150, 151]. T^* represents the temperature at which S_T inverts sign and T_f is a fitting parameter. For the experimental data, the temperature increment at the region where the hovering occurs ($d \approx 2.5$ μm) is $\Delta T \approx 4$ K for $\Delta T_{max} \approx 14.2$ K of the trapped colloid, as shown in fig. 5.9(c), implying $T^* \approx 302$ K, similar to the value of T^* for various colloids [150, 151]. Closer to heat center from that region S_T may invert its sign, resulting in inversion of thermophoretic velocity $v = -D_T\nabla T$ ($D_T = S_T D_0$ is thermo-diffusion coefficient). Alternatively, encountering some scattered light near to a trapped colloid, the incoming colloid may attain a temperature $T \geq T(r)$ due to its absorption. Consequently, the migrating PS AC no longer encounters a positive thermal gradient (∇T) and become zero or switches its sign near to this position. Hence the thermophoretic velocity $v = -D_T\nabla T$ may have a value close to 0 or invert its sign around this region. Any motion away or towards the trapped colloid will render fluctuation of the thermophoretic velocity sign, leading to the hovering of the second colloid. The hovering distance depends on the temperature distribution due to the first colloid and hence can be modulated by changing the laser power, as shown in fig. 5.10 (Video 5 [143]).

Thus, a heated colloid leads to a long-range attraction acting up to distance 10-12 μm due to thermophoretic migration other colloids and a short-range repulsion acting in the range 1-5 μm depending on the incident laser power, leading to their thermophoretic hovering. Such behaviour is significantly different from that of passive dielectric colloids, and creates an avenue for understanding as well as modification of collective dynamics of active matter
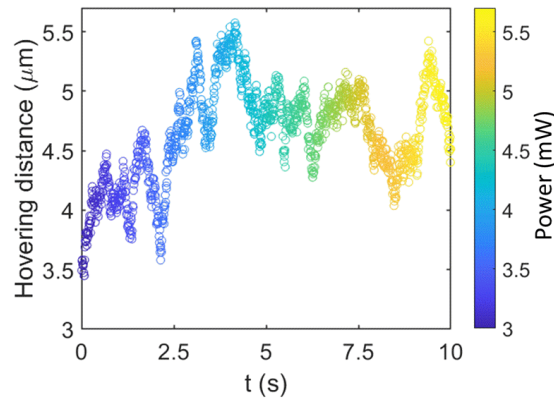
FIGURE 5.10: Variation of the distance between a trapped PS AC and a hovering PS AC with increasing laser power extracted from Video 5. [143]

systems [138].

It is worthwhile to notice the fluctuations in the position of the second colloid. While multiplexing of incident beam or implementing holography it is possible to trap the second colloid and study its dynamics due to environmental perturbations, in the following sections we show a simple defocused Gaussian beam can serve similar purpose.

5.6 Optothermal interaction of PS ACs in defocused Gaussian beam

While a focused beam can lead to hovering of the colloids around a trapped PS AC, a defocused beam can provide the mean for equal optical trapping of multiple colloids and heating them to equal extent. Hence, such configuration enables us to investigate the optothermal interaction and collective dynamics of multiple colloids. To start with, we characterize the defocused optical field distribution and exerted force on the the colloids.

5.6.1 Spatial distribution of trapping potential and gradient force due to defocsued illumination

The optical field intensity distribution due to defocused Gaussian beam illumination is shown in fig. 5.11 (a). The defocused beam has a central high intensity part followed by concentric Airy rings forming a circular optical field region. The defocusing was done upto the extent of $\sim 4\,\mu$m. This can be quantified in terms of the depth of focus $\text{DOF} = \lambda/(2\text{NA}^2)$, where λ is the wavelength of light, usually taken as 550 nm, NA is the numerical aperture of the objective lens. For the objective lens used for the incident optical field, Olympus M Plan
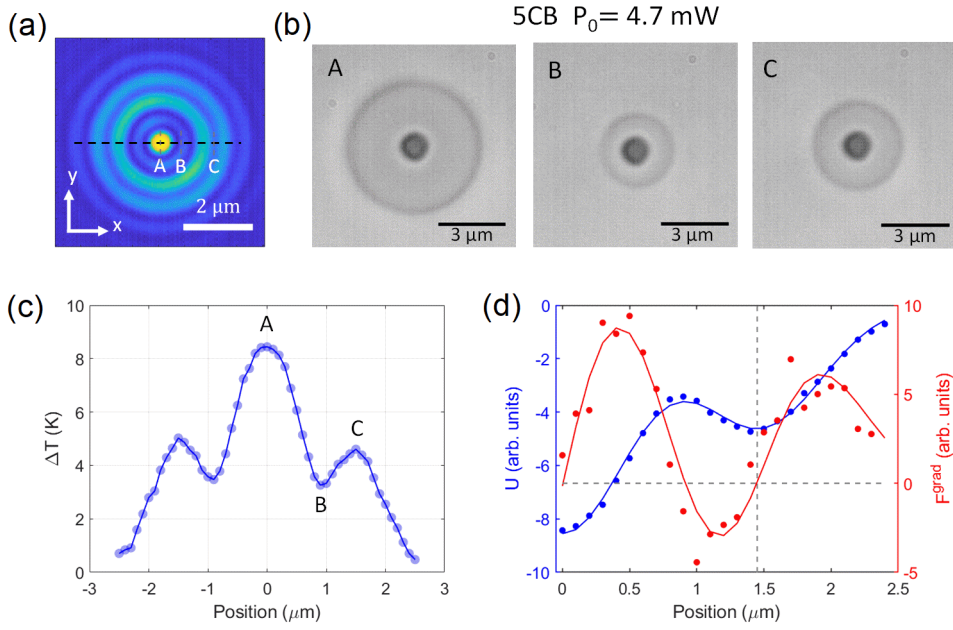
FIGURE 5.11: Optical gradient potential and force profile. (a) Incident optical field intensity profile. (b) Bright field optical image of 5CB phase transition due to heating of an immobile PS AC placed in different points of the optical field at laser power $P_0 = 4.7$ mW. (c) Extracted temperature profile along a dashed black line in (a). (d) The corresponding calculated optical potential and the optical gradient force line profile fitted with double Gaussian function.
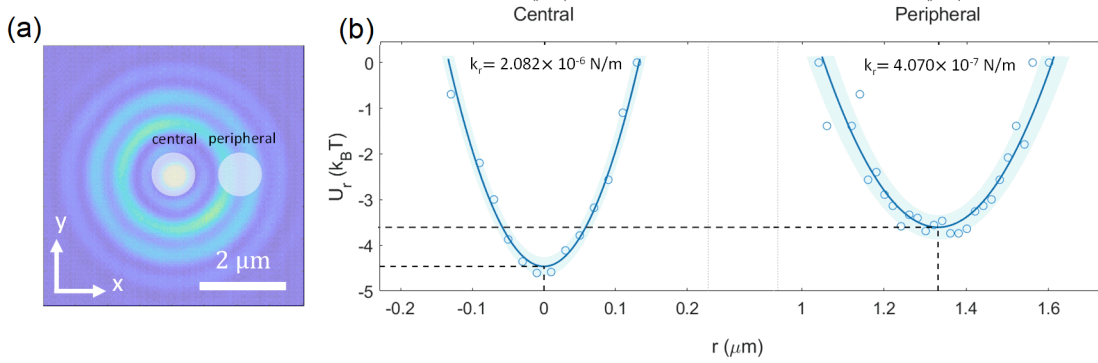
FIGURE 5.12: Estimation of radial trapping potential for defocused illumination. (a) The passive PS colloids gets trapped in two regions of the optical field in the central part and in the peripheral ring region. (b) The corresponding radial trapping potential. The trap stiffness is more for trapped colloid in the central region and the potential has a minimum ≈ -4.4 $k_B T$ and trap stiffness $k_r \approx 2.082$ pN/μm. The peripheral region has minima ≈ -3.6 $k_B T$ and trap stiffness $k_r \approx 0.407$ pN/μm.

Apo $100\times$ 0.95 NA lens, DOF $\sim 0.3\,\mu$m. Therefore, the defocusing distance was fixed to ~ 13 DOF.

To extract the profile of the optical gradient potential and force in the sample plane we scan an immobile PS AC in 5CB medium along a line in the optical field (shown by black

dashed line). The temperature increment of the colloid is dependent on the spatial profile of the optical field. Fig. 5.11 (b) shows the generation of isotropic phase of 5CB due to increment of surface temperature of the PS AC in three different points as indicated in fig. 5.11 (a). The temperature profile along a line parallel to x axis (as shown by black dashed line in fig. 5.11 (a)) is shown in fig. 5.11 (c). The increment in temperature is directly proportional to the intensity profile. Since the optical trapping potential is also proportional to the intensity profile of the incident optical field, the temperature profile also gives us a qualitative measure of the optical gradient potential. Fig. 5.11 (d) shows a qualitative profile of optical trapping potential (in blue fitted with double Gaussian function) and the corresponding optical gradient force profile (in red). The approximate trapping position is at the secondary minima of the optical potential and have been indicated by the grey dashed lines.

The quantitative measure between the trapping potential at center of the beam and at the peripheral region can be obtained by trapping passive polystyrene particles having diameter 1.01 μm in the defocused optical field at laser power $P_0 = 14$ mW (Video 2 [143]) and analysing the resulting trapping characteristics.

The passive colloids get trapped in the optical field in two regions − central region and the peripheral ring region as shown in fig. 5.12 (a). The measured radial trapping potential and the trap stiffness is more for the centrally trapped colloid with respect to the peripherally trapped colloid as can be seen from fig. 5.12 (b). For the centrally trapped colloid the minima of the trapping potential were found to be $U_r^{\text{cent}} \approx -4.4$ $k_B T$ and trap stiffness $k_r \approx 2.082$ pN/μm. On the other hand, trapping potential for the trapped colloid in the peripheral ring region has minima $U_r^{\text{peri}} \approx -3.6$ $k_B T$ and trap stiffness $k_r \approx 0.407$ pN/μm. The force on the particle at the central spot is approximately an order of magnitude higher than that in the peripheral region.

5.6.2   Dynamic of PS ACs in defocused Gaussian beam

The arrangement of two PS ACs in a defocused Gaussian optical field is shown in fig. 5.13 (a) along with the intensity profile in the xy plane. The colloids are trapped in diametrically opposite positions. The black spot indicates the beam center. The diametrically opposite trapping position shown in fig. 5.13 (a) can be attributed to the fact that each of the PS ACs get heated up to equal extent under the effect of optical field and hence leads to repulsion due to thermal field of each other. The interparticle distance depends on the extent of defocusing as well as the incident laser power. Fig. 5.13 (b) shows that for fixed defocusing, the interparticle distance (d) increases non-linearly with power. The non-linearity can be attributed to the self-thermophoretic motion of the colloids as well as their repulsion from
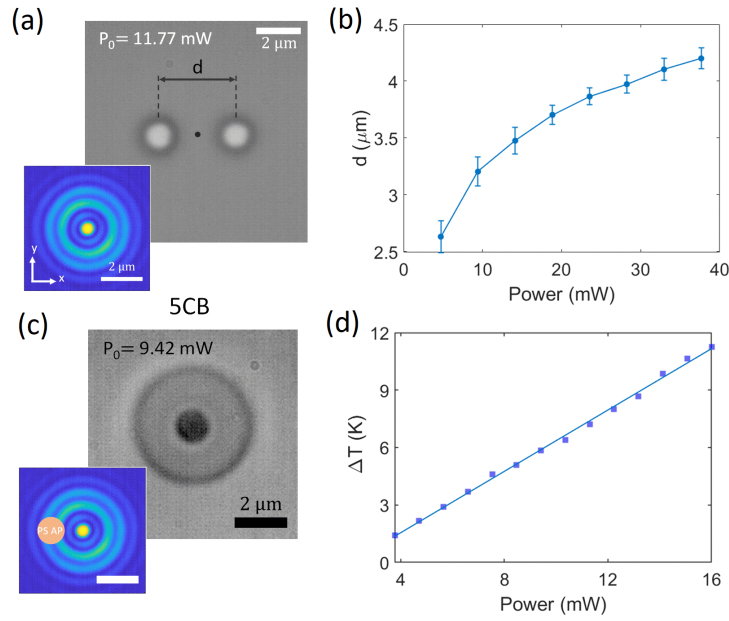
FIGURE 5.13: Dynamics of colloidal pair in defocused optical trap. (a) Two PS ACs gets trapped in diametrically opposite position. (b) For a fixed defocusing (diameter ~ 4 μm), the interparticle distance increases non-linearly as the laser power is increased. (c) Bright-field optical image of 5CB liquid crystal phase transition from nematic to isotropic around a heated immobilised PS AC with a defocused laser power $P_0 = 9.42$ mW. The position of the colloid with respect to the defocused spot is indicated in the inset. (d) Temperature increment of the PS AC as a increases linearly with laser power.

each other. To find out the approximate maximum temperature of a PS AC under such defocused illumination we study the nematic to isotropic transition of 5CB liquid crystal around a heated colloid shown in fig. 5.13 (c). The inset shows the approximate position of the PS AC at the defocused spot. The maximum temperature variation with power is shown in fig. 5.13 (d). The maximum temperature increment attained by a single colloid due to incident laser power of $P_0 = 16$ mW does not exceed ≈ 12 K.

In addition to their diametrically opposite arrangement, their orientation along an axis can be modulated by changing the incident laser polarization state as shown in fig. 5.14 (a). The two PS ACs orient themselves along x direction for y polarized beam and vice-versa for x polarized incident beam (Video 6 [143]). The inset shows the position distribution obtained over 8 seconds. The trapping state for y polarized incident beam (laser power $P_0 = 11.77$ mW) is further characterized by calculating the MSD along x (MSD_x) and y (MSD_y) direction and obtaining the corresponding trap-stiffness as shown in fig. 5.14 (b). The obtained trap-stiffness along x direction $k_x = 0.362$ pN/μm is one order of magnitude higher than that of along y direction $k_y = 0.058$ pN/μm. The result could be understood considering their diametrically opposite arrangement along x axis and resulting
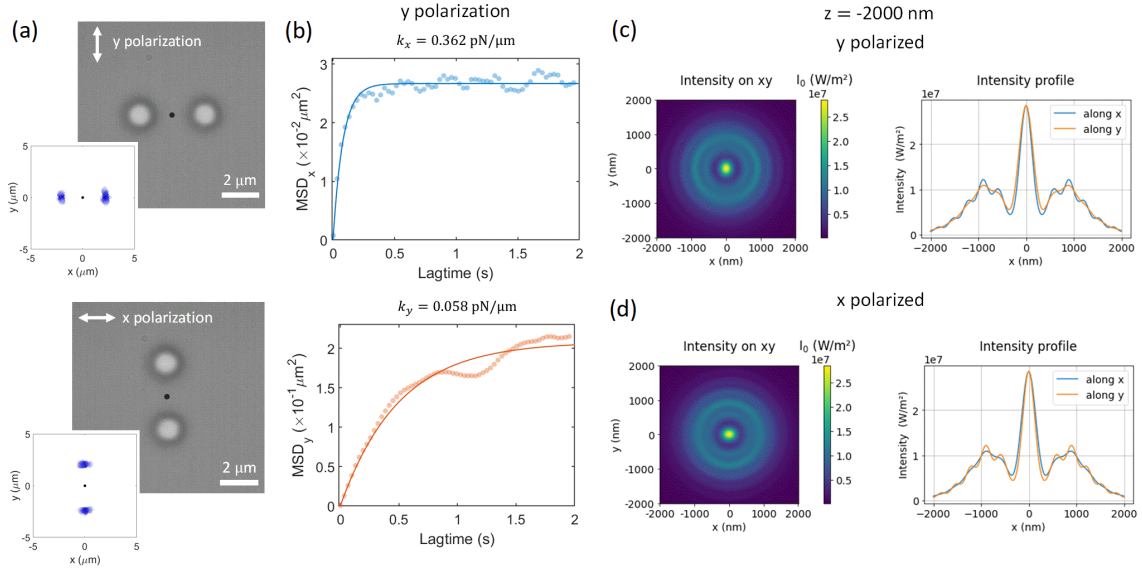
FIGURE 5.14: Polarization dependence of the arrangement. (a) The orientation of the PS ACs in the defocused spot depends on the polarization of incident beam. The colloids stay along x direction for y polarized beam and stay along y direction for x polarized beam. (b) Calculated MSD_x and MSD_y and the corresponding trap-stiffness of the colloids for y polarized incident beam. Numerically calculated defocused ($z = 2000$ nm) electric field intensity distribution and corresponding line profile along x and y axis for (c) focused y and (d) x polarized incident beam.

thermophoretic repulsive force and gradient optical field force acts along x axis. The polarization dependence of the orientation can be attributed to the electric field intensity distribution under such defocused illumination and the corresponding optical forces as shown in fig. 5.14 (c) and (d). The normalized electric field intensity distribution is more along x direction for y polarized beam and more along y direction for x polarized beam, resulting in higher gradient optical potential as well as confinement along that direction.

5.6.3 Optical gradient potential and force on PS ACs in defocused field

The optical gradient potential as well as force acting on the PS ACs due to the defocused optical field has been estimated through evaluation of the trap stiffness from the time series data (Video 1 [143]) at laser power P_0=14.13 mW. 450 frames have been considered in the calculation during the time frame where two colloids are oriented along the x axis due to the y-polarization of the illumination beam.

The optical gradient potential is higher along the x direction with respect to the y direction as shown in fig. 5.15. Consequently, the trap stiffness which quantifies the optical gradient force, $k_x \approx 0.447$ pN/μm is more with respect to $k_y \approx 0.035$ pN/μm. The variation of the values can be understood by considering their orientation in the optical field.

Numerically the gradient optical force on the active colloids have been estimated by modelling the colloids using Maxwell-Garnett effective medium theory [145, 146] (section

5.2.2) and evaluating the force in the defocused optical. It has been achieve through numerical calculation of the optical defocused field for x and y polarized incident field using PyFocus [152] and employing equation 1.4 for calculation of gradient optical force component.

Fig. 5.16 shows the numerically calculated optical force on the active colloids at laser power $P_0 = 10$ mW. The approximate position of trapping of the active colloid is indicated by white dashed circle in the first column and grey dashed circles in the second and third column. The optical forces are slightly higher perpendicular to the polarization direction. Although these are approximate calculation, the order of magnitudes match with the experimentally obtained trap stiffness. In addition, we have also calculated the axial optical scattering and gradient force by employing equation 1.4 for both focused ($z = 0$ nm) and defocused ($z = -2000$ nm) cases at laser power $P_0 = 10\,\mathrm{mW}$. The results have been shown in fig. 5.17 (a) and (b) for focused and defocused beam respectively. The colloids experience an axial scattering force, F_z^{scat} in the order of $\sim$ pN due to focused beam at laser power $P_0 = 10\,\mathrm{mW}$ and gradient force $F_z^{Grad} \sim 1$ pN. On the other hand, for defocused optical field, the colloids experiences $F_z^{scat} \sim 0.01$ pN as well as gradient force $F_z^{Grad} \sim 0.1$ pN also plays a crucial role in their trapping near to the glass surface.

The coupled motion of the PS ACs in the defocused laser beam is reminiscent of many biological active matters as well as of fundamental importance due to the synchronization of motion through environmental cues. The activity induced self-evolution is characteristic of all naturally occurring active matter systems and motivates the investigation of dynamic assembly of multiple active colloids.
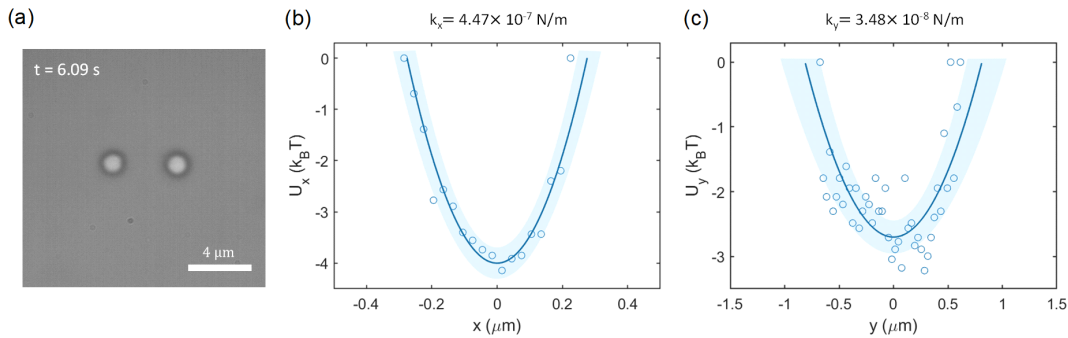
FIGURE 5.15: Calculation of optical gradient potential on active colloids for defocused illumination. (a) assembly of two colloids oriented along x axis in the defocused field. Optical gradient potential along (a) x axis and (b) y axis on the active colloids due to the y polarized defocused illumination. The potential and the trap are much stiffer along x axis compared to the y direction.
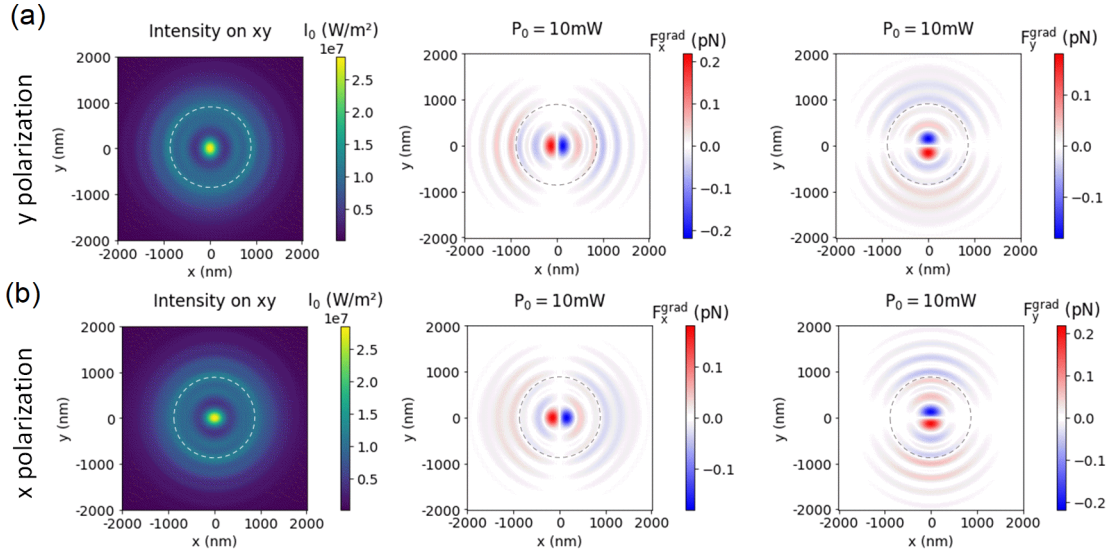
FIGURE 5.16: Numerical calculation of optical gradient force. Incident optical field (I_0), optical gradient force along x direction (F_x^{grad}) and y direction (F_y^{grad}) for (a) y polarized beam and (b) x polarized incident beam at power $P_0 = 10$ mW. White dashed circle in first column and grey dashed circles in second and third column indicates the approximate radial position of colloid trapping.
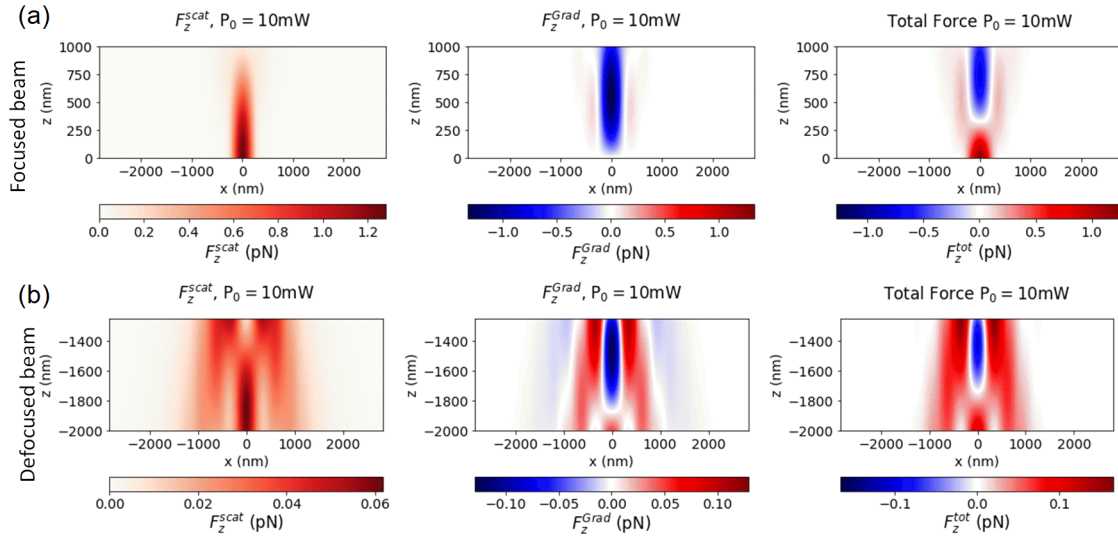
FIGURE 5.17: Numerica calculation of axial force on PS AC. Axial scattering (F_z^{scat}), gradient (F_z^{Grad}) as well as total force on a PS AC for (a) focused ($z = 0$ nm) and (b) defocused ($z = -2000$ nm) optical field.

5.7 Self evolution of the colloidal matter

Trapped PS ACs in the defocused laser spot generate a temperature distribution in the surrounding region and result in thermophoretic motion of other colloids in the vicinity. The
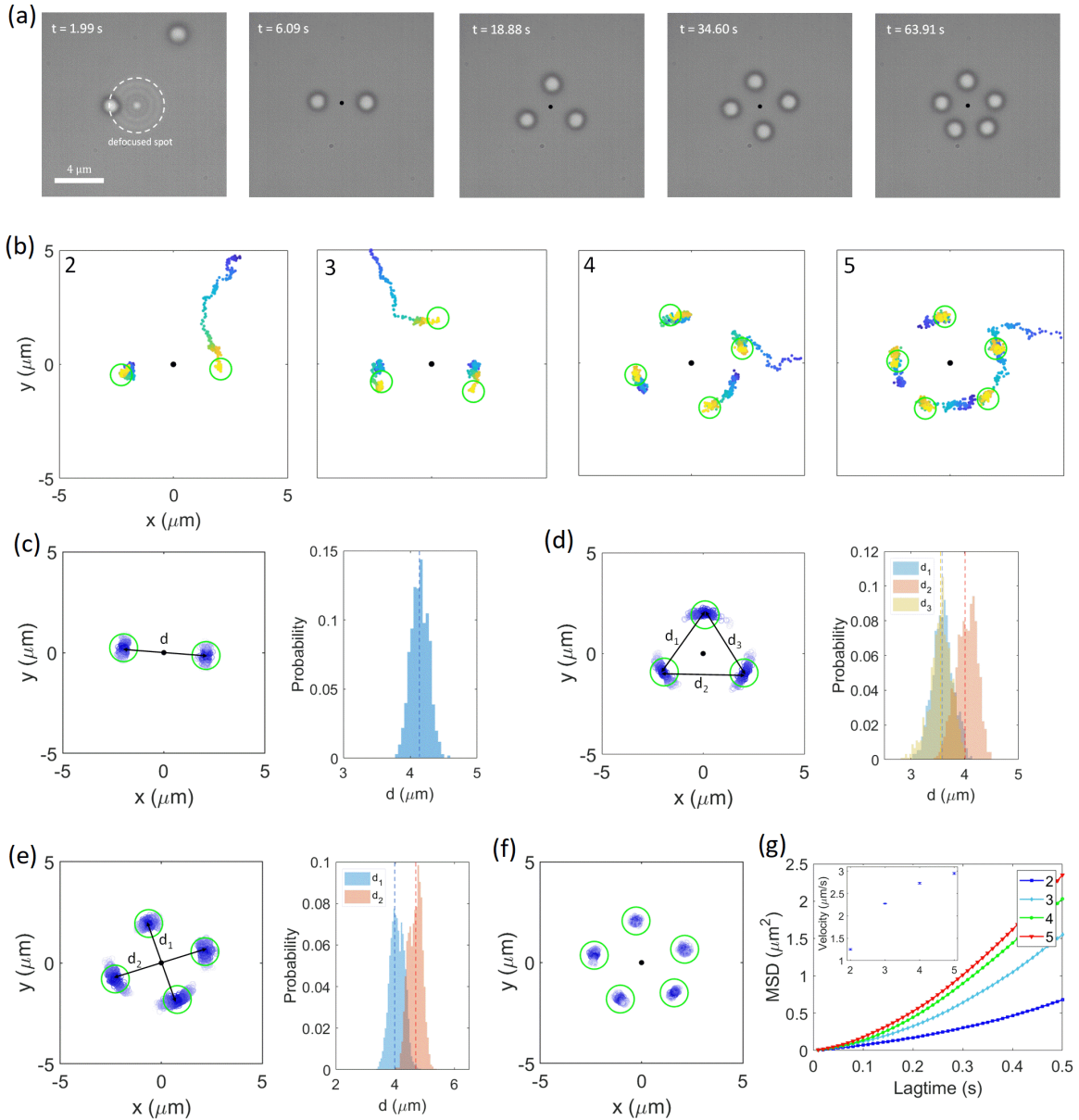
FIGURE 5.18: Self-evolution of active colloidal matter under defocused illumination. (a) The time series of the assembly under a defocused illumination at $P_0 = 14.13$ mW. Black spot indicates the position of beam center (b) As a new colloid joins the assembly, the existing PS ACs re-position themselves in the assembly and forms a dynamic structure with the new colloid included. The dynamic equilibrium positions are indicated by the green open circles. (c) Two PS ACs settle in diametrically opposite position having average distance $d = 4.14$ μm, (d) Three in the vertices of a triangle with the distances between the colloids having distribution about $d_1 = d_3 \approx 3.57$ μm and $d_2 = 4.02$ μm. (e) Four PS ACs form a diamond shaped quadrilateral geometry having diagonal distance distribution about $d_1 = 4.07$ μm and $d_2 = 4.68$ μm. (f) Five PS ACs form a pentagonal geometry. (g) The thermophoretic velocity of an incoming colloid is obtained by investigating the mean-squared displacements (MSDs). The obtained velocity (given in the inset) of an incoming colloid show incremental trend.

described experimental arrangement can thus lead to self-evolution of the structures as multiple PS ACs migrate towards the spatio-temporally static optical field. The primary driving mechanism for this assembly is the thermophoretic behaviour of the active colloids due to generated temperature gradient as well as the optical gradient force facilitated spatio-temporal trapping. Fig. 5.18 (a) shows the dynamic assembly of multiple PS ACs as they migrate one by one towards the heated colloids in a y polarized defocused beam (Video 1 [143]). The self-evolution of the dynamically stable structures is shown in fig. 5.18 (b). It can be seen that as a new colloid joins the structure, the existing colloidal arrangement re-organizes to form a stable assembly with the new colloid. In contrast, passive colloids (polystyrene 1.01 μm) do not exhibit active motion under such illumination configuration and get trapped to form two dimensional array (Video 2 [143]).

The dynamic property of assembly of two PS ACs trapped in diametrically opposite position is quantified by their position distribution and their distance as shown in fig. 5.18 (c). The distance between the colloids is shown in the histogram with average distance ≈ 4.14 μm. The assembly evolves into a triangle with three PS ACs as shown in fig. 5.18 (d), with each colloid settling at the vertices. The distance between the colloids is indicated in the histogram, with two distributions having mean ≈ 3.57 μm and ≈ 4.02 μm. The larger distance between the horizontally oriented colloids is due to the electric field intensity distribution of y polarized beam. Four PS ACs reorganize themselves to form a diamond shaped quadrilateral structure as shown in fig. 5.18 (e). The diagonal distance between the colloids exhibits two distributions with average ≈ 4.07 μm and ≈ 4.68 μm. The larger distance is between the colloids aligned horizontally and similar to the three PS AC case, it can be attributed to the polarization dependent electric field intensity distribution in the sample plane and the corresponding optical gradient forces. Five colloids lead to formation of a pentagonal structure as shown in fig. 5.18 (f). It is important to note that the exact nature of the dynamic structure formation depends on the identical characteristic of the colloids, deformed or smaller/bigger sized colloids might lead to formation of skewed geometry in
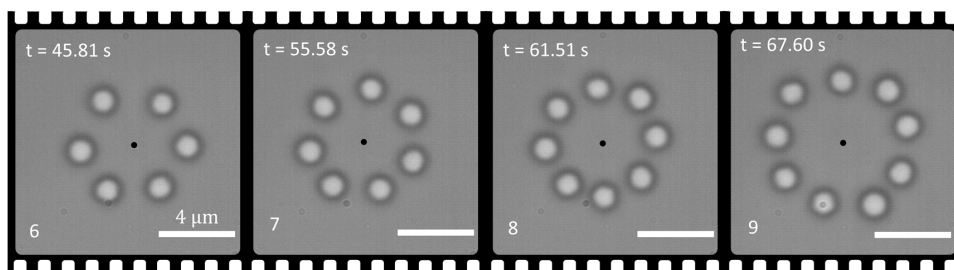
FIGURE 5.19: Colloidal assembly with higher number of colloids. With increasing time, and for larger defocusing, dynamic assembly for 6-9 PS ACs can also be formed. The black spot indicates the beam center. (Video 7 [143])

comparison to the ideal ones.

As the number of colloids in the assembly increase, the maximum temperature attained by the system increases. It is followed by the increased velocity (v) of the directed motion with which a new colloid joins the assembly and can be found out by considering the mean squared displacement (MSD). The MSD for such a directed motion is given by $MSD(\tau) = v^2\tau^2 + 4D\tau$, τ being the lag time [129]. Fig. 5.18 (g) shows the mean-squared displacement of the nth colloid as they undergo thermophoretic motion towards the assembly of $(n-1)$ colloid(s). The corresponding velocity (v) is shown in the inset and indicates an increasing trend having $v = 1.25\,\mu\text{m s}^{-1}$ for the second colloid to $v = 2.94\,\mu\text{m s}^{-1}$ for the fifth colloid.

Higher number of colloids can also form a stable colloidal matter through this process, as shown in Fig. 5.19 (Video 7 [143]). With a denser colloidal solution, the structure can evolve to form dynamic assembly of higher number of colloids in short time. However, it must be noted that the defocusing of the incident laser has to be increased for this purpose to ensure sufficient distance between two colloids in the assembly. This is because of the fact that a colloid can be repelled due to thermal gradient from the optical potential if the distance between two colloids become very less.

5.8   Investigation of thermophoresis, thermal convection and scattering forces

5.8.1   Calculation of Soret Coefficient

Since, the assembly process is driven by the thermophoresis of the colloids, in this section we make an attempt to approximate the Soret Coefficient by ignoring its temperature dependence for simplicity.. From the thermophoretic velocity (v) of second PS AC under the influence of temperature distribution set up by the first PS AC, we can obtain the thermo-diffusion coefficient (D_T) by employing the equation, $v = -D_T \nabla T$. Here $T = T_s + \Delta T_0 \frac{a}{r}$ is the absolute temperature, T_s is the ambient temperature and ΔT_0 is the maximum surface temperature of heated PS AC. Therefore, the trajectory ($r(t)$) of the incoming second PS AC is given by,

$$r(t) = (A + B\,t)^{1/3}. \tag{5.12}$$

where, $A = r_0{}^3$ and $B = 3D_T\Delta T_0 a$.

Thus, by fitting $r(t)$ vs. t between two PS ACs we can obtain D_T. Then, the Soret coefficient can be obtained as $S_T = \frac{D_T}{D}$. If $S_T > 0$ then the AC will move to the colder region and if $S_T < 0$, then the AC will move to the hotter region.

(a) (b)
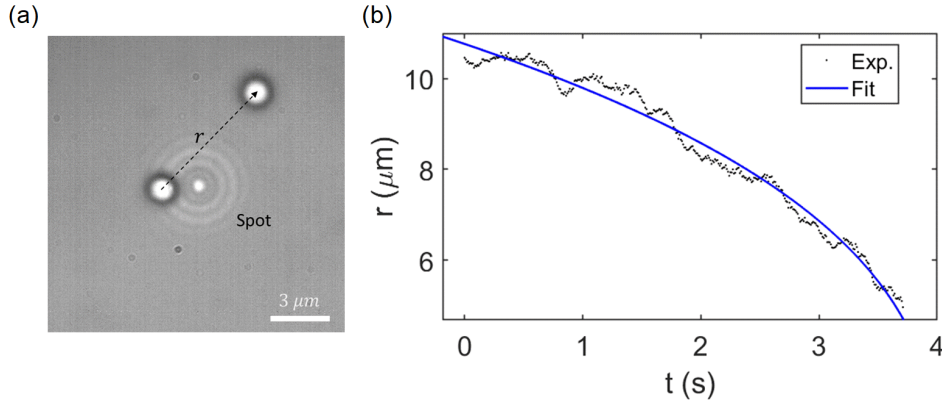
FIGURE 5.20: Soret coefficient calculation. (a) Snapshot of the motion of a PS AC under the influence of temperature distribution set up by a trapped and heated PS AC in a defocused laser spot. (b) Trajectory of the second colloid with respect to the trapped colloid $r(t)$ is fitted with equation 5.12.

The trajectory $r(t)$ of the second colloid undergoing thermophoretic motion with respect to the trapped one as shown in fig. 5.20 (a) is obtained by tracking their motion. The corresponding trajectory $r(t)$ is plotted in fig. 5.20 (b). Fitting it with equation (5.12) we obtain the fitting parameters $A = 1248.00 \ \mu\text{m}^3$ and $B = -308.20 \ \mu\text{m}^3\text{s}^{-1}$. Thus, the thermodiffusion coefficient is obtained as $D_T = \frac{B}{3\Delta T_0 a} = -16.01 \ \mu\text{m}^2\text{K}^{-1}\text{s}^{-1}$, where $\Delta T_0 = 9.80$ K and $2a = 1.31 \ \mu\text{m}$. The Soret coefficient can be obtained as $S_T = \frac{D_T}{D} = -115.16 \ \text{K}^{-1}$ ($D = 0.14 \ \mu\text{m}^2\text{s}^{-1}$). The negative sign implies the motion towards positive thermal gradient as in our experimental case.

5.8.2 Effect of buoyancy driven thermal convection

The generated thermal gradient due to heating of the trapped colloids can also lead to buoyancy driven convection in the surrounding regions. We have employed COMSOL 5.1 and combined the heat-transfer module with laminar flow module to enumerate the effect of buoyancy-driven convection for a single centrally trapped and heated PS AC, modelled using Maxwell-Garnett effective medium theory as explained in section 5.2.2. A 2D axisymmetric model depicts the geometry considered for the calculation as shown in fig. 5.21.The outer boundary layer was set to $T_0 = 298$ K. The colloid (PS AC) was defined as the heat source with the equation:

$$Q\left(r, z\right) = \frac{2P_0}{\pi w_0{}^2} \alpha e^{-\alpha z} e^{-2r^2/w_0{}^2} \tag{5.13}$$

where, P_0 is the incident laser power, $w_0 = 0.8 \ \mu\text{m}$ is beam waist and α is the absorption coefficient of the modelled particle at wavelength $\lambda = 532$ nm. Modelling the iron
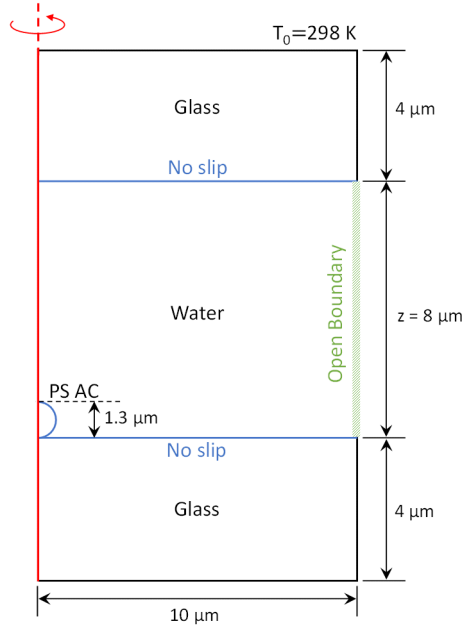
FIGURE 5.21: Schematic of the 2D axisymmetric geometry employed to calculate the temperature and the corresponding buoyancy driven convection

oxide infused colloid using Maxwell-Garnett effective medium theory (section 5.2.2) and calculating the refractive index as ($n = 1.6777 + i0.0169$), the absorption coefficient was calculated using the equation $\alpha = 4\pi n''/\lambda' = 5.3069 \cdot 10^5 \,\mathrm{m}^{-1}$, $\lambda' = \lambda/n_{\mathrm{med}}$, n'' denoting the imaginary part of the refractive index. A temperature dependent density $\rho(\mathrm{T})$, dynamic viscosity $\eta(\mathrm{T})$ as well as thermal conductivity $\kappa(\mathrm{T})$ of the water facilitates introduction of thermal convection. In addition, the following parameters are used.

Materials	$\kappa(\mathrm{Wm}^{-1}\mathrm{K}^{-1})$	$\rho(\mathrm{Kgm}^{-3})$	$\mathrm{C_p}(\mathrm{JKg}^{-1}\mathrm{K}^{-1})$
Glass	1.38	2203	703
Colloid	0.1861	1215	1070

TABLE 5.2: Parameters used for the simulations

Fig. 5.22 (a) shows the calculated temperature distribution. The temperature is more towards the central part of the colloid due to its lower thermal conductivity. However, experimental temperature only reflects the surface temperature. Fig. 5.22 (b) shows the corresponding temperature distribution along a line parallel to x axis at $z = 0.65 \,\mu$m, which shows decreasing trend from the central region. The surface temperature as a function of laser power is shown in fig. 5.22 (c) and matches reasonably well with the experimentally measured temperature. The relative density change is shown in fig. 5.22 (d).

To calculate the thermal convection, the upper and lower glass-water interfaces as well as the colloid water interface were set with no-slip boundary conditions and the boundary on right side as open boundary as shown in fig. 5.23. The resultant convective flow field and its
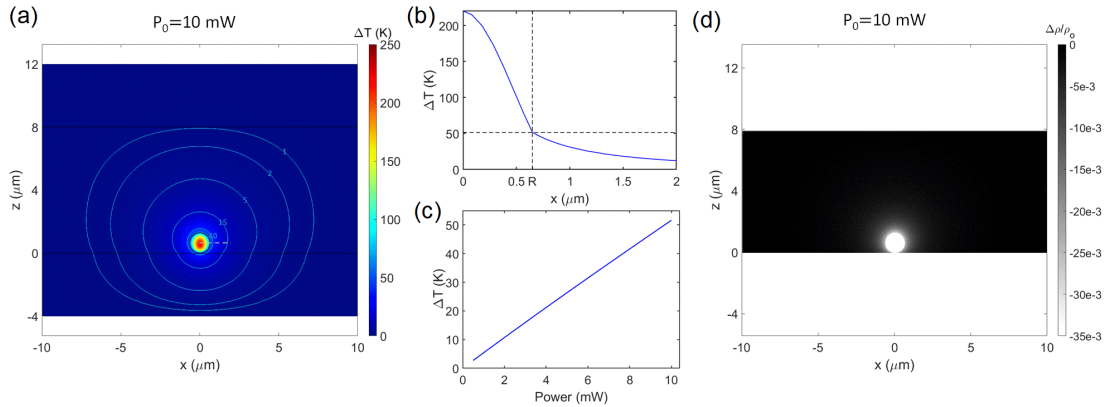
FIGURE 5.22: Simulated temperature distribution and density distribution considering thermal convection. (a) Temperature distribution in the xz plane (b) Temperature distribution along a line parallel to the x axis at $z = 0.65$ μm. (c) Temperature at the surface of the colloid as function of power shows increasing linear trend. (d) The relative density change in the xz plane.
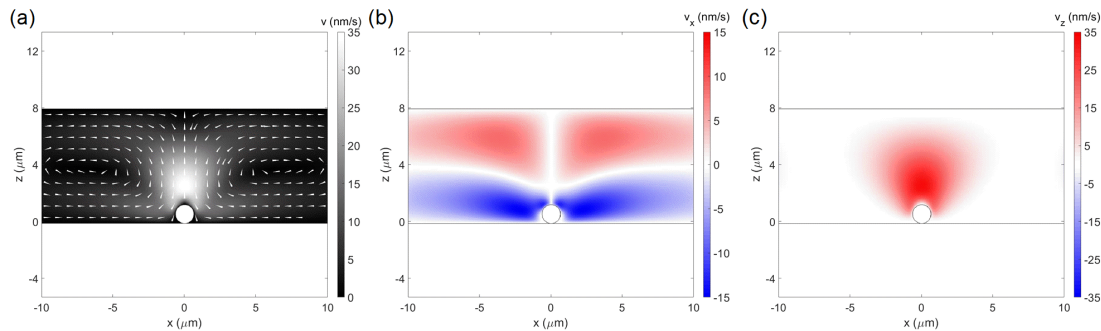
FIGURE 5.23: Simulated flow field due to thermal convection for a laser power of $P_0 = 10$ mW at xz plane. (a) Magnitude of the thermal flow field along with its direction (white arrow heads). The corresponding x and z component of the flow field is shown in (b) and (c) respectively.
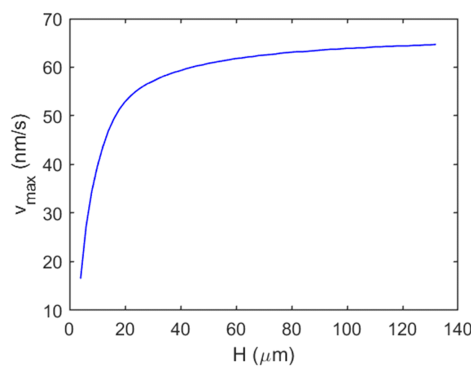
FIGURE 5.24: Simulated maximum convective velocity v_{max} at laser power $P_0 = 10$ mW as a function of chamber height H.

x and z components are shown in fig. 5.23. The calculated maximum flow velocity even for 10 mW excitation of a centrally heated colloid are in the range $\sim 10^1$ nm s^{-1}, which are two

orders of magnitude lower than the experimentally observed thermophoretic velocity. The calculated maximum velocity saturates at about $63 \, \text{nm s}^{-1}$ as the sample chamber height is increased to 120 μm as shown in fig. 5.24. Thus, the effect of thermal convection can be neglected compared to the thermophoretic velocity of the colloids.

5.8.3 Effect of scattering force and optical binding

Other than the effect of generated thermal gradient on the assembly process and their arrangement, we have also evaluated the effect of scattered light on neighbouring colloids and the resultant optical binding effect has been considered [153].

To evaluate the effect of optical binding we have used COMSOL 5.1 and employed a cuboidal geometry ($8 \, \mu\text{m} \times 8 \, \mu\text{m} \times 6 \, \mu\text{m}$) as shown in fig. 5.25 (a). A defocused Gaussian optical field at wavelength $\lambda = 532$ nm and with polarization along y direction was introduced using a port as shown by the green envelope and arrow. Iron oxide infused colloids were modelled as uniform spheres having diameter 1.3 with refractive index ($n = 1.6777 + i0.0169$) obtained by considering Maxwell-Garnett effective medium theory (see section 5.2.2). Scattering boundary conditions were applied to appropriate boundaries to avoid spurious reflections. The medium was modelled as homogeneous with refractive index set to that of water ($n_{\text{med}} = 1.33$). The entire geometry has been meshed using a minimum tetrahedral meshing size of ~ 150 nm.

The optical scattering force have been calculated by employing the Maxwell stress tensor formulation of the wave-optics module. A colloid was fixed at one position, and the scattering force on the particle was calculated as a function of position of the second moving colloid as shown in fig. 5.25 (a). Fig. 5.25(b) shows the numerically calculated optical
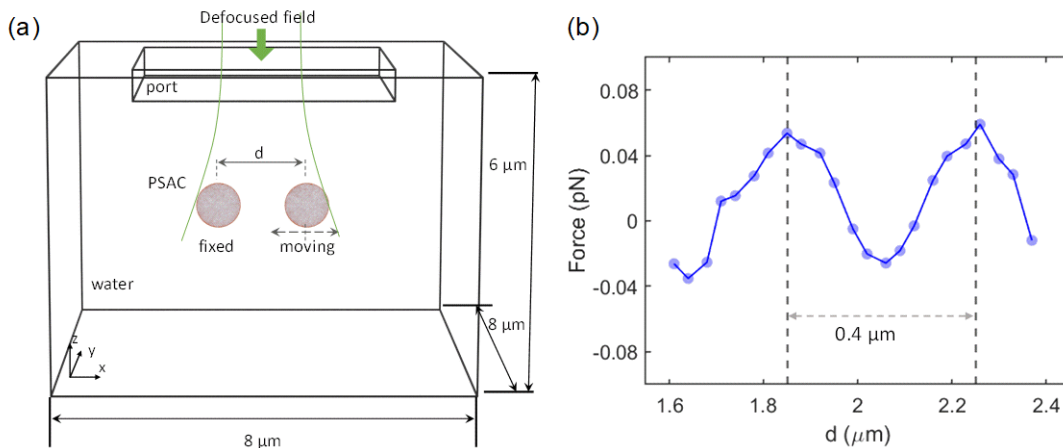
FIGURE 5.25: Numerical calculation of optical scattering force. (a) Schematic of the geometry employed for calculation of optical scattering force. (b) Evaluated optical scattering force using Maxwell stress tensor at the fixed particle as a function of position of the second moving particle.

scattering force. The force oscillates as function of position of the moving colloids with period $\lambda' = \lambda/n_{\mathrm{med}} = 400$ nm. The oscillations are characteristics of optical binding force and indicative of the scattering force on adjacent particles which are in the order of ~ 0.01 pN, one order smaller than the optical gradient force on the colloids, therefore, having a weaker effect on the assembly with respect to the gradient optical force. This represents the approximate scattering force on the colloids as implementation of strong focusing and resultant vectorial optical field is difficult to achieve in COMSOL.

5.9   Conclusion

To conclude, we have reported experimental investigation of optothermal interaction of active colloids in focused and defocused Gaussian optical field. The colloids undergo self-thermophoretic motion under the effect of asymmetric illumination of focused optical field. The self-thermophoretic effect and its laser power dependence has been investigated by considering temperature dependent thermo-diffusion coefficient (D_T) as well as Soret coefficient (S_T) of the colloid. In addition, the temperature distribution set due to a trapped and heated colloid serves as an environmental perturbation of freely diffusing PS ACs in the surrounding region and aid thermophoresis enabled long-range attraction and a short-range repulsion. In a defocused optical field, the colloids form an ordered assembly under the counteracting effect of optical gradient potential enabled attraction and short-range repulsion due to thermal gradient. The resultant colloidal matter self-evolves as a new active colloid joins the assembly. We further report input polarization state as a parameter for modulation of the self-thermophoretic motion of the ACs as well as structural orientation of the colloids in defocused laser spot. This observation is further understood by investigation of the focal electric field intensity distribution under such illumination configuration. In addition, the effect of optical scattering force and thermal convection has been investigated by employing FEM simulations. Through this method, the number of ACs in the colloidal matter can be modulated by changing the extent of laser defocusing. Thus, our study achieves dynamic assembly of active colloids in a simple defocused optical field.

The following table summarizes the results discussed in various sections of this chapter.

Section	Summary
5.2	In this section we have characterized the properties of the colloids and discussed the experimental configuration
5.3	Summary of temperature measurement techniques

5.4.1	Optical trapping of the colloids and power dependence of trap constant shows linear dependence with respect to incident laser power
5.4.2	Self-thermophoretic motion of the colloids due to self-heating of the colloids and investigation of power dependence of the dynamics
5.4.3	Polarization dependence of self-thermophoretic motion: the colloids moves along x direction of y polarized light and vice-versa for x polarized light
5.5	Themophoretic hovering of a colloid near a trapped PS AC due to temperature distribution set up by the trapped colloid
5.6.1	Spatial distribution of the defocused optical field, estimation
5.6.2	Dynamics of pair of PS AC in defocused illumination shows their arrangement along diametrically opposite position whose orientation can be modulated by input linear polarization state: they orient along x direction for y polarized optical field and vice-versa for x polarized field.
5.6.3	Experimental and numerical estimation of optical forces
5.7	The formation of colloidal matter self-evolves in the defocused optical field as a new colloid joins the assembly and it grows with time as well as extent of defocusing and laser power.
5.8.1	The Soret coefficient has been estimated by tracking the trajectory of an incoming PS AC.
5.8.2	The effect of Bouyancy driven thermal convection flow in the order of $\sim \mathrm{nm\,s^{-1}}$ have been considered for the assembly process
5.8.3	Though numerical calculation, we show that the optical binding force ~ 0.1 pN may play a role in the arrangement of the colloidal matter in the optical field.

The presented work, therefore investigate the optical and thermal interaction of self-heating iron oxide infused polystyrene colloids. In recent times, the optical tweezing of

metal particle doped colloids have led to diverse field of research from realizing microscopic engines to self-propelling colloids with laser steering [131, 133, 139]. In addition, laser multiplexing coupled with steering have led to feed-back controlled assembly [133]. However, we show that the thermal response these colloids can be utilized for assemble in a single defocused optical field. The self-evolution of this assembly without any external intervention has been depicted for the first time. The study can serve as a simple model system for understanding collective behavior at microscopic length scales in addition to realization of reconfigurable microscopic engines with multiple colloids.

Chapter 6

Orbital angular momentum driven collective motion of active colloids

Abstract:

This chapter discusses the self-organization and collective motion of polystyrene thermally active colloids driven by orbital energy flow of Laguerre-Gaussian beams. Specifically, we harness the self-heating and thermophoretic nature of the iron oxide infused polystyrene colloids to investigate the optothermal interactions of colloids undergoing orbital motion in the illuminated optical field. The results indicate that the colloids undergo long-range attractive motion towards a trapped and heated colloid and a short-range repulsive interaction between two equally heated colloids in the optical field. This leads to self-evolution of the structure as a new colloid joins the assembly and consequently the characteristics of the orbital angular momentum driven collective motion of the entire structure undergoes modifications. The results have been further investigated by studying their dynamics with respect to increasing laser power as well as introducing a passive dielectric colloid in the assembly, therefore, by modulation of the optothermal interactions.

6.1   Introduction and motivation

Living organisms of different length scales such as colonies of bacteria [135, 136], flocks of birds [137], schools of fish [154] often undergo collective motion [138] under the influence of external environmental cues such as boundaries, nutrients, predators etc. These systems, termed as living active matter, have opened up a vast swathe of studies related to their collective dynamics, pattern formation, non-equilibrium thermodynamics as well as provide a test bed for many biophysical phenomena [138, 155, 156]. It is desirable to study these systems in much more controlled manner and replicate the systems.

In this context, in recent times, similar behaving systems have been envisaged through optical trapping and manipulation of artificial active colloids of microscopic dimensions. These systems not only provide a path for experimental realisation of active matter dynamics

but also allows modulation through various means to investigate emergent behaviours such as clustering, pattern formation, self-interactions [131–133, 140, 141]. At the core, most of these studies harness light-matter interactions due to a focused or defocused optical field at the particle-environment interface to facilitate optical forces as well as localized heating for trapping and manipulation of self-thermophoretic colloids. These systems absorb energy from the surrounding medium to self-propel, and can undergo collective motion as a whole, mimicking dynamic pattern formation[133], swarming and vortex formation [132, 157] as well as sensing, self-learning when coupled with a feedback mechanism [131, 158, 159]. The driving mechanism behind such studies have been realized by defocused illumination of active colloids in a critical mixture [132] as well as via laser beam multiplexing and steering with feedback loop [131, 133].

An alternative approach for driving the dynamics of the colloids can be facilitated by scattering forces due to the interaction of angular momentum carrying beams with the colloids [19, 50–52, 160]. Manipulation of colloids through such methods utilizes optical holography where optical intensity, phase as well as polarization states are modulated to manipulate and form desired assemblies [49, 65, 66, 161]. Specifically, phase modulation has enabled generation of optical fields possessing orbital angular momentum (OAM) due to their helical wave fronts and consequent transverse energy flow due to orbital constituent, termed as orbital energy flow [47]. As a result, colloidal objects trapped in a beam possessing OAM undergo orbital motion due to the scattering force facilitated by the orbital energy flow component [49, 50]. To this end, such angular momentum driven systems have been studied to investigate hydrodynamic as well as non-equilibrium interaction between colloidal particles [162–164].

Motivated by this, in this report we investigate the collective dynamics of iron oxide infused (Fe_2O_3/Fe_3O_4) polystyrene thermally active colloid (PS AC) due to the orbital flow of an illuminated Laguerre Gaussian (LG_m^l, l is azimuthal order, m is radial order) beam. The transverse orbital energy flow of the incident LG beam leads to scattering force facilitated orbital motion of the colloids in the optical field. In addition, the iron oxide doping leads to heating of the colloids due to absorption of the laser intensity and consequent temperature distribution in the surrounding region. As a result, colloids in the vicinity undergo thermophoretic motion towards the heat center as shown in the schematic in fig. 6.1 (a). Eventually, the colloids get trapped in the optical field due to optical gradient force and experience mutual thermal repulsion due to their equal temperature in the optical trap. Such thermophoresis enabled long-range attraction and short-range repulsion have already been discussed in our previous work [121] as well as chapter 5. Finally, the counteractive effects of attractive and repulsive force in addition to the optical trap leads to collective motion of the colloids due to scattering forces induced by the orbital energy flow of the beam. The
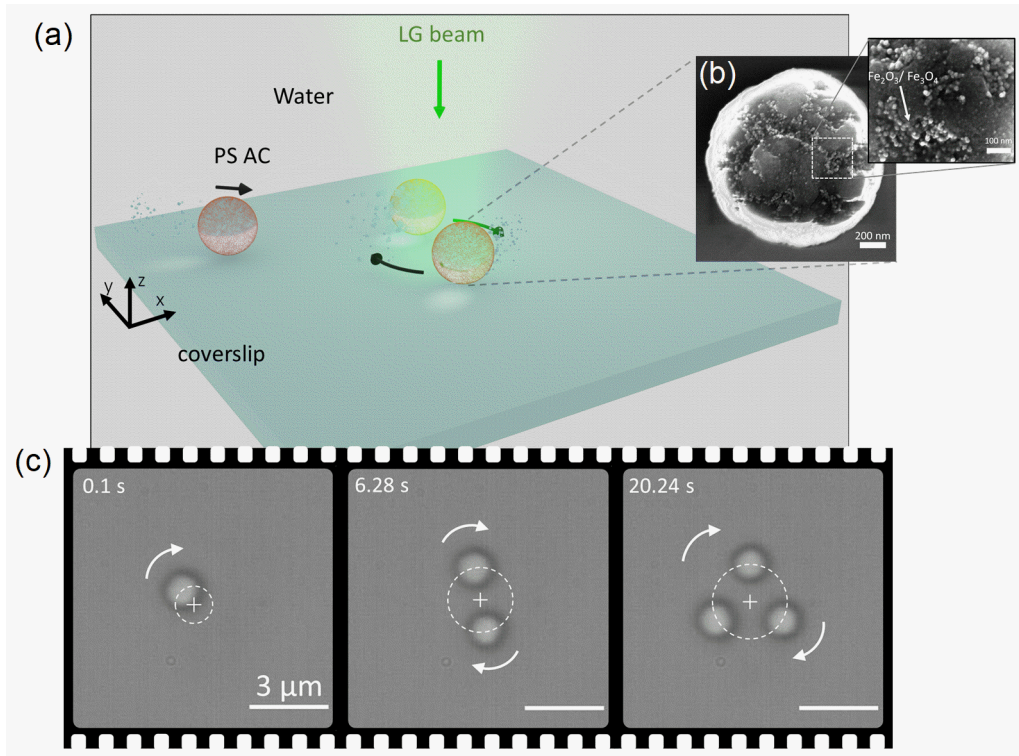
FIGURE 6.1: Collective motion of optothermally assembled reconfigurable colloidal matter. (a) Schematic of assembly and collective motion of polystyrene thermally active colloids (PS ACs) due to the orbital energy flow of incident LG_0^3 beam at wavelength $\lambda = 532$ nm. (b) Scanning electron micrograph of a PS AC shows the embedded $Fe_2O_3/Fe_3O_4 \sim 15$ nm nanoparticles with $\sim 30\%$ mass fraction. (c) Timeseries of the assembly and rotation of the formed colloidal matter.

characteristics of the arrangement of the colloids in optical fields as well as their collective motion changes as the assembly grows - the angular velocity of rotational motion decreases as the assembly grows from one to three colloids, as shown in fig. 6.1 (c). In comparison to the PS ACs, the orbital motion of system of dielectric polystyrene colloids of 1.01 μm diameter increase with number of colloids, and is discussed in section 6.4.

Before we discuss the characteristics of the collective motion and analyze the data, we will describe the experimental implementation as well as the properties of the colloids.

6.2 Experimental implementation and properties of the colloid

The colloids used in the experiments have diameter ~ 1.31 μm and are composed of polystyrene doped with nanoparticulate (dimaeter 15 nm) iron oxide (Fe_2O_3/Fe_3O_4) distributed throughout the volume of the colloid with mass fraction $\sim 30\%$ (microparticles GmbH) as shown

in fig. 6.1 (b). As a consequence of the iron oxide doping, the colloid heats up upon absorption of the incident laser beam, which can lead to self-thermophoretic motion due to asymmetric heating [121], rendering their active nature. In addition, the doping also facilitates higher scattering forces due to the incident optical beam compared to an un-doped dielectric colloid. The effective material properties of the iron oxide doped colloid can be modeled using Maxwell-Garnett effective medium theory which results in a refractive index $n = 1.6777 + i0.0169$. as described in section 5.2.2 of chapter 5 [145, 146].

The sample consists of a micro chamber (height $\sim 100\,\mu$m) enclosed with two glass coverslips containing a dilute solution of these polystyrene thermally active colloids (PS ACs) dispersed in deionized water. The sample is placed on a piezo stage and illuminated with LG_0^3 beam at wavelength $\lambda = 532$ nm using a 100×0.95 objective lens with the help of the top channel of a dual-channel optical microscope as discussed in the section 5.2 of chapter 5. The LG_0^3 beam is prepared through projection of a Gaussian beam to a fork diffraction pattern of desired order by employing a off-axis spatial light modulator, as described in section 2.1 of chapter 2. The continuous power variation is performed using a half-wave plate and a polarizing beam splitter as discussed in chapter 5 section 5.2. The signal is collected from the lower channel of the dual channel microscope, using a 100×1.49 NA objective lens and then projected to a fast camera (100 -1000 fps), with the excitation wavelength rejected by combination of notch and edge filters. The extraction of the trajectories of the colloidal particles from the recorded image sequence are performed by employing Trackmate [144].

In absence of any external perturbation, the colloids undergo unbiased Brownian motion, the diffusion of which can be calculated by tracking their position and calculating the mean-square displacement (MSD). The diffusion coefficient for the free diffusing PS AC is $D = 0.14\,\mu$m^{2}s^{-1}, which is lower than their bulk value $D_0 = 0.33\,\mu$m^{2}s^{-1}. The lower value can be attributed to their proximity to the glass surface as described in section 5.2.3 of chapter 5.

In the following section we discuss the assembly process as well as the collective dynamics of the colloids driven by the LG_0^3 beam.

6.3 Dynamics of PS ACs due to LG_0^3 beam excitation

Under the influence of the incident optical field an optically trapped the colloid undergoes rotational motion due to the scattering force exerted by the transverse orbital energy flow of LG_0^3 beam (see equation 1.3). In addition, the generated temperature distribution leads to thermophoretic motion of the colloids in the vicinity and consequent assembly.

Fig. 6.2 describes the entire assembly and collective motion of the colloids at laser power $P_0 = 6.5$ mW. A trapped single colloid undergoes orbital rotation under the influence
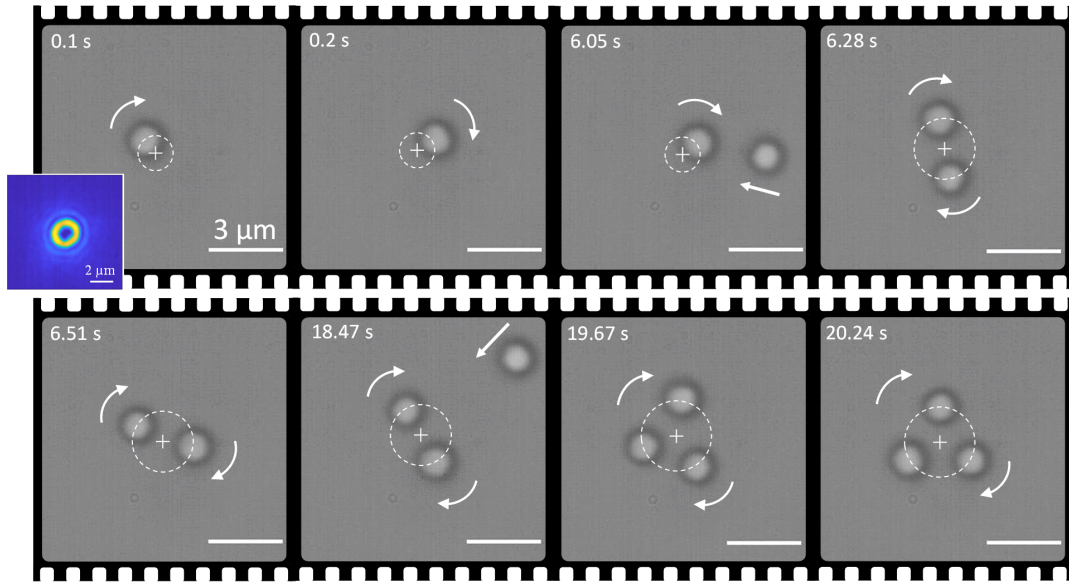
FIGURE 6.2: Time series of assembly and collective motion of the colloidal matter. A single PS AC gets trapped int he incident LG_0^3 beam as shown in the inset and undergoes orbital motion indicated by the white arrow. The resultant optical heating leads to thermophoretic motion of surrounding PS ACs towards the heat center and formation of colloidal matter due to short-range inter-particle thermal repulsion of equally heated colloids. In addition, the colloids undergo collective motion owing to the scattering force imparted due to the orbital energy flow of the incident LG_0^3 beam.

of the transverse orbital energy flow of the incident LG_0^3 beam as shown in the inset. The optical field also leads to heating of the trapped and rotating PS ACs, which facilitates an environmental cue for surrounding freely diffusing PS ACs. As a consequence, surrounding PS ACs undergo thermophoretic motion towards the heat center. The thermophoretic motion ($v = -D_T \nabla T$, D_T is thermo-diffusion coefficient and T is the temperature) can be characterized by its negative Soret coefficient ($S_T = D_T/D_0$) and has been discussed in section 5.8.1 of chapter 5. As a result, an incoming PS AC gets trapped in the optical field and undergoes orbital motion in the optical field as shown in fig. 6.2. It is interesting to note that the two colloids always keep diametrically opposite positions with respect to each other, while undergoing collective orbital motion. Similarly, for three colloids, they form a triangular colloidal matter, and rotate collectively, being approximately equidistant from each other. Such formation of colloidal matter and its mechanism in a defocused optical Gaussian beam has already been discussed in the previous chapter [121]. In this report, we investigate the collective rotational motion of the active colloidal matter under the influence of transverse orbital energy flow of the LG_0^3 beam. In the following section, we analyze the collective motion of the colloids and quantify the parameters.

6.3.1   Analysis of the collective motion

The analysis of the collective dynamics of the assembly of colloids can be performed by investigating their position distribution. Fig 6.3 (a) shows the average position distribution of the colloidal assembly as it undergoes orbital motion at laser power $P_0 = 6.5$ mW. Inset shows the corresponding assembly. As stated before, the mechanism relies on trapping as well heating of the colloids in the focused LG_0^3 optical field. The corresponding radial optical potential can be computed by analyzing the trajectory of rotating single colloid. Fig. 6.3 (b) shows the histogram of the radial position distribution and corresponding radial optical potential (U_r) in units of k_BT, where k_B is the Boltzmann constant. The radial trapping stiffness (k_r) can be obtained by considering equipartition theorem [52], and fitting the obtained potential with $\frac{1}{2}k_r r^2$. At laser power $P_0 = 6.5$ mW, the obtained trapping stiffness comes out to be $k_r = 3.22 \cdot 10^{-7}$ N/m. This indicates that the colloid experiences a radial optical gradient force in the order $F_r \approx 0.1$-1 pN. The radius at which the colloid undergoes orbital motion changes increases in case of collective motion of two and three
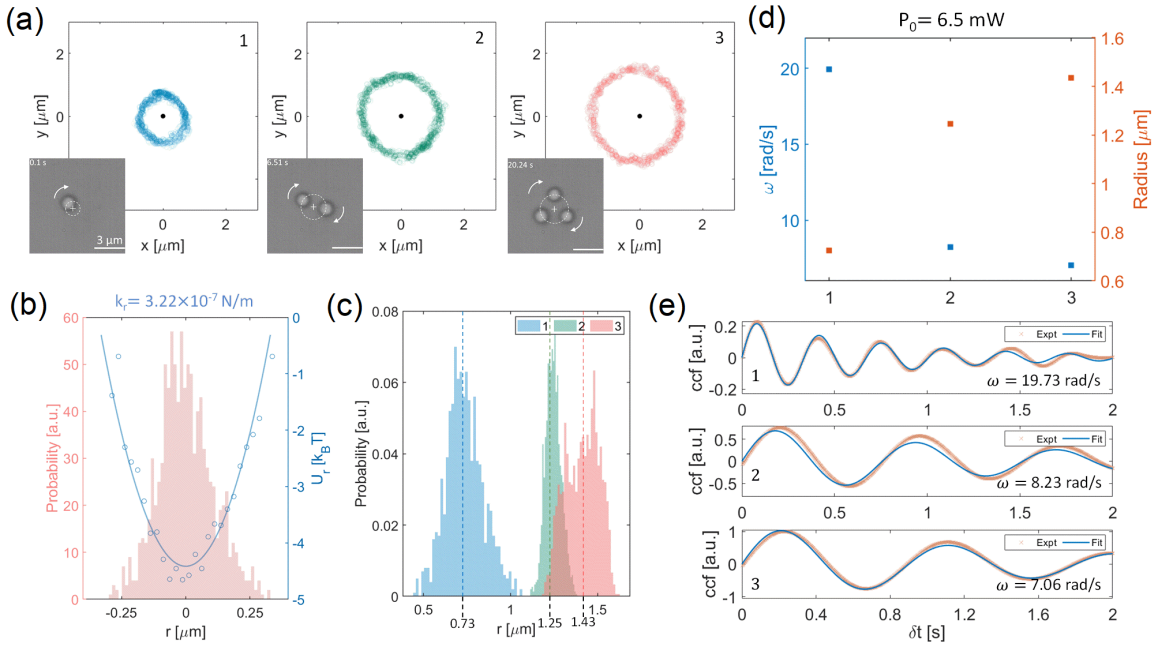
FIGURE 6.3: Analysis of collective motion of the colloidal matter. (a) The position distribution of the rotating colloidal matter consisting 1 to 3 PS ACs. Inset shows the corresponding snapshot of the assembly. (b) Analysis of the radial position distribution for a single PS AC leads to estimation of radial trapping potential with trapping stiffness $k_r = 0.322\,\mathrm{pN}/\mu\mathrm{m}$ at laser power $P_0 = 6.5\,\mathrm{mW}$. (c) The inter-particle thermal repulsion of equally heated PS ACs leads to higher radius of rotation for colloidal matter consisting 2 and 3 PS ACs shown by the histogram with average radius $r = 0.73\,\mu\mathrm{m}$ for 1 PS AC, $r = 1.25\,\mu\mathrm{m}$ for 2 PS ACs and $r = 1.43\,\mu\mathrm{m}$ for 3 PS ACs. (d) The thermal repulsion leads to decrease of of the average angular velocity of rotation with increase in number of colloids in the colloidal matter. (e) The angular velocities have been extracted through calculation of cross correlation function

colloids as shown in fig. 6.3 (c).

This can be attributed to their thermal repulsion, since multiple colloids when heated to the same extent exhibit short range (up to 1 to 5 μm) repulsive behavior (see section 5.5 of chapter 5). Considering their thermophoretic behavior quantified by equation $v = -D_T \nabla T$, two colloids heated to equal extent, experience a negative temperature gradient when they come close. This repulsion also leads to decreasing of the collective angular velocity (ω) as the number of colloids increase as shown in fig. 6.3 (d). The corresponding average angular velocity can be extracted by calculating cross correlation function ($ccf(\delta t)$) of the corresponding trajectories ($x(t), y(t)$) through,

$$ccf(\delta t) = \langle x(t)y(t + \delta t)\rangle = \frac{k_B T}{k} e^{-k\delta t/\gamma} \sin(\omega \delta t) \qquad (6.1)$$

where, δt is the lag time, $\gamma = 6\pi a \eta$ is the friction coefficient of a colloid having radius a in a fluid having bulk viscous coefficient η and k is the trapping stiffness. The angular velocity at laser power $P_0 = 6.5$ mW decreases drastically from 19.93 rad/s for single PS AC to 8.23 rad/s for two colloids and decreases further to 7.02 rad/s for three PS ACs, as shown in fig. 6.3 (e). The slowing down can be attributed to their thermal repulsion as well as the colloids experiencing lower orbital angular momentum flux due and hence optical torque due to increasing radius of two and tree PS AC systems.

To further quantify the orbital motion, the azimuthal force acting on a single PS AC is calculated by analyzing its motion. The azimuthal force (F_ϕ) is given by $F_\phi = \gamma v_\phi$, where γ is the dynamic viscosity corrected with respect to the colloids proximity to the surface (see section 5.2.3 of chapter 5) and $v_\phi = r\omega$, is the tangential velocity of the colloid undergoing orbital motion at radius r with angular velocity ω. For a single colloid rotating at radius $r = 0.73$ μm and $\omega = 19.93$ rad/s, the azimuthal force acting on the colloid is approximately, $F_\phi \approx 0.309$ pN. Similarly, for two PS AC system the value turns out to be $F_\phi \approx 0.219$ pN and and for three PS AC system the values is $F_\phi \approx 0.215$ pN. In addition, the time averaged torque ($\langle\tau\rangle$) acting a single PS AC colloid can also be calculated. The rotational motion of a colloid about the z axis with a constant angular velocity $\mathbf{\Omega} = \omega\hat{\mathbf{z}}$ results from a balance between the torque applied to the sphere and the drag torque: $\tau_{\mathbf{drag}} = \mathbf{r} \times \mathbf{F_{drag}}$. Therefore, the time averaged torque can be calculated as, $\langle\tau\rangle = \gamma\langle\mathbf{r} \times (\mathbf{r} \times \mathbf{\Omega})\rangle = \gamma\omega\langle r^2\rangle$. For the rotation of a single PS AC, the torque comes out to be $\tau = 4.566 \cdot 10^{-20}$ N m. In comparison, the incident LG_0^3 beam carries an flux of OAM $\tau_{OAM} = lP_0/f = 4.61 \cdot 10^{-17}$ N m, where $l = 3$ is the azimuthal order, $P_0 = 6.5$ mW is the power and f is the frequency of light. Therefore, approximately 1% of the incident OAM flux is transferred onto the PS AC. It must be noted that the exact values of angular velocities as well as their radius depends on individual colloids, their morphology, as well as mass fraction of iron oxide doping.

6.3.2   Numerical calculation of optical forces

To corroborate the order of magnitude of the experimentally determined forces, we have used COMSOL 5.1 to calculate forces on a single colloid. A cuboidal geometry ($8\,\mu m \times 8\,\mu m \times 6\,\mu m$) have been employed for the study as shown in fig. 6.4 (a). A LG_0^3 beam at wavelength 532 nm with polarization along y axis and power $P_0 = 10$ mW was incident onto the system through a port as shown by the maroon arrow. The approximate focusing conditions were matched with the experimental case by setting $w_0 = 0.8\,\mu m$, although exact strong focusing conditions are difficult to achieve in COMSOL. The colloid was modeled using Maxwell-Garnett effective medium theory (see section 5.2.2 of chapter 5) [145], which results in an effective refractive index $n = 1.6777 + i0.0169$. The surrounding medium is set as a homogeneous medium with refractive index set to that of water for simplicity. The entire geometry is meshed using a minimum tetrahedral meshing size of ~ 150 nm. Scattering boundary conditions are applied on the appropriate surfaces to avoid spurious reflections.

The PS AC was scanned across the xy plane from $-2.2\,\mu m$ to $+2.2\,\mu m$ in both x and y direction in 20 steps and the force on the colloid at each position is calculated by Maxwell-stress tensor formulation of the wave-optics module. Fig. 6.4 (b) shows the obtained radial force profile and the black arrows depict the sense of the in plane force components (F_x,F_y). Inset shows the corresponding beam profile with superimposed black arrows indicating the transverse orbital energy flow of the beam. The approximate radius of trapping is at $r \approx 0.6\,\mu m$ and shown by the green dotted circle. The obtained radial optical force of the order $F_r \sim 0.1\text{-}1$ pN matches well with the order of magnitude of the experimentally obtained
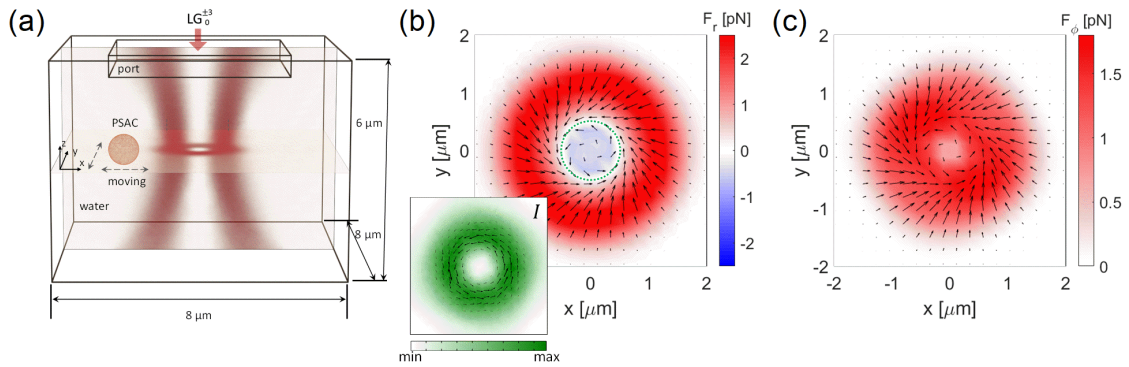
FIGURE 6.4: Numerical calculation of optical force. (a) Schematic of the geometry employed for numerical calculation of optical forces. (b) Calculated radial optical force (F_r) with black arrows indicating the sense of the in plane force components (F_x, F_y). Inset shows the corresponding focal optical field profile along with arrows showing the sense of orbital energy flow. (c) Calculated azimuthal force component (F_ϕ) with black arrows indicating the sense of the in plane force components (F_x, F_y).

value of trap stiffness. Fig. 6.4 (c) shows the corresponding azimuthal force (F_ϕ) along with the black arrows depicting in plane force sense. The order of magnitude of the F_ϕ are similar to that of the experimentally measured value.

The collective motion described in this section is reminiscent of many biological active matters as well as of fundamental importance due to their synchronization through environmental cues such as thermal gradient. Before we proceed to discuss the temperature distribution of the system of PS ACs, it is useful to investigate the motion of passive dielectric polystyrene colloids under the influence of LG_0^3 beams and characterize the differences.

6.4   Dynamics of passive dielectric colloids

The large optical field due to focusing of the LG_0^3 beam can facilitate optical trapping of passive dielectric polystyrene colloids of diameter 1.01 μm. Subsequently, the colloid undergoes orbital motion as depicted in fig. 6.5 (a) for incident power $P_0 = 6.5$ mW. The corresponding beam intensity profile is shown in the inset. Similarly, multiple colloids can be optically trapped and can undergo orbital motion under the influence of the scattering force imparted due to the orbital energy flow of the LG_0^3 beam. Their rotational motion can be analyzed by calculating the cross-correlation function (ccf) and extracting the corresponding angular velocity (ω). The extracted angular velocity values are shown in fig. 6.5 (b). It can be seen that the angular velocity increases as the number of particles increase in the LG_0^3 beam trap in contrast to the collective motion of the PS ACs, as discussed in
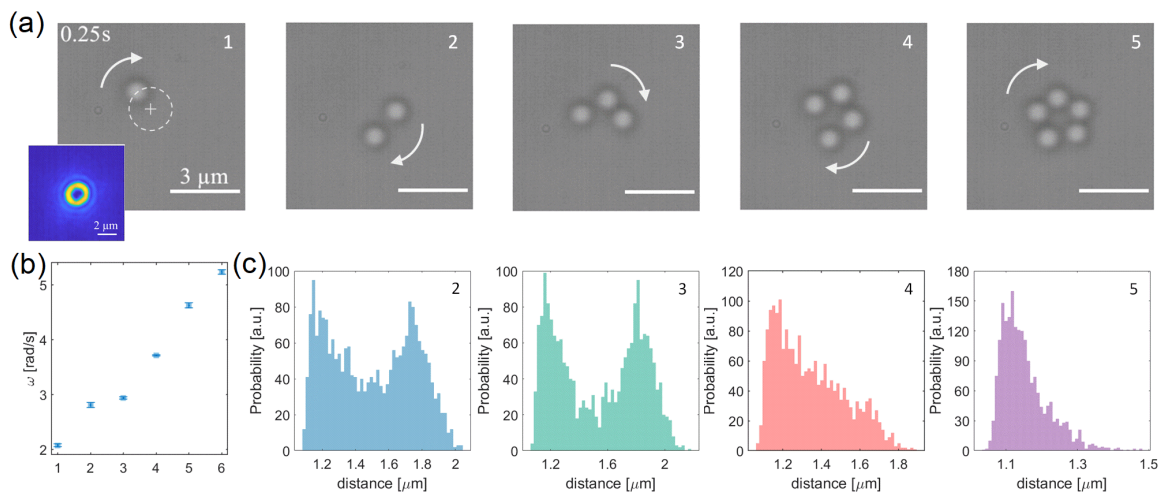
FIGURE 6.5: Investigation of dynamics of passive dielectric colloids. (a) Optical trapping and rotational motion of passive dielectric polystyrene 1.01 μm colloids in incident LG_0^3 beam. The optical beam profile is shown in the inset. White arrows indicate the sense of the orbital motion. (b) The angular velocity increases with number of colloids in the trap. (c) Histogram of corresponding average inter-particle distance when there is 2-5 colloids in the trap.

the previous section. This increase can be attributed to the hydrodynamic interactions between the identical colloids, i.e., a trailing colloid travels in the wake created by the leading colloid and is dependent on their separation [162, 164]. This is investigated by calculating the corresponding histogram for the inter-particle distances for 2-5 colloids, shown in fig. 6.5 (c). The extracted histogram indicates that for 2-3 colloids, the orbiting colloids can be either very close to each other, or further away from each other, resulting in two peaks in the histogram. Therefore, similar hydrodynamic interaction results in close values of the ω shown in fig. 6.5 (b). On the other hand, sharper probability distribution for the inter-particle distance for 4-5 colloid systems results in their higher angular velocities. Such interactions are enabled by the close packing of the passive polystyrene colloids, in contrast to the case with PS ACs.

Examples of hydrodynamics interaction mediated collective motion have been widely reported in the literature. For example, Sokolov et al. [162] reported spontaneous pairing of two colloids when they are driven around a ring by an optical vortex beam. The mechanism relies on symmetry breaking of the hydrodynamic coupling through the curvature of the path due to orbital flow of incident LG beam. Similar collective motion of multiple colloids have also been reported by Tsuji et al. [164], where the authors report increase of angular velocity of LG beam driven colloids with increase of number of colloids and consequent decrease of inter-particle distance.

Since the collective motion of the PS ACs rely on their optothermal heating, in the following section we look at the experimental estimation of the temperature increment due to optical heating as well as the temperature distribution in the surrounding region.

6.5   Estimation of temperature increment and temperature distribution

The iron oxide nanoparticle doped trapped PS ACs acts as a microscopic heat source upon absorption of the incident beam. The maximum surface temperature attained by the colloid in such cases can be calculated by studying the nematic to isotropic phase transition of 5CB liquid crystal (phase transition temperature $T_{pt} = 35°C = 308\,K$), as described in section 5.3 of chapter 5. Fig. 6.6 (a) shows the nematic to isotropic transition of liquid crystal around centrally heated immobile PS AC at laser power $P_0 = 3.88$ mW. The position of the PS AC with respect to the LG_0^3 beam is shown in the inset. The measured maximum surface temperature on the colloid increases linearly with respect to the incident laser power as shown in fig. 6.6 (b), fitted with linear equation $\Delta T\,[K] = 2.01\,P_0\,[mW] - 0.41$.
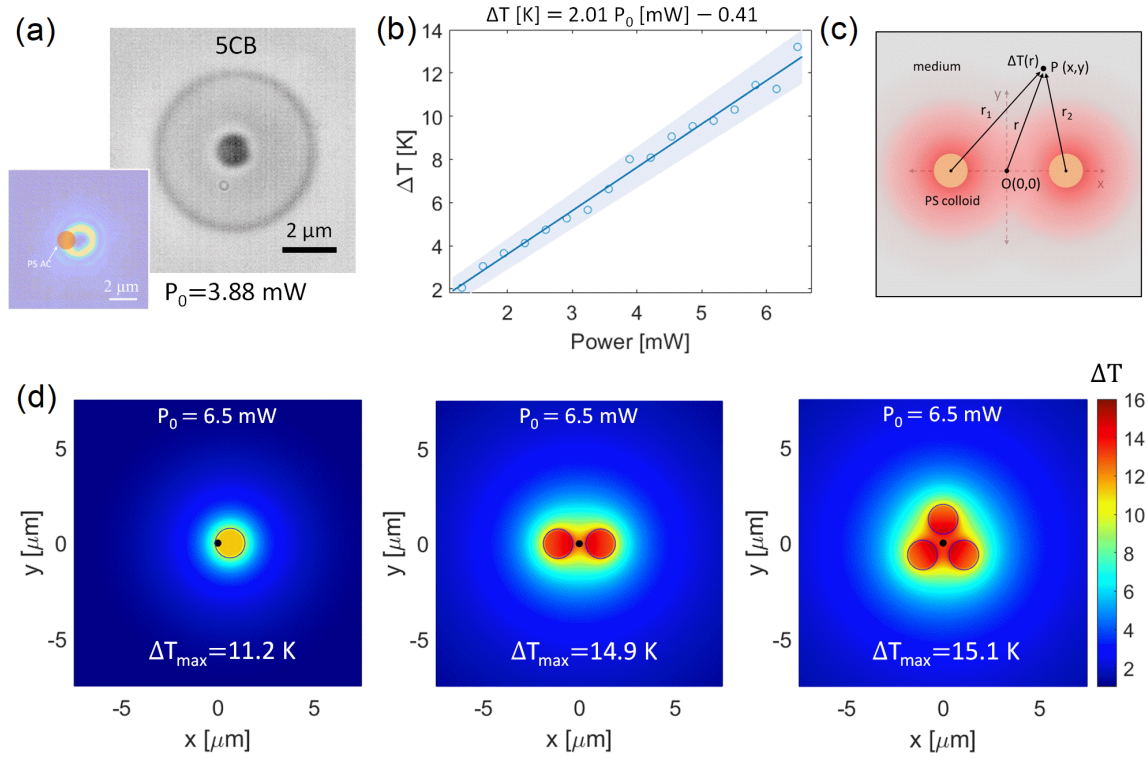
FIGURE 6.6: Estimation of surface temperature of PS AC and corresponding temperature distribution. (a) Bright-field optical image of 5CB liquid crystal phase transition from nematic to isotropic around a heated immobilised PS AC with a LG_0^3 beam at power $P_0 = 3.88$ mW. The position of the colloid with respect to the beam profile is indicated in the inset. (b) The measured maximum surface temperature of the colloids varies linearly with laser power. (c) Schematic for calculation of temperature distribution in the xy plane due to two equally heated colloids. (d) Estimated temperature distribution in the xy plane for assembly of 1-3 PS ACs at laser power $P_0 = 6.5$ mW.

To estimate the maximum, we assumed uniform temperature increment (T_0) on the surface of the heated colloid. The temperature distribution in the surrounding region (xy plane) can be obtained by [40]:

$$\Delta T(r) = \begin{cases} T_0 \dfrac{a}{r}, & \text{for } r \geq a. \\ T_0, & \text{for } r \leq a. \end{cases} \tag{6.2}$$

where, r is distance from the heated colloid center as shown in the schematic fig. 6.6 (c). This approach can be extrapolated for determining the temperature distribution in the surrounding region for multiple heated colloids through the equation, $\Delta T(r) = \sum_n \Delta T_n(r_n)$. Here, the subscript n denotes the nth heated colloid in the assembly and $\Delta T_n(r_n)$ is the temperature distribution sets up by the nth PS AC.

Fig. 6.6 (d) shows the corresponding temperature distribution for 1 to 3 PS ACs at laser power $P_0 = 6.5$ mW, with average inter-particle distance and radius extracted from

the experimentally measured dynamics of the assembly (see fig. 6.3). The temperature increment is calculated by considering $\Delta T^{\text{est}} = \Delta T^{\text{exp}} e^{-\delta x^2/2w_0^2}$, δx is the distance from the ring shaped region of the beam, $w_0 = 0.8 \, \mu$m is beam width, ΔT^{exp} is the experimentally measured temperature of an immobile centrally heated colloid in the configuration as shown in the inset of fig. 6.6 (a). The maximum temperature of the system increases from one PS AC to three PS ACs, leading to higher thermal repulsion and therefore, resulting in slower collective angular velocity as described in section 6.3.1.

To further investigate the effect of thermal repulsion, in the following section we look at dynamics of binary mixture of polystyrene 1.01 μm passive colloids and 1.31 μm PS ACs under the influence of focused LG_0^3 beam.

6.6   Dynamics of binary colloidal mixture: thermally active and passive colloids

To further investigate the effect of thermal repulsion on the angular velocity of the system, we investigate a system of PS ACs (brown disks) and passive polystyrene (PS) dielectric spheres having diameter 1.01 μm (blue disks). At laser power $\text{P}_0 = 6.5$ mW, a single PS AC colloid undergoes orbital motion and its angular velocity is extracted by calculating the corresponding cross correlation function, resulting in obtaining angular velocity, $\omega = 15.2$ rad/s, shown in fig. 6.7 (a). In comparison, a system of a single PS AC and a passive PS colloid undergo collective motion with angular velocity $\omega = 8.4$ rad/s. In this case, collective motion is slower than a single PS AC since the passive PS is much slower moving species than the PS AC. In addition, the thermophoretic response of the passive PS may also contribute to lower angular velocities. The corresponding histogram of the inter-particle distance shows maximum probability at distance $d_{12} \approx 1.51 \, \mu$m. In contrast, collective motion of two PS ACs undergo orbital motion with significantly slower angular velocity $\omega = 5.5$ rad/s as shown in fig. 6.7 (c). The average inter-particle distance is $d_{12} \approx 2.62 \, \mu$m and is much higher with respect to the case shown in fig. 6.7 (b), owing to their thermal repulsion. Addition of a passive PS onto the system of two PS ACs renders angular velocity $\omega = 4.5$ rad/s of the system of colloids, slower with respect to two PS ACs, as shown in fig. 6.7 (d). It can be attributed to the slower moving passive PS colloid as well as its thermophoretic response to the heated PS ACs. The inter-particle distances between the PS ACs and the passive PS shown in fig. 6.7 (d) has an average of $d_{13} = 1.82 \, \mu$m and $d_{23} = 1.68 \, \mu$m, and depicts that the passive PS roughly stays in between the PS ACs. Replacing the passive PS with another PS AC renders formation of triangular colloidal matter and much slower angular velocity, $\omega = 2.9$ rad/s. The average inter-particle distance is shown by the histogram with average $d = 2.60 \, \mu$m. It must be noted that the PS ACs in the

sample chamber trapped for the study were kept of similar size for consistency. Therefore, the results depict that thermal repulsion between the PS ACs have a stronger effect on the slower angular velocity of the formed colloidal matter than a slower moving passive PS.

Since optothermal heating of the colloids plays the key role in their collective orbital motion, in the following section we investigate their behavior with increasing laser power, which leads to higher heating as well as increasing incident orbital energy flow. Through the competitive action of the azimuthal force as well as the thermal repulsion we also investigate how the colloidal structure self-evolves while undergoing orbital motion through this process.
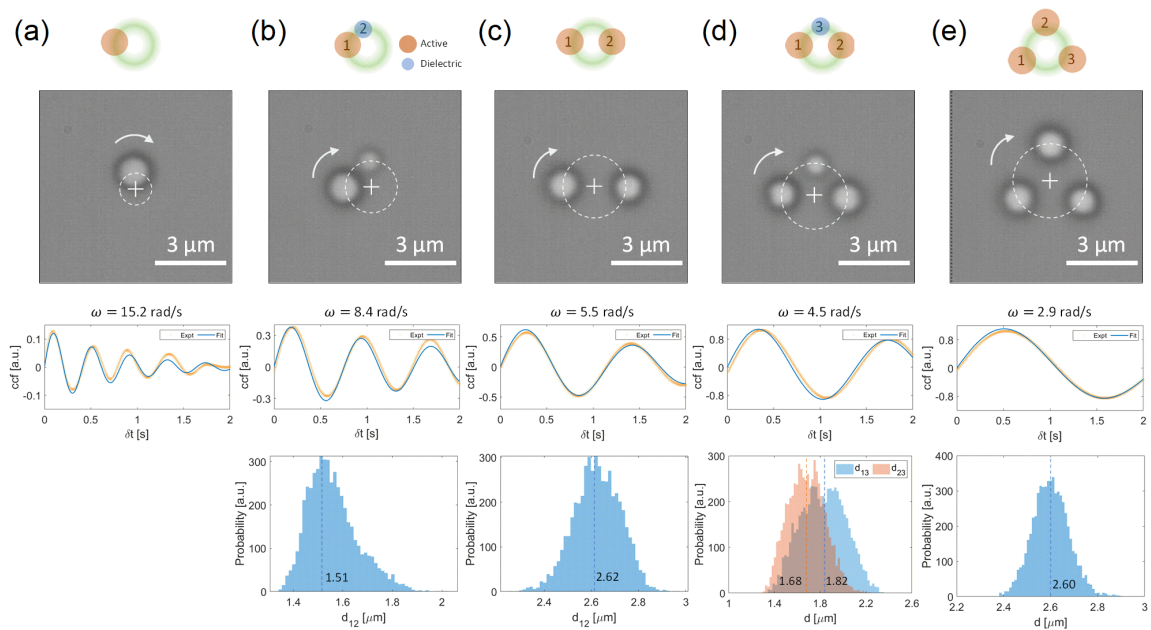
FIGURE 6.7: Investigation of dynamics of binary active-passive system. (a) A single PS AC in an incident LG_0^3 beam at laser power $P_0 = 6.5$ mW undergoes orbital motion with angular velocity $\omega = 15.2$ rad/s. (b) In comparison, the system consisting a PS AC and a passive PS undergoes rotation with angular velocity $\omega = 8.4$ rad/s. The corresponding inter-particle distance peaks around $d_{12} = 1.51$ μm. (c) The thermal repulsion between two PS ACs lead to significantly slower angular velocity $\omega = 5.5$ rad/s as well as higher average inter-particle distance $d_{12} = 2.62$ μm. (d) Introduction of a passive PS into the system of 2 PS ACs lead to slowing down of the system with average angular velocity $\omega = 4.5$ rad/s with average distance between the PS ACs and PS being $d_{13} = 1.68$ μm and $d_{23} = 1.82$ μm. (e) In comparison, an assembly of three PS ACs rotate with much slower angular velocity $\omega = 2.9$ rad/s and average inter-particle distance $d = 2.60$ μm.

6.7 Evolution of rotating colloidal matter with increasing laser power

The collective motion of the PS ACs in the LG_0^3 optical field can be further modulated by increasing the incident laser power. For a single PS AC colloid, the angular velocity of the orbital motion increases with increasing laser power, having a linear trend as shown in fig. 6.8 (a). While undergoing orbital motion, the average radius of orbiting trajectory decreases with increasing laser power, as shown in fig. 6.8 (b). This is because of asymmetrical heating of the colloid due to its orbital motion as well as thermal fluctuations (see section 5.4.2 of chapter 5). Therefore, while changing the power from ~ 2 mW to ~ 7 mW, the estimated maximum surface temperature change $\Delta T \approx 12$ K (see Fig. 6.6 (d)) can lead to temperature dependant viscosity change as well as thermal diffusion properties of the colloid, leading to self-thermophoretic motion (see section 5.4.2 of chapter 5). The self-thermophoretic motion towards the inner side of the vortex beam is because of the fact that the beam intensity falls off faster on the inner side. The effect is similar to that of polarization dependence of the self-thermophoretic motion as discussed in section 5.4.3 chapter 5. However, we envisage that considering the small increase of temperature change and corresponding change in viscosity
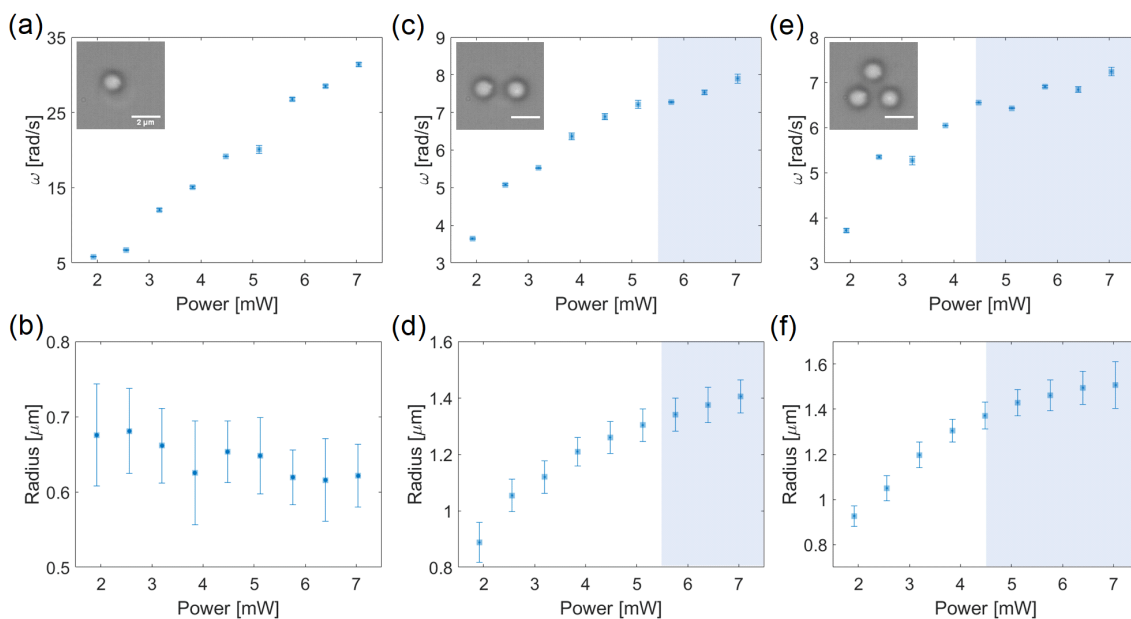
FIGURE 6.8: Evolution of the assembly and rotational dynamics with laser power. (a) The angular velocity of orbital motion of a single PS AC increases linearly with laser power. (b) Its radius of rotation decreases in the process due to self-thermophoretic behaviour. (c) The angular velocity and (d) the radius of rotation for a colloidal matter consisting 2 PS ACs increases with power at lower values, but undergoes saturating behaviour at higer powers (≥ 5.5 mW). (e) The angular velocity and (f) the radius of rotation for a colloidal matter consisting 3 PS ACs increases with power at lower values and undergoes saturating behaviour at powers ≥ 4.5 mW.

of water, it does not play the major in changing the angular velocity of the colloid.

In contrast to a single PS AC, the angular velocity of collective motion of two PS ACs shows increasing trend at lower laser power values as shown in fig. 6.8 (c), whereas at higher values (≥ 5.5 mW) indicated by the shaded region, the angular velocities undergo saturating behavior. Similarly, the radius of their collective motion of two PS ACs increases non-linearly with laser power, as shown in 6.8 (d). Such non-linearity can be attributed to their mutual thermal repulsion along with outwards self-thermophoretic motion at higher powers (≥ 5.5 mW), indicated by the shaded region. In case of the collective motion of a system of three colloids, the angular velocities of orbital motion increases at lower laser powers but at higher values (≥ 4.5 mW) undergo saturating behavior, depicted by the shaded region in fig. 6.8 (e). Similarly, its radius also increases non-linearly and undergoes saturation behavior at power ≥ 4.5 mW shown by the shaded region in fig. 6.8 (f) due to their mutual thermal repulsion as well as self-thermophoresis. The saturating behavior of angular velocity with increasing laser power for two and three PS ACs can be attributed to their increase of thermal repulsion with increasing laser power as well as, the colloids move outward from the LG_0^3 beam intensity part. In addition, the saturation occurs at lower power for three PS AC systems than the two PS AC system due to their higher system temperature than two PS AC systems at any given laser power.

6.8   Conclusion

To summarize, we have investigated self-organization and collective motion of polystyrene thermally active colloids driven by orbital energy flow of Laguerre-Gaussian beams. A single colloid undergoes optical trapping as well as optothermal heating due to incident optical field. In addition, the temperature distribution set up due to the trapped colloid acts as an environmental cue and leads to thermophoretic motion of the colloids in the vicinity. Multiple colloids form a colloidal matter in the optical field owing to their mutual thermal repulsion, and therefore leading to collective motion as a whole due to orbital energy flow facilitated azimuthal scattering force. The organization as well as the collective rotational motion of the colloidal matter self-evolves as a new colloid joins the assembly. The angular velocity of the collective motion decreases as the number of colloids increases in the assembly, due to their mutual thermal repulsion. In contrast, the angular velocity of an assembly of passive polystyrene colloids increases with their number of, owing to their hydrodynamic interaction. To further underline the effect of thermal repulsion in the collective motion, we have studied the collective motion of binary mixture of thermally active and passive polystyrene colloids. In addition, we have investigated the dynamics of the active colloidal matter with increasing laser power. For a single active colloid, the angular velocity of orbital motion

increases linearly with increasing laser power. Conversely, we show that for assembly of two and three colloids its radius of motion as well as angular velocity increases non-linearly with respect to increasing laser power, and exhibits saturating behaviour at higher power owing to thermal repulsion as well as self-thermophoretic motion.

Self-organization and collective motion of artificial colloids holds great ramification not only for non-equilibrium physics but also for various bio physical phenomena. It has been envisaged for microscopic engines as well as applications such as targeted task of drug delivery [139, 165]. To this end, the thermophoretic response of artificial active colloids have been harnesses in various configuration such as defocused beam in binary mixture [132] as well as laser steering with feedback [133]. However, the optical scattering forces have yet to be utilized in such systems. While for traditional Gaussian optical fields, the optical scattering force is dominant along the light propagation direction, the transverse optical scattering force of vortex beams presents itself as a useful tool for providing the driving forces for the colloids. The heating due to optical field and the driving due to angular momentum present in these beams allows investigation of dynamics self-evolving assembly as well as collective motion of the active colloids. The study can serve as a model system to study questions related to driven active matters as well as can be harnessed as a re-configurable colloidal micro-engine.

Chapter 7

Conclusions and future directions

In conclusion, the work presented in this thesis discusses some recent efforts in investigation of light-matter interactions with nanoscopic as well as microscopic objects. The discussions presented in the chapters investigated implications in light-matter interactions due to intensity, polarization as well as phase of the incident optical fields. In doing so, we have covered a diverse range of phenomena covering from spin-orbit interactions of angular momentum carrying beams with a mono-crystalline silver nanowire to optothermal interactions with iron oxide infused polystyrene thermally active colloids. The optical setup employed for the studies involved operation and modification of a home-built two-channel optical microscope, integrated with Fourier plane imaging capability for momentum space imaging as well as a fast camera for observation of millisecond colloidal dynamics. The experimental results as well as the supporting numerical calculations ineluctably establishes the importance of considering the vectorial nature of optical fields at the focal plane of a high numerical aperture objective lens. In addition, we have discussed the role of geometrical arrangements and symmetries in the presented light-matter interaction phenomena.

In the following paragraphs we summarize the different experimental results presented in the chapters of this thesis, broadly divided into two parts: investigation of spin-orbit interactions and investigation of optothermal interactions of active colloids. Importantly, we will also present some outlines to extrapolate the results for future studies. We envisage, the presented results in this document will lead to better understanding of light-matter interaction related to sub-wavelength spin-orbit interactions as well as optothermal interactions with active as well as passive colloids in fluidic environments.

The first problem we discussed in chapter 3, involves investigation of spin-orbit interaction of circularly polarized Laguerre-Gaussian beams with a mono-crystalline silver nanowire (AgNW), which acts as a sub-wavelength strip scatterer. Herein, we addressed the problem of simultaneous and unambiguous detection of spin and orbital angular momentum components of an incident optical field. The transverse component of the Poynting vector also known as the transverse energy flow due to spin as well as orbital angular momentum beams represents a momentum direction and sense. Such momentum can be transferred

onto a probe particle to facilitate its rotational motion. On the other hand, it can also lead to preferential scattering upon scattering, the directionality of which is dependent on the magnitude and sign of the angular momentum value. In addition, the orthogonality of the angular momentum states represent mutually orthogonal states which can be harnessed for optical communication. Therefore, to simultaneously distinguish the constituent components of the total angular momentum we employ Fourier plane microscopy, which enables precise measurement and quantification of preferential scattering due to the transverse energy flow components. The analysis of scattering pattern of incident circularly polarized LG beams from an AgNW in the sub and super-critical region of in the Fourier plane leads to the conclusion that - preference of scattering in the sub-critical region changes when the spin is inverted, whereas the super-critical region intensity distribution preference depends predominantly on the orbital energy flow of the incident beam. The detection mechanism relies on the polarization dependent scattering behavior of the nanowire. The effective directionality trends have been further investigated through calculation of focal optical field and corresponding transverse energy flow constituent due to spin and orbital angular momentum of the light beam. The presented work exhibits a single element based angular momentum detection mechanism and bypasses the requirement of complex nanofabrication based on-chip photonic structures.

Subsequently, in chapter 4, we go one step further and investigate the spin density of the optical fields. Specifically, we investigate the longitudinal spin density due to focusing of incident linearly polarized Gaussian and Hermite Gaussian beams and the consequent spin-Hall effect by analysing the scattered signal from a single AgNW. We show that, contrary to the paraxial to linearly polarized optical field possessing zero spin angular momentum, the strong focusing and consequent generation of vectorial optical field can possess partial spin angular momentum in the form of spin densities. The longitudinal spin density component can be detected by analyzing the circular polarization component of the scattered light, which leads to a spin-dependent anti-symmetric intensity distribution in the Fourier plane, therefore exhibiting angular spin-Hall effect. The corresponding longitudinal spin density was found to be enhanced by a factor 1.31 for HG beam with respect to that of Gaussian beam. By studying the numerically calculated focal optical fields as well as the scattered light with finite element method numerical calculations, we attribute the observed effect to the generation of longitudinally spinning optical fields due to focusing, hinting at the geometrical origin of the effect. Our experiments reveal the very intricate nature of the SOI between a focused optical beam and a nanoscopic object.

In the following part we outline possible future implications of the experimental results presented here.

Future directions:

Both these chapters (chapter 3 and 4) aim at investigation of incident focal focal optical fields and understanding the resultant spin-orbit interactions. In doing so, we try to read out the polarization as well as angular momentum state of the incident optical field, as well as its modification due to strong focusing. Therefore, in the following we lay out possibilities for harnessing the detection mechanism as well as the scattered light from the nanowire for future studies.

- One of the possible extrapolations to the presented results can be to use them as a polarization sensor, allowing us to detect any elliptical polarization of the incident light beam. The directionality of the scattered light from an AgNW in the sub- and super-critical region of the Fourier plane as well as intensity in the super-critical region depends on the polarization state of the incident light beam. Hence polarization dependent study of the parameters can lead to determination of specific polarization state of the incident beam. Similar polarization dependent directionality has been investigated from other structures as well [15, 166]. To this end, a similar approach has been presented in Fig. 3.10 of chapter 3, where we have examined the polarization dependence of the parameters - directionality in the sub- (D_{sub}) and super-critical region (D_{super}), as well as intensity in the super-critical region (I_{super}) of the Fourier plane. In doing so, we establish protocols for detection of specific polarization states, namely, left-circularly polarized and right-circularly polarized states. In addition,we have pointed out the difficulties of measuring generalized elliptical polarization states. However, with more involved study and investigation of additional parameters, any generalized polarization can be determined.

- Strong focusing of beam possessing orbital angular momentum such as Laguerre Gaussian beams can also lead to orbital to spin angular momentum conversion and consequent generation of spin densities, much more enhanced with respect to the linearly polarized Gaussian/Hermite Gaussian beams cases. Similar effect of generation and conversion of angular momentum of light has been theoretically investigated as well as experimentally probed through transmission of vectorial beams through a stratified medium [22] and by focusing effects [167]. In specific cases, the scattering induced angular momentum interconversion has been studied through interaction with chiral scatterers [110, 168]. In similar lines, the scattering from a single AgNW can also be harnessed to potential read out of the spin densities due to focussing of LG beams. The consequent orbital to spin angular momentum conversion can be detected by polarization analysis of the scattered signal as well as investigation of the phase distribution of the scattered light through interferometric methods.

• In addition to the extraction of information of the focal optical fields, the scattered light allows us to modify the focal optical field intensity, as well as its energy flow direction. A specific example has been presented in Fig. 3.3 (e) by comparing the transverse energy flow due to interaction with the nanowire for x and y polarized incident LG_0^1 beam. Such modification of energy flow can be detected by examining the dynamics of a probe particle in the vicinity of the nanowire surface. Scattering induced interaction can also lead to a very rich signature of the optical force landscape, which can potentially be harnessed for optical trapping and manipulation.

In the following parts of the thesis, in chapter 5 we have investigated the optothermal interactions due to optical heating of metallic nanoparticles embedded in the volume of polystyrene active colloids dispersed in deionized water. In keeping with the theme of the thesis, we investigate the effect of focused and defocused optical field intensity distribution and polarization on the optical trapping and dynamic assembly of these self-heating colloids. Specifically, we harness the self-heating as well as thermophoretic behavior of iron-oxide infused polystyrene colloids to investigate the optothermal interactions. The resulting attractive and repulsive forces lead to reconfigurable assembly of the colloids in a defocused optical field, which further undergoes self-evolution as a new colloid joins the assembly. Additionally, the experimental results indicate that the polarization of the incident optical field and the consequent vectorial nature of the optical field intensity distribution at the focal plane can be employed to control the direction of self-thermophoretic motion of the colloids as well as the structural orientation of the assembly.

In the following chapter,in chapter 6, we discussed self-organization and collective motion of the iron oxide infused polystyrene thermally active colloids driven by the energy flow of Laguerre-Gaussian beams. Similar to the study of the previous chapter, the self-heating nature of the polystyrene active colloids were harnessed to generate an environmental perturbation in which the surrounding colloids undergo thermophoretic motion. In addition, the short-range thermal repulsion of two equally heated colloids lead to self-evolution of the assembly as well as collective motion under the influence of the scattering force due to the orbital energy flow. The radial optical force as well as the azimuthal driving scattering force have been extracted by analyzing the trajectories of the colloids as well as by means of numerical simulations. Finally, we have also investigated the self-evolution of the structures with respect to increment of incident laser power as well in binary mixture of colloids.

In what follows, we discuss how the results can be extrapolated for future studies.

Future directions:

The two chapters investigate the optothermal interaction of active colloids as well as the formation and collective dynamics of reconfigurable active colloidal matter in different incident optical field configurations. In doing so, we have discussed various properties of the thermally active colloids such as their self-thermophoretic behavior, thermophoretic migration, as well as investigated inter-particle interactions. In addition, we have investigated how the interactions and dynamics get modulated by the various properties of the incident optical fields. Specifically the themophoretic as well as the self-thermophoretic nature of the colloids can be harnessed in various ways and we lay out a few possibilities in the following points.

- The volume distribution of the iron-oxide nanoparticulate inclusions within the colloid renders them roughly symmetric. Therefore, their activity stems from asymmetric illumination of focused light. An alternate method of forming an asymmetric arrangement will be by assembling a binary mixture of colloids - passive dielectric colloids and thermally active colloids. Such a system even in the case of symmetric illumination may exhibit active dynamics. Similar systems have been investigated in a critical mixture and their active dynamics have been studied [169]. The active-passive binary system and its dynamics can potentially be harnessed as a colloidal micro engine and non-equilibrium dynamics.

- The optothermal assembly of active colloids in the defocused optical assembly can also potentially be used for selective tasks such as reconfigurable colloidal engines, as well as the arrangement with specific photonic properties. In addition, it is possible to study dynamics of the colloids in binary systems, in crowded environments under various optical illumination and environmental conditions for investigation of collective motion such as swarming, vortex formation.

In summary, the work presented in this thesis discusses a diverse group of light-matter interaction phenomena whose characteristics are dictated by similar laser excitation arrangement, i.e., strongly focused optical fields. The results are corroborated with optical field calculations as well as accompanied with extensive analysis of the experimental data to point out the driving principle. We hope that the results will find interest in the community and can lead to more enriched knowledge of various light-matter interactions with focused optical fields.

Bibliography

[1] J. H. Poynting, "The wave motion of a revolving shaft, and a suggestion as to the angular momentum in a beam of circularly polarised light", Proceedings of the Royal Society of London. Series A, Containing Papers of a Mathematical and Physical Character **82**, 560–567 (1909).

[2] L. Allen, M. W. Beijersbergen, R. J. C. Spreeuw, and J. P. Woerdman, "Orbital angular momentum of light and the transformation of laguerre-gaussian laser modes", Phys. Rev. A **45**, 8185–8189 (1992).

[3] S. Franke-Arnold, L. Allen, and M. Padgett, "Advances in optical angular momentum", Laser & Photonics Reviews **2**, 299–313 (2008).

[4] L. Novotny and B. Hecht, *Principles of nano-optics*, 2nd ed. (Cambridge University Press, 2012).

[5] A. Ashkin, "Acceleration and trapping of particles by radiation pressure", Phys. Rev. Lett. **24**, 156–159 (1970).

[6] A. Ashkin, J. M. Dziedzic, J. E. Bjorkholm, and S. Chu, "Observation of a single-beam gradient force optical trap for dielectric particles", Opt. Lett. **11**, 288–290 (1986).

[7] A. Ashkin, "Optical trapping and manipulation of neutral particles using lasers", Proceedings of the National Academy of Sciences **94**, 4853–4860 (1997).

[8] K. Bliokh and Y. Bliokh, "Topological spin transport of photons: the optical Magnus effect and Berry phase", Physics Letters A **333**, 181–186 (2004).

[9] M. Onoda, S. Murakami, and N. Nagaosa, "Hall effect of light", Phys. Rev. Lett. **93**, 083901 (2004).

[10] K. Y. Bliokh and Y. P. Bliokh, "Conservation of angular momentum, transverse shift, and spin Hall effect in reflection and refraction of an electromagnetic wave packet", Phys. Rev. Lett. **96**, 073903 (2006).

[11] K. Y. Bliokh and A Aiello, "Goos–Hänchen and Imbert–Fedorov beam shifts: an overview", Journal of Optics **15**, 014001 (2013).

[12] D. K. Sharma, V. Kumar, A. B. Vasista, S. K. Chaubey, and G. V. P. Kumar, "Spin-Hall effect in the scattering of structured light from plasmonic nanowire", Opt. Lett. **43**, 2474–2477 (2018).

[13]D. Paul, D. K. Sharma, and G. V. P. Kumar, "Focused linearly-polarized-light scattering from a silver nanowire: experimental characterization of the optical spin-Hall effect", Phys. Rev. A **103**, 013520 (2021).

[14]K. Y. Bliokh, "Geometrical optics of beams with vortices: berry phase and orbital angular momentum Hall effect", Phys. Rev. Lett. **97**, 043901 (2006).

[15]J. Lin, J. P. B. Mueller, Q. Wang, G. Yuan, N. Antoniou, X.-C. Yuan, and F. Capasso, "Polarization-controlled tunable directional coupling of surface plasmon polaritons", Science **340**, 331–334 (2013).

[16]N. Shitrit, I. Yulevich, E. Maguid, D. Ozeri, D. Veksler, V. Kleiner, and E. Hasman, "Spin-optical metamaterial route to spin-controlled photonics", Science **340**, 724–726 (2013).

[17]D. O'Connor, P. Ginzburg, F. J. Rodríguez-Fortuño, G. A. Wurtz, and A. V. Zayats, "Spin–orbit coupling in surface plasmon scattering by nanostructures", Nature Communications **5**, 5327 (2014).

[18]D. K. Sharma, V. Kumar, A. B. Vasista, D. Paul, S. K. Chaubey, and G. V. P. Kumar, "Optical orbital angular momentum read-out using a self-assembled plasmonic nanowire", ACS Photonics **6**, 148–153 (2019).

[19]Y. Zhao, J. S. Edgar, G. D. M. Jeffries, D. McGloin, and D. T. Chiu, "Spin-to-orbital angular momentum conversion in a strongly focused optical beam", Phys. Rev. Lett. **99**, 073901 (2007).

[20]K. Y. Bliokh, E. A. Ostrovskaya, M. A. Alonso, O. G. Rodríguez-Herrera, D. Lara, and C. Dainty, "Spin-to-orbital angular momentum conversion in focusing, scattering, and imaging systems", Opt. Express **19**, 26132–26149 (2011).

[21]R. C. Devlin, A. Ambrosio, N. A. Rubin, J. P. B. Mueller, and F. Capasso, "Arbitrary spin-to-orbital angular momentum conversion of light", Science **358**, 896–901 (2017).

[22]S. Nechayev, J. S. Eismann, R. Alaee, E. Karimi, R. W. Boyd, and P. Banzer, "Kelvin's chirality of optical beams", Phys. Rev. A **103**, L031501 (2021).

[23]W. L. Barnes, A. Dereux, and T. W. Ebbesen, "Surface plasmon subwavelength optics", Nature **424**, 824–830 (2003).

[24]W. L. Barnes, "Surface plasmon–polariton length scales: a route to sub-wavelength optics", Journal of Optics A: Pure and Applied Optics **8**, S87–S93 (2006).

[25]M. Righini, A. S. Zelenina, C. Girard, and R. Quidant, "Parallel and selective trapping in a patterned plasmonic landscape", Nature Physics **3**, 477–480 (2007).

[26]L. R. E. C. and P. G. Etchegoin, *Principles of surface-enhanced Raman spectroscopy: and related plasmonic effects* (Elsevier, 2011).

[27] A. B. Vasista, H. Jog, T. Heilpern, M. E. Sykes, S. Tiwari, D. K. Sharma, S. K. Chaubey, G. P. Wiederrecht, S. K. Gray, and G. V. P. Kumar, "Differential wavevector distribution of surface-enhanced Raman scattering and fluorescence in a film-coupled plasmonic nanowire cavity", Nano Letters **18**, 650–655 (2018).

[28] T. Neumann, M.-L. Johansson, D. Kambhampati, and W. Knoll, "Surface-plasmon fluorescence spectroscopy", Advanced Functional Materials **12**, 575–586 (2002).

[29] G.-C. Li, Q. Zhang, S. A. Maier, and D. Lei, "Plasmonic particle-on-film nanocavities: a versatile platform for plasmon-enhanced spectroscopy and photochemistry", Nanophotonics **7**, 1865–1889 (2018).

[30] K. Kneipp, Y. Wang, H. Kneipp, L. T. Perelman, I. Itzkan, R. R. Dasari, and M. S. Feld, "Single molecule detection using surface-enhanced Raman scattering (sers)", Phys. Rev. Lett. **78**, 1667–1670 (1997).

[31] S. Nie and S. R. Emory, "Probing single molecules and single nanoparticles by surface-enhanced Raman scattering", Science **275**, 1102–1106 (1997).

[32] P. P. Patra, R. Chikkaraddy, R. P. N. Tripathi, A. Dasgupta, and G. V. P. Kumar, "Plasmofluidic single-molecule surface-enhanced Raman scattering from dynamic assembly of plasmonic nanoparticles", Nature Communications **5**, 4357 (2014).

[33] S. Tiwari, U. Khandelwal, V. Sharma, and G. P. Kumar, "Single molecule surface enhanced Raman scattering in a single gold nanoparticle-driven thermoplasmonic tweezer", The Journal of Physical Chemistry Letters **12**, 11910–11918 (2021).

[34] G. Baffou, *Thermoplasmonics: heating metal nanoparticles using light* (Cambridge University Press, 2017).

[35] G. Baffou, F. Cichos, and R. Quidant, "Applications and challenges of thermoplasmonics", Nature Materials **19**, 946–958 (2020).

[36] R Piazza and A Parola, "Thermophoresis in colloidal suspensions", Journal of Physics: Condensed Matter **20**, 153102 (2008).

[37] R. Piazza, "Thermophoresis: moving particles with thermal gradients", Soft Matter **4**, 1740–1744 (2008).

[38] M. Braun and F. Cichos, "Optically controlled thermophoretic trapping of single nano-objects", ACS Nano **7**, 11200–11208 (2013).

[39] F. M. Weinert and D. Braun, "Observation of slip flow in thermophoresis", Phys. Rev. Lett. **101**, 168301 (2008).

[40] A. P. Bregulla, A. Würger, K. Günther, M. Mertig, and F. Cichos, "Thermo-osmotic flow in thin films", Phys. Rev. Lett. **116**, 188303 (2016).

[41]H.-R. Jiang, H. Wada, N. Yoshinaga, and M. Sano, "Manipulation of colloids by a nonequilibrium depletion force in a temperature gradient", Phys. Rev. Lett. **102**, 208301 (2009).

[42]A. Würger, "Thermal non-equilibrium transport in colloids", Reports on Progress in Physics **73**, 126601 (2010).

[43]L. Lin, E. H. Hill, X. Peng, and Y. Zheng, "Optothermal manipulations of colloidal particles and living cells", Accounts of Chemical Research **51**, 1465–1474 (2018).

[44]V. Sharma, D. Paul, S. K. Chaubey, S. Tiwari, and G. V. P. Kumar, "Large-scale optothermal assembly of colloids mediated by a gold microplate", Journal of Physics: Condensed Matter **32**, 324002 (2020).

[45]M. Trivedi, D. Saxena, W. K. Ng, R. Sapienza, and G. Volpe, "Self-organized lasers from reconfigurable colloidal assemblies", Nature Physics, `10.1038/s41567-022-01656-2` (2022).

[46]A. M. Yao and M. J. Padgett, "Orbital angular momentum: origins, behavior and applications", Adv. Opt. Photon. **3**, 161–204 (2011).

[47]A. Bekshaev, K. Y. Bliokh, and M. Soskin, "Internal flows and energy circulation in light beams", Journal of Optics **13**, 053001 (2011).

[48]T. Setälä, A. Shevchenko, M. Kaivola, and A. T. Friberg, "Degree of polarization for optical near fields", Phys. Rev. E **66**, 016615 (2002).

[49]D. G. Grier, "A revolution in optical manipulation", Nature **424**, 810–816 (2003).

[50]V. Garcés-Chávez, D. McGloin, M. J. Padgett, W. Dultz, H. Schmitzer, and K. Dholakia, "Observation of the transfer of the local angular momentum density of a multiringed light beam to an optically trapped particle", Phys. Rev. Lett. **91**, 093602 (2003).

[51]Y. Zhao, D. Shapiro, D. Mcgloin, D. T. Chiu, and S. Marchesini, "Direct observation of the transfer of orbital angular momentum to metal particles from a focused circularly polarized gaussian beam", Opt. Express **17**, 23316–23322 (2009).

[52]P. H. Jones, O. M. Maragò, and G. Volpe, *Optical tweezers: principles and applications* (Cambridge University Press, 2015).

[53]C. J. Bustamante, Y. R. Chemla, S. Liu, and M. D. Wang, "Optical tweezers in single-molecule biophysics", Nature Reviews Methods Primers **1**, 25 (2021).

[54]A. L. Pyayt, B. Wiley, Y. Xia, A. Chen, and L. Dalton, "Integration of photonic and silver nanowire plasmonic waveguides", Nature Nanotechnology **3**, 660–665 (2008).

[55]M. Song, A. Bouhelier, P. Bramant, J. Sharma, E. Dujardin, D. Zhang, and G. Colas-des Francs, "Imaging symmetry-selected corner plasmon modes in penta-twinned crystalline ag nanowires", ACS Nano **5**, 5874–5880 (2011).

[56]H. Yang, M. Qiu, and Q. Li, "Identification and control of multiple leaky plasmon modes in silver nanowires", Laser & Photonics Reviews **10**, 278–286 (2016).

[57]V. Garcés-Chávez, R. Quidant, P. J. Reece, G. Badenes, L. Torner, and K. Dholakia, "Extended organization of colloidal microparticles by surface plasmon polariton excitation", Phys. Rev. B **73**, 085417 (2006).

[58]G. Baffou, R. Quidant, and F. J. García de Abajo, "Nanoscale control of optical heating in complex plasmonic systems", ACS Nano **4**, 709–716 (2010).

[59]V. S. Liberman and B. Y. Zel'dovich, "Spin-orbit interaction of a photon in an inhomogeneous medium", Phys. Rev. A **46**, 5199–5207 (1992).

[60]K. Y. Bliokh, F. J. Rodríguez-Fortuño, F. Nori, and A. V. Zayats, "Spin–orbit interactions of light", Nature Photonics **9**, 796–808 (2015).

[61]J. Wang, J.-Y. Yang, I. M. Fazal, N. Ahmed, Y. Yan, H. Huang, Y. Ren, Y. Yue, S. Dolinar, M. Tur, and A. E. Willner, "Terabit free-space data transmission employing orbital angular momentum multiplexing", Nature Photonics **6**, 488–496 (2012).

[62]A. Nicolas, L. Veissier, L. Giner, E. Giacobino, D. Maxein, and J. Laurat, "A quantum memory for orbital angular momentum photonic qubits", Nature Photonics **8**, 234–238 (2014).

[63]M. I. D'Yakonov and V. I. Perel', "Possibility of Orienting Electron Spins with Current", ZhETF Pisma Redaktsiiu **13**, 657 (1971).

[64]J. E. Hirsch, "Spin Hall effect", Phys. Rev. Lett. **83**, 1834–1837 (1999).

[65]D. G. Grier and Y. Roichman, "Holographic optical trapping", Appl. Opt. **45**, 880–887 (2006).

[66]E. R. Dufresne and D. G. Grier, "Optical tweezer arrays and optical substrates created with diffractive optics", Review of Scientific Instruments **69**, 1974–1977 (1998).

[67]E. R. Dufresne, G. C. Spalding, M. T. Dearing, S. A. Sheets, and D. G. Grier, "Computer-generated holographic optical tweezer arrays", Review of Scientific Instruments **72**, 1810–1816 (2001).

[68]N. R. Heckenberg, R. McDuff, C. P. Smith, and A. G. White, "Generation of optical phase singularities by computer-generated holograms", Opt. Lett. **17**, 221–223 (1992).

[69]M. Massari, G. Ruffato, M. Gintoli, F. Ricci, and F. Romanato, "Fabrication and characterization of high-quality spiral phase plates for optical applications", Appl. Opt. **54**, 4077–4083 (2015).

[70] D. Murugesapillai, M. J. McCauley, L. J. Maher, and M. C. Williams, "Single-molecule studies of high-mobility group b architectural dna bending proteins", Biophysical Reviews **9**, 17–40 (2017).

[71] R. Vaippully, V. Ramanujan, M. Gopalakrishnan, S. Bajpai, and B. Roy, "Detection of sub-degree angular fluctuations of the local cell membrane slope using optical tweezers", Soft Matter **16**, 7606–7612 (2020).

[72] I. A. Martínez, E. Roldán, L. Dinis, and R. A. Rica, "Colloidal heat engines: a review", Soft Matter **13**, 22–36 (2017).

[73] S. Paul, A. Jayaram, N Narinder, T. Speck, and C. Bechinger, "Force generation in confined active fluids: the role of microstructure", Phys. Rev. Lett. **129**, 058001 (2022).

[74] P. Schuck, "Use of surface plasmon resonance to probe the equilibrium and dynamic aspects of interactions between biological macromolecules", Annual Review of Biophysics and Biomolecular Structure **26**, 541–566 (1997).

[75] "Fourier optics", in *Fundamentals of photonics* (John Wiley & Sons, Ltd, 1991) Chap. 4, pp. 108–156.

[76] J. A. Kurvits, M. Jiang, and R. Zia, "Comparative analysis of imaging configurations and objectives for fourier microscopy", J. Opt. Soc. Am. A **32**, 2082–2092 (2015).

[77] A. B. Vasista, D. K. Sharma, and G. P. Kumar, "Fourier plane optical microscopy and spectroscopy", in *Digital encyclopedia of applied physics* (John Wiley & Sons, Ltd, 2019), pp. 1–14.

[78] E. Wolf and D. Gabor, "Electromagnetic diffraction in optical systems - i. an integral representation of the image field", Proceedings of the Royal Society of London. Series A. Mathematical and Physical Sciences **253**, 349–357 (1959).

[79] C. Tangi Le Guennic, *How is an OAM generated? what is the potential of oam generators on the market?*, (2020) `https://blog.cailabs.com/en/how-is-an-oam-generated`.

[80] I. C. Lenton, A. B. Stilgoe, T. A. Nieminen, and H. Rubinsztein-Dunlop, "OTSLM toolbox for structured light methods", Computer Physics Communications **253**, 107199 (2020).

[81] A. A. Pushkina, J. I. Costa-Filho, G Maltese, and A. I. Lvovsky, "Comprehensive model and performance optimization of phase-only spatial light modulators", Measurement Science and Technology **31**, 125202 (2020).

[82] M. A. Lieb, J. M. Zavislan, and L. Novotny, "Single-molecule orientations determined by direct emission pattern imaging", J. Opt. Soc. Am. B **21**, 1210–1215 (2004).

[83] B. Richards, E. Wolf, and D. Gabor, "Electromagnetic diffraction in optical systems, ii. structure of the image field in an aplanatic system", Proceedings of the Royal Society of London. Series A. Mathematical and Physical Sciences **253**, 358–379 (1959).

[84] J. Yang, J.-P. Hugonin, and P. Lalanne, "Near-to-far field transformations for radiative and guided waves", ACS Photonics **3**, 395–402 (2016).

[85] D. Paul, D. K. Sharma, and G. V. P. Kumar, "Simultaneous detection of spin and orbital angular momentum of light through scattering from a single silver nanowire", Laser & Photonics Reviews **16**, 2200049 (2022).

[86] M. Padgett, J. Arlt, N. Simpson, and L. Allen, "An experiment to observe the intensity and phase structure of laguerreâĂŞgaussian laser modes", American Journal of Physics **64**, 77–82 (1996).

[87] J. Leach, M. J. Padgett, S. M. Barnett, S. Franke-Arnold, and J. Courtial, "Measuring the orbital angular momentum of a single photon", Phys. Rev. Lett. **88**, 257901 (2002).

[88] J. Leach, J. Courtial, K. Skeldon, S. M. Barnett, S. Franke-Arnold, and M. J. Padgett, "Interferometric methods to measure orbital and spin, or the total angular momentum of a single photon", Phys. Rev. Lett. **92**, 013601 (2004).

[89] C. V. Felde, "Diffraction diagnostics of phase singularities at optical beams", in Sixth international conference on correlation optics, Vol. 5477, edited by O. V. Angelsky (International Society for Optics and Photonics, 2004), pp. 67 –76.

[90] B Jack, M. J. Padgett, and S Franke-Arnold, "Angular diffraction", New Journal of Physics **10**, 103013 (2008).

[91] L. E. E. de Araujo and M. E. Anderson, "Measuring vortex charge with a triangular aperture", Opt. Lett. **36**, 787–789 (2011).

[92] A. Bekshaev, L. Mikhaylovskaya, S. Patil, V. Kumar, and R. P. Singh, "Optical-vortex diagnostics via fraunhofer slit diffraction with controllable wavefront curvature", J. Opt. Soc. Am. A **37**, 780–786 (2020).

[93] A. Mair, A. Vaziri, G. Weihs, and A. Zeilinger, "Entanglement of the orbital angular momentum states of photons", Nature **412**, 313–316 (2001).

[94] M. Pu, X. Li, X. Ma, Y. Wang, Z. Zhao, C. Wang, C. Hu, P. Gao, C. Huang, H. Ren, X. Li, F. Qin, J. Yang, M. Gu, M. Hong, and X. Luo, "Catenary optics for achromatic generation of perfect optical angular momentum", Science Advances **1**, e1500396 (2015).

[95] Y. Guo, M. Pu, Z. Zhao, Y. Wang, J. Jin, P. Gao, X. Li, X. Ma, and X. Luo, "Merging geometric phase and plasmon retardation phase in continuously shaped metasurfaces for arbitrary orbital angular momentum generation", ACS Photonics **3**, 2022–2029 (2016).

[96] P. Genevet, J. Lin, M. A. Kats, and F. Capasso, "Holographic detection of the orbital angular momentum of light with plasmonic photodiodes", Nature Communications **3**, 1278 (2012).

[97] J. Chen, X. Chen, T. Li, and S. Zhu, "On-chip detection of orbital angular momentum beam by plasmonic nanogratings", Laser & Photonics Reviews **12**, 1700331 (2018).

[98] S. Zhang, P. Huo, W. Zhu, C. Zhang, P. Chen, M. Liu, L. Chen, H. J. Lezec, A. Agrawal, Y. Lu, and T. Xu, "Broadband detection of multiple spin and orbital angular momenta via dielectric metasurface", Laser & Photonics Reviews **14**, 2000062 (2020).

[99] Y. Sun, Y. Yin, B. T. Mayers, T. Herricks, and Y. Xia, "Uniform silver nanowires synthesis by reducing agno3 with ethylene glycol in the presence of seeds and poly(vinyl pyrrolidone)", Chemistry of Materials **14**, 4736–4745 (2002).

[100] N. Visaveliya and J. M. Kãűhler, "A self-seeding synthesis of ag microrods of tuned aspect ratio: ascorbic acid plays a key role", Nanotechnology **24**, 345604 (2013).

[101] C. Taneja, D. Paul, and G. V. Pavan Kumar, "Experimental observation of transverse spin of plasmon polaritons in a single crystalline silver nanowire", Applied Physics Letters **119**, 161108 (2021).

[102] S. Tiwari, C. Taneja, V. Sharma, A. B. Vasista, D. Paul, and G. V. Pavan Kumar, "Dielectric microsphere coupled to a plasmonic nanowire: a self-assembled hybrid optical antenna", Advanced Optical Materials **8**, 1901672 (2020).

[103] H. Wei, Z. Wang, X. Tian, M. Käll, and H. Xu, "Cascaded logic gates in nanophotonic plasmon networks", Nature Communications **2**, 387 (2011).

[104] D. Haefner, S. Sukhov, and A. Dogariu, "Spin Hall effect of light in spherical geometry", Phys. Rev. Lett. **102**, 123903 (2009).

[105] K. Y. Bliokh, M. A. Alonso, E. A. Ostrovskaya, and A. Aiello, "Angular momenta and spin-orbit interaction of nonparaxial light in free space", Phys. Rev. A **82**, 063825 (2010).

[106] T. A. Nieminen, A. B. Stilgoe, N. R. Heckenberg, and H. Rubinsztein-Dunlop, "Angular momentum of a strongly focused gaussian beam", Journal of Optics A: Pure and Applied Optics **10**, 115005 (2008).

[107] Z. Bomzon, M. Gu, and J. Shamir, "Angular momentum and geometrical phases in tight-focused circularly polarized plane waves", Applied Physics Letters **89**, 241104 (2006).

[108] O. G. Rodríguez-Herrera, D. Lara, K. Y. Bliokh, E. A. Ostrovskaya, and C. Dainty, "Optical nanoprobing via spin-orbit interaction of light", Phys. Rev. Lett. **104**, 253601 (2010).

[109] M. Neugebauer, S. Nechayev, M. Vorndran, G. Leuchs, and P. Banzer, "Weak measurement enhanced spin Hall effect of light for particle displacement sensing", Nano Letters **19**, 422–425 (2019).

[110] S. Nechayev, J. S. Eismann, G. Leuchs, and P. Banzer, "Orbital-to-spin angular momentum conversion employing local helicity", Phys. Rev. B **99**, 075155 (2019).

[111] F. Cardano and L. Marrucci, "Spin–orbit photonics", Nature Photonics **9**, 776–778 (2015).

[112] K. Y. Bliokh and F. Nori, "Transverse and longitudinal angular momenta of light", Physics Reports **592**, 1 –38 (2015).

[113] A. Aiello and P. Banzer, "The ubiquitous photonic wheel", Journal of Optics **18**, 085605 (2016).

[114] A. Y. Bekshaev, "Spin–orbit interaction of light and diffraction of polarized beams", Journal of Optics **19**, 085602 (2017).

[115] M. Born, E. Wolf, A. B. Bhatia, P. C. Clemmow, D. Gabor, A. R. Stokes, A. M. Taylor, P. A. Wayman, and W. L. Wilcock, *Principles of optics: electromagnetic theory of propagation, interference and diffraction of light*, 7th ed. (Cambridge University Press, 1999).

[116] M. Neugebauer, P. Banzer, and S. Nechayev, "Emission of circularly polarized light by a linear dipole", Science Advances **5**, `10.1126/sciadv.aav7588` (2019).

[117] L.-k. Shi and J. C. W. Song, "Shift vector as the geometric origin of beam shifts", Phys. Rev. B **100**, 201405 (2019).

[118] Y. Liu, Z.-M. Yu, C. Xiao, and S. A. Yang, "Quantized circulation of anomalous shift in interface reflection", Phys. Rev. Lett. **125**, 076801 (2020).

[119] M. Neugebauer, T. Bauer, A. Aiello, and P. Banzer, "Measuring the transverse spin density of light", Phys. Rev. Lett. **114**, 063901 (2015).

[120] J. S. Eismann, L. H. Nicholls, D. J. Roth, M. A. Alonso, P. Banzer, F. J. Rodríguez-Fortuño, A. V. Zayats, F. Nori, and K. Y. Bliokh, "Transverse spinning of unpolarized light", Nature Photonics **15**, 156–161 (2021).

[121] D. Paul, R. Chand, and G. V. P. Kumar, "Optothermal evolution of active colloidal matter in a defocused laser trap", ACS Photonics **9**, 3440–3449, (2022) (arXiv:2203.08904).

[122] G. Volpe, R. Quidant, G. Badenes, and D. Petrov, "Surface plasmon radiation forces", Phys. Rev. Lett. **96**, 238101 (2006).

[123] G. Volpe and D. Petrov, "Torque detection using brownian fluctuations", Phys. Rev. Lett. **97**, 210603 (2006).

[124] L. Tong, V. D. Miljković, and M. Käll, "Alignment, rotation, and spinning of single plasmonic nanoparticles and nanowires using polarization dependent optical forces", Nano Letters **10**, 268–273 (2010).

[125] S. Duhr and D. Braun, "Optothermal molecule trapping by opposing fluid flow with thermophoretic drift", Phys. Rev. Lett. **97**, 038103 (2006).

[126] T. Bickel, A. Majee, and A. Würger, "Flow pattern in the vicinity of self-propelling hot janus particles", Phys. Rev. E **88**, 012301 (2013).

[127] M. Fränzl and F. Cichos, "Hydrodynamic manipulation of nano-objects by optically induced thermo-osmotic flows", Nature Communications **13**, 656 (2022).

[128] S. Ramaswamy, "The mechanics and statistics of active matter", Annual Review of Condensed Matter Physics **1**, 323–345 (2010).

[129] H.-R. Jiang, N. Yoshinaga, and M. Sano, "Active motion of a janus particle by self-thermophoresis in a defocused laser beam", Phys. Rev. Lett. **105**, 268302 (2010).

[130] M. C. Marchetti, J. F. Joanny, S. Ramaswamy, T. B. Liverpool, J. Prost, M. Rao, and R. A. Simha, "Hydrodynamics of soft active matter", Rev. Mod. Phys. **85**, 1143–1189 (2013).

[131] U. Khadka, V. Holubec, H. Yang, and F. Cichos, "Active particles bound by information flows", Nature Communications **9**, 3864 (2018).

[132] T. Bäuerle, R. C. Löffler, and C. Bechinger, "Formation of stable and responsive collective states in suspensions of active colloids", Nature Communications **11**, 2547 (2020).

[133] M. Fränzl, S. Muiños Landin, V. Holubec, and F. Cichos, "Fully steerable symmetric thermoplasmonic microswimmers", ACS Nano **15**, 3434–3440 (2021).

[134] F. Schmidt, H. Šípová-Jungová, M. Käll, A. Würger, and G. Volpe, "Non-equilibrium properties of an active nanoparticle in a harmonic potential", Nature Communications **12**, 1902 (2021).

[135] H. P. Zhang, A. Be'er, E.-L. Florin, and H. L. Swinney, "Collective motion and density fluctuations in bacterial colonies", Proceedings of the National Academy of Sciences **107**, 13626–13630 (2010).

[136] M. E. Cates, "Diffusive transport without detailed balance in motile bacteria: does microbiology need statistical physics?", Reports on Progress in Physics **75**, 042601 (2012).

[137] M. Ballerini, N. Cabibbo, R. Candelier, A. Cavagna, E. Cisbani, I. Giardina, V. Lecomte, A. Orlandi, G. Parisi, A. Procaccini, M. Viale, and V. Zdravkovic, "Interaction ruling animal collective behavior depends on topological rather than metric distance: evidence from a field study", Proceedings of the National Academy of Sciences **105**, 1232–1237 (2008).

[138]T. Vicsek and A. Zafeiris, "Collective motion", Physics Reports **517**, Collective motion, 71–140 (2012).

[139]F. Schmidt, A. Magazzù, A. Callegari, L. Biancofiore, F. Cichos, and G. Volpe, "Microscopic engine powered by critical demixing", Phys. Rev. Lett. **120**, 068004 (2018).

[140]C. Bechinger, R. Di Leonardo, H. Löwen, C. Reichhardt, G. Volpe, and G. Volpe, "Active particles in complex and crowded environments", Rev. Mod. Phys. **88**, 045006 (2016).

[141]M. Mijalkov, A. McDaniel, J. Wehr, and G. Volpe, "Engineering sensorial delay to control phototaxis and emergent collective behaviors", Phys. Rev. X **6**, 011008 (2016).

[142]L. Damet, G. M. Cicuta, J. Kotar, M. C. Lagomarsino, and P. Cicuta, "Hydrodynamically synchronized states in active colloidal arrays", Soft Matter **8**, 8672–8678 (2012).

[143]D. Paul, R. Chand, and G. V. P. Kumar, *SI movies - Optothermal evolution of active colloidal matter in defocused laser trap*, (2022) `https://youtube.com/playlist?list=PLVIRTkGrtbruGG2_wWC5CeA-4t_POOC_-` (visited on 2022).

[144]J.-Y. Tinevez, N. Perry, J. Schindelin, G. M. Hoopes, G. D. Reynolds, E. Laplantine, S. Y. Bednarek, S. L. Shorte, and K. W. Eliceiri, "Trackmate: an open and extensible platform for single-particle tracking", Methods **115**, 80–90 (2017).

[145]V. A. Markel, "Introduction to the Maxwell Garnett approximation: tutorial", JOSA A **33**, 1244–1256 (2016).

[146]K. Pietrak and T. S. Wiśniewski, "A review of models for effective thermal conductivity of composite materials.", Journal of Power Technologies **95** (2015).

[147]H. Brenner, "The slow motion of a sphere through a viscous fluid towards a plane surface", Chemical engineering science **16**, 242–251 (1961).

[148]R. G. Horn, "Refractive indices and order parameters of two liquid crystals", Journal de physique **39**, 105–109 (1978).

[149]S. Iacopini, R. Rusconi, and R. Piazza, "The "macromolecular tourist": universal temperature dependenceof thermal diffusion in aqueous colloidal suspensions", The European Physical Journal E **19**, 59–67 (2006).

[150]L. Helden, R. Eichhorn, and C. Bechinger, "Direct measurement of thermophoretic forces", Soft matter **11**, 2379–2386 (2015).

[151]M. Braibanti, D. Vigolo, and R. Piazza, "Does thermophoretic mobility depend on particle size?", Phys. Rev. Lett. **100**, 108303 (2008).

[152]F. Caprile, L. A. Masullo, and F. D. Stefani, "Pyfocus–a python package for vectorial calculations of focused optical fields under realistic conditions. application to toroidal foci", Computer Physics Communications, 108315 (2022).

[153] K. Dholakia and P. Zemánek, "Colloquium: Gripped by light: Optical binding", Rev. Mod. Phys. **82**, 1767–1791 (2010).

[154] K. Tunstrøm, Y. Katz, C. C. Ioannou, C. Huepe, M. J. Lutz, and I. D. Couzin, "Collective states, multistability and transitional behavior in schooling fish", PLOS Computational Biology **9**, 1–11 (2013).

[155] I. D. Couzin and J. Krause, "Self-organization and collective behavior in vertebrates", in , Vol. 32, Advances in the Study of Behavior (Academic Press, 2003), pp. 1–75.

[156] S. Camazine, *Self-organization in biological systems* (Princeton University Press, 2003).

[157] X. Wang, P.-C. Chen, K. Kroy, V. Holubec, and F. Cichos, *Spontaneous vortex formation by microswimmers with retarded attractions*, 2022.

[158] S. Muiños-Landin, A. Fischer, V. Holubec, and F. Cichos, "Reinforcement learning with artificial microswimmers", Science Robotics **6**, eabd9285 (2021).

[159] M. Fränzl and F. Cichos, "Active particle feedback control with a single-shot detection convolutional neural network", Scientific Reports **10**, 12571 (2020).

[160] G. Volpe and D. Petrov, "Torque detection using brownian fluctuations", Phys. Rev. Lett. **97**, 210603 (2006).

[161] Y. Roichman, B. Sun, Y. Roichman, J. Amato-Grill, and D. G. Grier, "Optical forces arising from phase gradients", Phys. Rev. Lett. **100**, 013602 (2008).

[162] Y. Sokolov, D. Frydel, D. G. Grier, H. Diamant, and Y. Roichman, "Hydrodynamic pair attractions between driven colloidal particles", Phys. Rev. Lett. **107**, 158302 (2011).

[163] V. Svak, O. Brzobohatý, M. Šiler, P. Jákl, J. Kaňka, P. Zemánek, and S. H. Simpson, "Transverse spin forces and non-equilibrium particle dynamics in a circularly polarized vacuum optical trap", Nature Communications **9**, 5453 (2018).

[164] T. Tsuji, R. Nakatsuka, K. Nakajima, K. Doi, and S. Kawano, "Effect of hydrodynamic inter-particle interaction on the orbital motion of dielectric nanoparticles driven by an optical vortex", Nanoscale **12**, 6673–6690 (2020).

[165] S. Goswami, A. Ghosh, and D. Dasgupta, "A minimalistic magnetic manipulation system for manouvering nanorobots", Preprint (**Version 1**), `10.21203/rs.3.rs-2431365/v1` (2023).

[166] M. Neugebauer, P. Woźniak, A. Bag, G. Leuchs, and P. Banzer, "Polarization-controlled directional scattering for nanoscopic position sensing", Nature Communications **7**, 11286 (2016).

[167]V. V. Kotlyar, A. G. Nalimov, A. A. Kovalev, A. P. Porfirev, and S. S. Stafeev, "Spin-orbit and orbit-spin conversion in the sharp focus of laser light: theory and experiment", Phys. Rev. A **102**, 033502 (2020).

[168]P. Woźniak, I. D. Leon, K. Höflich, G. Leuchs, and P. Banzer, "Interaction of light carrying orbital angular momentum with a chiral dipolar scatterer", Optica **6**, 961–965 (2019).

[169]J. Grauer, F. Schmidt, J. Pineda, B. Midtvedt, H. Löwen, G. Volpe, and B. Liebchen, "Active droploids", Nature Communications **12**, 6005 (2021).